


2019

Design and Implementation of Silicon-Based MEMS Resonators for Application in Ultra Stable High Frequency Oscillators

Sarah Shahraini
University of Central Florida

 Part of the [Electrical and Computer Engineering Commons](#)
Find similar works at: <https://stars.library.ucf.edu/etd>
University of Central Florida Libraries <http://library.ucf.edu>

This Doctoral Dissertation (Open Access) is brought to you for free and open access by STARS. It has been accepted for inclusion in Electronic Theses and Dissertations by an authorized administrator of STARS. For more information, please contact STARS@ucf.edu.

STARS Citation

Shahraini, Sarah, "Design and Implementation of Silicon-Based MEMS Resonators for Application in Ultra Stable High Frequency Oscillators" (2019). *Electronic Theses and Dissertations*. 6731.
<https://stars.library.ucf.edu/etd/6731>

**DESIGN AND IMPLEMENTATION OF SILICON-BASED MEMS RESONATORS FOR
APPLICATION IN ULTRA STABLE HIGH-FREQUENCY OSCILLATORS**

by

SARAH SHAHRAINI

B.S. Khaje Nasir University of Technology, 2010

M.S. Khaje Nasir University of Technology, 2012

A dissertation submitted in partial fulfillment of the requirements
for the degree of Doctor of Philosophy
in the Department of Electrical and Computer Engineering
in the College of Engineering and Computer Science
at the University of Central Florida
Orlando, Florida

Fall Term

2019

Major Professor: Reza Abdolvand

© 2019 Sarah Shahraini

ABSTRACT

The focus of this work is to design and implement resonators for ultra-stable high-frequency ($>100\text{MHz}$) silicon-based MEMS oscillators. Specifically, two novel types of resonators are introduced that push the performance of silicon-based MEMS resonators to new limits. Thin film Piezoelectric-on-Silicon (TPoS) resonators have been shown to be suitable for oscillator applications due to their combined high quality factor, coupling efficiency, power handling and doping-dependent temperature-frequency behavior. This thesis is an attempt to utilize the TPoS platform and optimize it for extremely stable high-frequency oscillator applications.

To achieve the said objective, two main research venues are explored. Firstly, quality factor is systematically studied and anisotropy of single crystalline silicon (SCS) is exploited to enable high-quality factor side-supported radial-mode (aka breathing mode) TPoS disc resonators through minimization of anchor-loss. It is then experimentally demonstrated that in TPoS disc resonators with tethers aligned to $[100]$, unloaded quality factor improves from ~ 450 for the second harmonic mode at 43 MHz to $\sim 11,500$ for the eighth harmonic mode at 196 MHz .

Secondly, thickness quasi-Lamé modes are studied and demonstrated in TPoS resonators for the first time. It is shown that thickness quasi-Lamé modes (TQLM) could be efficiently excited in silicon with very high quality factor (Q). A quality factor of 23.2 k is measured in vacuum at 185 MHz for a fundamental TQLM-TPoS resonators designed within a circular acoustic isolation frame. Quality factor of 12.6 k and 6 k are also

measured for the second- and third- harmonic TQLM TPoS resonators at 366 MHz and 555 MHz respectively. Turn-over temperatures between 40 °C to 125 °C are also designed and measured for TQLM TPoS resonators fabricated on degenerately N-doped silicon substrates. The reported extremely high quality factor, very low motional resistance, and tunable turn-over temperatures >80 °C make these resonators a great candidate for ultra-stable oven-controlled high-frequency MEMS oscillators.

To my wonderful husband, Mostafa, who has been always a strong source of support, encouragement, and love

ACKNOWLEDGMENTS

First, I would like to greatly acknowledge my advisor, Dr. Reza Abdolvand, for his patience, deep knowledge, and valuable advices. I am also grateful to my committee members Prof. Kalpathy Sundaram, Prof. Vikram Kapoor, Prof. Xun Gong, and Prof. Swaminathan Rajaraman. I would thank all my lab fellows at the Dynamic Microsystems Lab for their corporations and also providing a friendly environment in the lab.

I am also very thankful to my father, Mohammad Ali, and my mother, Zohreh, and my sisters Zahra and Saba for their endless support and love.

TABLE OF CONTENTS

LIST OF FIGURES.....	x
LIST OF TABLES.....	xvii
LIST OF ABBREVIATIONS.....	xix
CHAPTER 1: INTRODUCTION.....	1
CHAPTER 2: BACKGROUND	4
2.1 Transduction Mechanisms.....	4
2.1.1 Electrostatic Transduction	4
2.1.2 Piezoelectric Transduction	6
2.2 TPoS Resonators	9
2.3 MEMS Based Oscillators	10
2.4 Oscillator Stability	12
2.4.1 Non-Deterministic Frequency Stability	12
2.4.2 Deterministic Frequency Stability	13
CHAPTER 3: FABRICATION PROCESS OF THIN FILM PIEZOELECTRIC ON SUBSTRATE RESONATORS.....	14
3.1 Bottom Metal Deposition and Patterning	14
3.2 Piezoelectric Material Deposition.....	15
3.3 Top Metal Deposition and Patterning	16
3.4 Bottom Electrode Access Pad	17
3.5 Gold Over Layer Deposition	18
3.6 Device Stack Etch	19

3.7	Back Side Etching	20
3.8	Device Release	21
 CHAPTER 4: SIDE-SUPPORTED RADIAL-MODE THIN-FILM PIEZOELECTRIC-ON-SILICON DISC RESONATOR.....		
		23
4.1	Analysis of The Radial Mode in SCS	26
4.2	Finite Element Modeling.....	29
4.2.1	Anchor Loss Modeling.....	29
4.2.2	TCF Modeling.....	38
4.3	Fabrication Process.....	42
4.4	Experiment Results	43
4.4.1	Quality Factor Measurements	43
4.4.2	TCF Measurements.....	50
4.5	Harmonic Radial Mode Disc TPoS Resonators	51
4.6	Conclusions	53
 CHAPTER 5: QUASI THICKNESS LAMÉ MODES IN THIN-FILM PIEZOELECTRIC-ON-SILICON RESONATORS		
		55
5.1	Thickness Lamé Mode in TPoS Resonators.....	58
5.2	Harmonic QTLM TPoS Resonators	60
5.3	Quasi Thickness Lamé Mode TPoS Resonator	62
5.3.1	Coupling Efficiency for QTLM TPoS Resonators	62
5.3.2	Support Loss in QTLM TPoS Resonators.....	65
5.3.3	Turn Over Temperature in QTLM TPoS Resonators	68
5.4	Experimental Results	74

5.5	Conclusions	83
CHAPTER 6: TEMPERATURE COMPENSATION OF TPOS RESONATORS USING		
FLUORINE DOPED SILICON OXIDE 85		
6.1	Temperature Compensation with Silicon Dioxide	85
6.2	SiOF Structural Composition	88
6.3	Film Preparation	91
6.3.1	Refractive Index and Extinction Coefficient.....	91
6.3.2	FTIR Absorbance Spectrum.....	93
6.3.3	SIMS Measurements.....	95
6.4	TPOS Resonators Passive Temperature Compensation with Fluorine Doped Silicon Oxide Over Layer	96
6.5	Conclusions	98
CHAPTER 7: CONCLUSIONS AND FUTURE WORKS 100		
7.1	Accomplishments.....	100
7.2	Future Research	103
APPENDIX:PERMISSIONS FOR REUSING THE PUBLISHED PAPERS [23, 53, 93,94]		
IN THE DISSERTATION..... 106		
REFERENCES..... 108		

LIST OF FIGURES

Figure 1. The schematic view of a Lamé mode capacitive resonator on the left and a SEM image of the capacitive resonator [18].	5
Figure 2. The schematic of a first order lateral-extensional piezoelectric resonator (a) and the SEM image of the same resonator [25].	7
Figure 3. The schematic of a TPoS third order lateral extensional resonator (a) and the SEM image of fifth order quasi thickness Lamé TPoS resonator (b).	10
Figure 4. The block diagram for an oscillator circuit.	11
Figure 5. An ideal clock compared to a real clock.	11
Figure 6. The bottom metal deposition and patterning. Molybdenum is the material of choice for bottom metal.	15
Figure 7. A thin layer of AlN is sputtered on the SOI wafer.	16
Figure 8. The top metal Mo sputtered on the AlN and then patterned to create top electrodes and contact pads.	17
Figure 9. The AlN layer is wet etched to create access to the bottom metal.	18
Figure 10. A thin layer of Gold is evaporated and then patterned using lift off for creating ohmic contact.	19
Figure 11. The stack of Mo/AlN/Mo/Si is etched to define the resonator structure.	20
Figure 12. The silicon would be etched from backside of the wafer to create openings beneath the resonators.	21
Figure 13. The resonators are released by etching the Box oxide layer in BOE.	22
Figure 14. The SEM image of two selected resonator presented in this dissertation.	22

Figure 15. The simulated total displacement for first- (a) and fourth- (b) harmonic radial resonance mode of a disc structure made from material with isotropic acoustic velocity. No nodal points on the edge of the disc.	28
Figure 16. The simulated total displacement for first- (a) and fourth- (b) harmonic radial resonance modes of a disc structure made on a [100] single crystalline silicon substrate. Pseudo-nodal points appear on the edges for higher harmonics (e.g. fourth-harmonic)	28
Figure 17. The simulated total displacement for fourth-order radial-mode SCS disc resonator with tethers aligned to [100] crystalline plane (a) and with tethers aligned to [110] crystalline plane (b) with fixed boundary condition at the outer edges of the tethers.	29
Figure 18. The meshed resonant structure (a) and the stress field for the fundamental in-plane bending mode of a cantilever (b) modeled in COMSOL. The complex eigenfrequency is utilized to calculate the Q.	33
Figure 19. The anchor Q as a function of PML scaling factor for a cantilever beam resonator (similar to Figure 18). The minimum Q is assumed to be the most accurate.	35
Figure 20. The meshed resonant structure (a) and the stress field (b) for a radial-mode TPoS disc resonator modeled in COMSOL. The PML and the substrate radiuses are adjusted to λ and 2λ for each harmonic mode.....	35
Figure 21. The stress field for 2nd (a), 3rd (b), 4th (c), 5th (d) and 8th (e) order radial mode disc resonator.....	37

Figure 22. The simulated temperature-frequency dependency for radial mode disc resonator fabricated on n-type doped silicon ($n=6 \times 10^{19} \text{cm}^{-3}$) compared with width-extensional resonators oriented in two different directions.....	40
Figure 23. The schematic of a TPoS disc resonator fabricated in this study.	42
Figure 24. The recorded S21 for a UNCD radial-mode TPoS disc resonator simultaneously presenting the resonance peaks of 2nd, 3rd harmonics with their corresponding Q.....	46
Figure 25. The recorded S21 for a SCS radial-mode TPoS disc resonator with tethers aligned to [100] direction measured in partial vacuum simultaneously presenting the resonance peaks of 2nd, 3rd, 4th, 5th and 8th harmonics with their corresponding Q..	47
Figure 26. The frequency-temperature plot measured for a radial-mode TPoS disc resonator and extensional mode TPoS resonators aligned to [100] and [110] silicon planes.....	51
Figure 27. The SEM photo for the 4 th harmonic radial mode TPoS disc resonator.	52
Figure 28. The measured frequency response for a 4 th harmonic radial mode disc TPoS resonator. Lower motional resistance is measured compared to design with just two electrodes.....	53
Figure 29. The simulated stress field in the x and y directions for a pure AlN planar Lamé mode. In each half vibration cycle, stress field is tensile in one planer axis and compressive in the other axis (dark blue and dark red indicate maximum opposing stress in the center). Therefore, such planar Lamé mode cannot be efficiently excited with thin polycrystalline films laid on top of the resonator body.	58

Figure 30. The displacement field for a silicon resonator with thickness (T) and different finger pitches. For the finger pitches close to the thickness of the resonator, Lamé mode (d) would replace lateral extensional mode (a) in the resonator slab. For the finger pitches close to a fraction of the thickness of the resonator, higher harmonic Lamé are actuated in the resonator slab (second harmonic (e) and third harmonic (f)).	59
Figure 31. The piezoelectric polarization field (a) and asymmetric electrode design (b)	61
Figure 32. A schematic view graph of a third-order QLM TPoS resonator. Electrode patterns are the same as the ones for lateral extensional mode.	61
Figure 33. The stress field in the fundamental a) and third harmonic QTLM resonators. The stress field in the piezoelectric portion of the third harmonic mode is larger and because of that higher coupling efficiencies are expected for third harmonic QLM.	62
Figure 34. The modeled admittance for a third order QLM TPoS resonator. The coupling efficiencies are calculated using the series and parallel frequencies.	63
Figure 35. The admittance modeled for a fourth harmonic QTLM TPoS resonator with 4 μm silicon topped with 2 μm AlN.	65
Figure 36. The PML based model developed for support loss prediction for a fundamental QLM TPoS resonator with an acoustic isolation frame. The resonator and frame dimensions are chosen to resemble the fabricated resonators.	67
Figure 37. On a [100] silicon wafer, for the resonators aligned to [100] crystalline plane, should be rotated 45 degrees. All the faces of the resonator block are [100] which would be similar to the Lamé mode.	68

Figure 38. The modeled TCF curves for resonators with FP 40, 30 and 17 μm . The turn-over temperature shifts toward higher temperature as the FP/ T ratio approaches unity. Quasi Lamé mode shows the highest and lateral-extensional mode shows the lowest turn-over temperatures.....	72
Figure 39. The Turn-over temperature of a QLM TPoS resonator as a function of FP/T ratio. Higher turn-over temperature is predicted for the resonators with FP/T ratio closer to one. The turn-over temperature could be adjusted lithographically.	73
Figure 40. The measured frequency response in air for the fundamental QTLM TPoS resonator with and without acoustic isolation frame in air. The unloaded quality factor improved significantly by adding an isolation frame.	75
Figure 41 .The measured frequency response for the fundamental QTLM TPoS resonator in partial vacuum. Unloaded quality factor of 23.2 k is measured at 185 MHz for this resonance mode.....	76
Figure 42. The measured frequency response for a 2nd harmonic QTLM TPoS resonator in air.	77
Figure 43. The measured frequency response for a 3rd harmonic QTLM TPoS resonator in air.	77
Figure 44. The wide spectrum frequency response for a second harmonic QLM TPoS resonator. There are no other strong peak close to this mode which make it a good candidate for oscillator application.	78
Figure 45. The measured CF curves for lateral-extensional, and quasi thickness Lamé mode resonators.	80

Figure 46. The measured frequency response for a quasi-thickness Lamé mode resonator with $FP=30\text{ }\mu\text{m}$	83
Figure 47. Si atom surrounded with four oxygen atom in a tetrahedral structure in SiO_2	89
Figure 48. Threefold SiO_2 ring in the presence of Fluorine and without Fluorine.	89
Figure 49. Transition of lower order rings to relaxed higher order rings in the presence of active Fluorine in the plasma.....	90
Figure 50. The Refractive index measured by ellipsometer for films deposited with different NF_3 partial pressure.....	92
Figure 51. The Extinction coefficient of the films deposited with different NF_3 partial pressure.	92
Figure 52. The normalized FTIR spectrum measured for different sputtered silicon oxide layers.....	94
Figure 53. The Fluorine concentration profile measured for different sputtered Fluorine doped SiO_2	95
Figure 54. The schematic of TPoS resonators used for Fluorine doped oxide over layer deposition.	96
Figure 55. The stress field for the first order (a) and third order (b) Lateral extensional mode.	97
Figure 56. The frequency response of the TPoS resonators with and without oxide for (a) Fluorine doped silicon oxide and (b) pure silicon oxide.....	97

Figure 57. The measured frequency drift for LE TPoS resonators with different silicon oxide over layer. Resonators with Fluorine doped oxide over layer has almost two times better temperature stability over the measured temperature range.....	98
Figure 58. The Schematic of the proposed ovenized TPoS oscillator.	103
Figure 59. The proposed high order QTLM TPoS resonator.	104

LIST OF TABLES

Table 1. Anchor quality factor for bending mode beam resonator	32
Table 2. Simulated and fabricated resonator dimensions.....	34
Table 3. Simulated anchor quality factor for radial mode disc resonators.	36
Table 4. Simulated support Q for tether with variable length.....	39
Table 5. Elastic constants of phosphorus doped ($N=6 \times 10^{19} \text{CM}^{-3}$) silicon and their corresponding first and second order temperature coefficients [16].....	41
Table 6. Measured quality factor data for radial mode disc resonators.	45
Table 7. Measured data for single crystalline silicon disc resonator with tethers aligned to [100] direction.....	49
Table 8. Comparison of the best results reported in this work with selected published data in the same frequency range.....	50
Table 9. The modeled coupling efficiencies for TPoS resonators. A full stack of Mo/AlN/Mo/Si is considered with the same thickness of the fabricated resonators ($0.1 \mu\text{m}$ μm Mo/ $1 \mu\text{m}$ ScAlN/ $0.1 \mu\text{m}$ Mo/ $16 \mu\text{m}$ Si).....	64
Table 10. The modeled anchor quality factor for the resonator with and without acoustic isolation frame.....	67
Table 11. The elastic constants of Phosphorus-Doped ($n=6.6 \times 10^{19} \text{cm}^{-3}$) Silicon and their corresponding first and second order temperature coefficients [16].....	70
Table 12. The measured coupling efficiencies for different classes of TPoS resonator.	79
Table 13. The measured quality factor for the fundamental QTLM TPoS resonator compared to a selected published results in the same frequency range.....	81

Table 14. The measured data for Lateral extensional mode compared to QTLM resonators with properties transitioning from LE to QTLM.	82
--	----

LIST OF ABBREVIATIONS

ABC	Absorption Boundary Condition
ADS	Advanced Design System
AlN	Aluminum Nitride
BAW	Bulk-Acoustic-Wave
CLM	Cross-sectional Lamé Mode
CMOS	Complementary Metal-Oxide-Semiconductor
FEM	Finite Element Model
FTIR	Fourier Transform Infrared Spectroscopy
HF	Hydrofluoric acid
HFCVD	Hot Filament Chemical Vapor Deposition
IC	Integrated Circuit
ICP	Inductive Coupled Plasma
LE	Lateral Extensional
MEMS	Micro-Electro-Mechanical Systems
Mo	Molybdenum
PCB	Printed Circuit Board
PML	Perfectly Matched Layer
Q	Quality Factor
RMS	Root Mean Square
ScAlN	Scandium Aluminum Nitride
SCS	Single Crystalline Silicon

SEM	Scanning Electron Micrograph
Si	Silicon
SiO ₂	Silicon Oxide
SNR	Signal to Noise Ratio
SOI	Silicon On Insulator
TCE	Temperature Coefficient of Elasticity
TCF	Temperature Coefficient of Frequency
TPoS	Thin-Film Piezoelectric-on-Substrate
TQLM	Thickness Quasi Lamé Mode
VHF	Very High Frequency
UNCD	Ultra Nano Crystalline Diamond

CHAPTER 1: INTRODUCTION

Since the invention of Micro-electro-mechanical systems (MEMS) in 1960's, their application in different microelectronic market has been continuously growing over the past decades. Recently, MEMS seize a fair share in inertial sensors, gyroscopes, filter and recently timing commercial market. Their application could vary from gyroscopes [1] [2], accelerometers [3] [4], sensors [5] [6] [7] [8], bio sensors and microfluidic devices [9] [10], filters [11] [12] to oscillators in timing applications [13] [14] [15].

Oscillators generate a synchronizing heartbeat signal in most electrical devices (frequency clock in data transmission, frequency up and down transmission in RF transceivers (radio frequency communication), global positioning systems and etc). The two essential components of an oscillator are an amplifier and a frequency-selective component (i.e. resonator) that is placed in the amplifier feedback loop. For decades, off-chip quartz crystals had dominated the oscillator market as the frequency-selective component. Recently, MEMS resonators have been receiving great deal of attention as a candidate for replacing quartz in certain applications due to offering extremely small packages and a potential for integration with microelectronic circuits on the silicon substrate. In addition to what mentioned above, MEMS based oscillators has additional advantages such as lower sensitivity to acceleration due to their smaller size, Lower Electromagnetic (EM) sensitivity and slower aging.

Regardless of the specific application, the resonator quality factor (Q) directly impacts the system performance as it basically determines the noise floor [14]. However,

optimization of quality factor is a complicated process as the physics of loss is not fully understood and hard to control in most cases.

This dissertation is prepared in seven chapters. The current chapter, chapter one, provides an introduction to the work presented in this dissertation. In chapter two, a background would be presented to the basic concepts of MEMS resonators specifically thin film piezoelectric on silicon (TPoS resonators), different transduction mechanisms and etc. In Chapter three, a detailed fabrication process for the devices presented in this dissertation is presented. The fabrication difficulties and also the solutions to overcome these problems are discussed thoroughly. A method to improve the quality factor for side supported piezoelectric disc resonators is presented in chapter four. These resonators are fabricated with TPoS (AlN on Silicon) topology. The preliminary results are presented and the quality factor data for these resonators are compared with the data for the resonators in the same frequency range. Thickness Quasi Lamé Mode (TQLM) resonators are introduced in chapter five. TQLM resonators are a new class of MEMS resonators. The quality factor for this vibration mode in TPoS resonators is also explored for these resonators. The Temperature Coefficient of Frequency (TCF) is also studied and above 80 °C turn-over temperature is also reported for these piezoelectric resonators without the need for any additional oxide layer for the first time. In chapter six, a new method for depositing Fluorine doped silicon oxide is studied and also these films are used as an over layer in passive temperature compensation of TPoS resonators. Two times better thermal stability is measured compared to the resonators with pure oxide

over layer and finally, accomplishment in this dissertation would be briefly presented and potential future directions would be pointed out in Chapter seven.

CHAPTER 2: BACKGROUND

2.1 Transduction Mechanisms

In MEMS resonators, first the electrical signal would be transformed to mechanical vibration and again that mechanical vibration is detected as an electrical signal in the output. There are different kind of transduction mechanism to link energy in the mechanical and electrical domain. These transduction mechanisms can be categorized as follow:

- Piezoelectric transduction
- Electrostatic transduction
- Thermal transduction

Electrostatic and piezoelectric transductions are the most common excitation methods for MEMS resonators. These two classes of MEMS resonator are introduced in more detail in the following sections.

2.1.1 Electrostatic Transduction

Electrostatic transduction is used in the capacitive resonators to actuate the resonance mode in the resonator structure. In these resonators, there is a narrow gap between the conductive resonator body and electrodes Figure 1. A DC polarization voltage is needed to effectively actuate the resonance mode using the capacitive transduction. For the capacitive resonators, the resonators are fabricated out of low loss acoustic materials such as single crystalline silicon and these resonators are made of single layer materials

and because of that quality factors as high as few millions are reported for these resonators [16]. Because of the narrow gaps and large squeeze air damping loss, these resonators are needed to operate in vacuum [17].

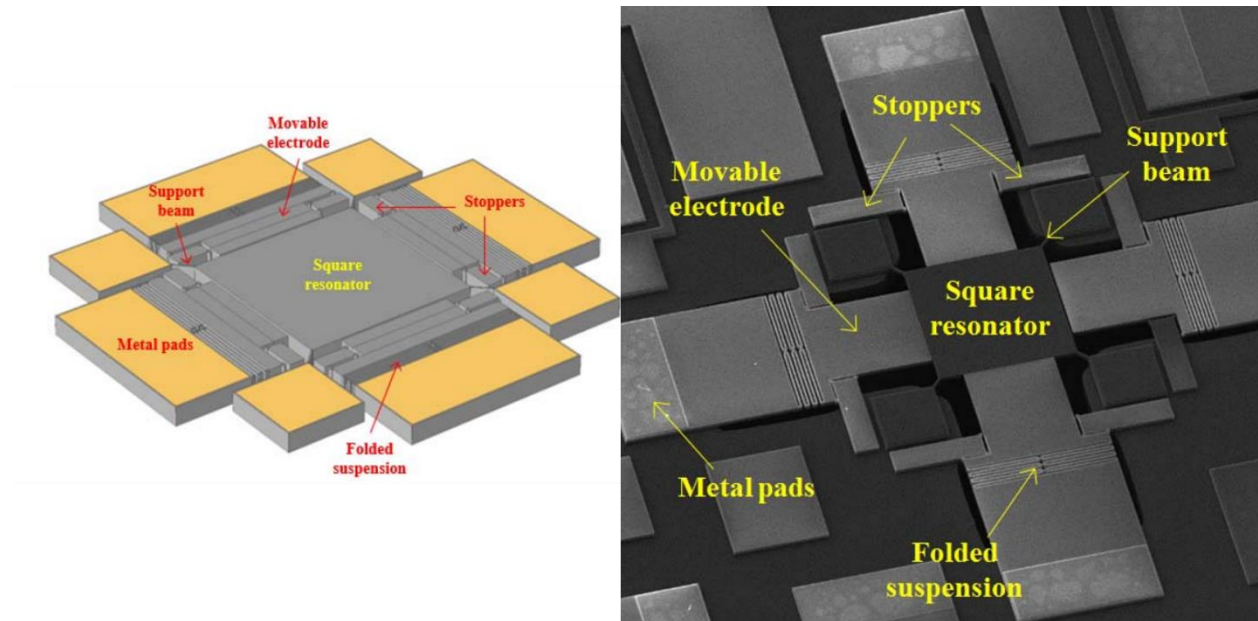


Figure 1. The schematic view of a Lamé mode capacitive resonator on the left and a SEM image of the capacitive resonator [18].

The motional impedance in the MEMS resonators are inversely proportional to quality factor and electromechanical coupling of the resonator. Despite the high quality factor of the capacitive resonators, very low coupling efficiencies of these resonators would cause high motional impedance. To improve the coupling efficiency, one should increase the overlap area or reduce the gap between the resonator and the actuation electrodes [19] [20]. Both these methods have limitations caused by fabrication limits. This problem would escalate as the frequency increases. In another technique, coupling efficiency would be

improved by filling these narrow gaps with high permittivity dielectric material however with this method both parasitic capacitance and quality factor are affected negatively [21] [22]. Despite all the progress in improving electromechanical coupling of the capacitive resonators, the main drawback of this class of MEMS resonators is still their relatively large motional resistance.

2.1.2 Piezoelectric Transduction

With piezoelectric transduction, electrical and mechanical energies are coupled using piezoelectric materials. All material with non-centrosymmetric crystalline structure would show piezoelectricity to some extent. Applying pressure to a piezoelectric material would create charge on this materials (direct piezoelectric effect) and also a piezoelectric material would deform in the presence of an electric field (reverse piezoelectric effect). The general constitutive equations of piezoelectricity would define how the electrical and mechanical energies are coupled for piezoelectric materials and are as follow:

$$D = d T + \varepsilon^T E \quad (2-1)$$

$$S = s^E T + d^t E \quad (2-2)$$

Where D is the electrical displacement, d is piezoelectric constant, T is stress, ε^T is permittivity at a constant stress, E is electric field, S is strain and s^E is compliance at a constant electric field. In these equations $D_{3 \times 1}$, $S_{6 \times 1}$ and $T_{3 \times 1}$ are vectors and the constants are tensors ($d_{3 \times 6}$, $\varepsilon_{3 \times 3}$, $s_{6 \times 6}$).

Equation (2-1) can be expanded as follow:

$$\begin{bmatrix} D_1 \\ D_2 \\ D_3 \end{bmatrix} = \begin{bmatrix} d_{11} & d_{12} & d_{13} & d_{14} & d_{15} & d_{16} \\ d_{21} & d_{22} & d_{23} & d_{24} & d_{25} & d_{26} \\ d_{31} & d_{32} & d_{33} & d_{34} & d_{35} & d_{36} \end{bmatrix} \begin{bmatrix} T_1 \\ T_2 \\ T_3 \\ T_4 \\ T_5 \\ T_6 \end{bmatrix} + \begin{bmatrix} \varepsilon_{11} & \varepsilon_{12} & \varepsilon_{13} \\ \varepsilon_{21} & \varepsilon_{22} & \varepsilon_{23} \\ \varepsilon_{31} & \varepsilon_{32} & \varepsilon_{33} \end{bmatrix} \begin{bmatrix} E_1 \\ E_2 \\ E_3 \end{bmatrix} \quad (2-3)$$

Piezoelectric resonators are constructed of a piezoelectric layer either sandwiched between two conductive electrode layers (transverse field excitation) [23] or beneath conductive layer (lateral field excitation) [24]. Electric field would be applied to the piezoelectric layer through these conductive electrodes and when the frequency of the applied electric field match one of the natural resonance frequencies of the resonator structure the resonance mode would be excited. A piezoelectric resonator is shown in Figure 2.

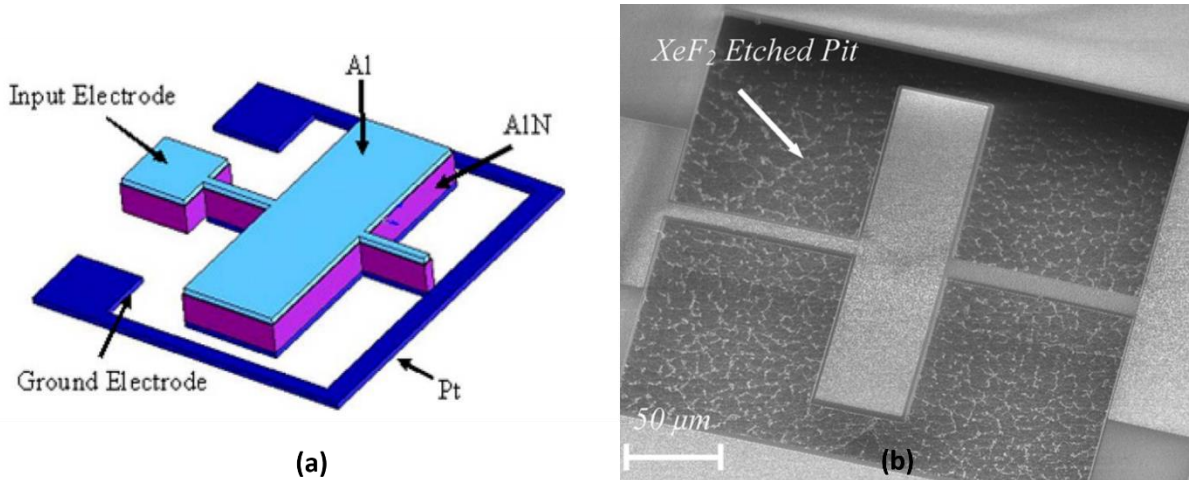


Figure 2. The schematic of a first order lateral-extensional piezoelectric resonator (a) and the SEM image of the same resonator [25].

Due to strong electromechanical coupling efficiencies of piezoelectric resonators, the motional impedance of these resonators are considerably smaller than their capacitive counterparts, specifically for higher frequencies. With piezoelectric transduction, GHz resonators could be implemented effortlessly while it was out of reach with capacitive transduction. In this dissertation Aluminum nitride (AlN) and Scandium doped AlN (ScAlN) are used as the piezoelectric material for transduction of vibrational modes. The piezoelectric coefficient matrix of AlN is as follow [26]:

$$\begin{bmatrix} 0 & 0 & 0 & 0 & d_{15} & 0 \\ 0 & 0 & 0 & d_{15} & 0 & 0 \\ d_{31} & d_{32} & d_{33} & 0 & 0 & 0 \end{bmatrix} (Cm^{-2}) = \begin{bmatrix} 0 & 0 & 0 & 0 & -0.48 & 0 \\ 0 & 0 & 0 & -0.48 & 0 & 0 \\ -0.58 & -0.58 & 1.55 & 0 & 0 & 0 \end{bmatrix} \quad (2-4)$$

Although AlN has lower coupling efficiencies compared to other piezoelectric materials such as Zinc oxide (ZnO) and Lithium Niobate (LiNbO₃) but due to their high acoustic velocity, ease of fabrication (CMOS-compatible) and their high electrical resistivity, AlN and ScAlN are great candidates for piezoelectric MEMS resonators. The ScAlN film can be sputtered such as AlN film. Larger coupling efficiencies are reported for the resonators with ScAlN as the piezoelectric layer compared to pure AlN resonators [27].

On the other hand, the quality factor of the piezoelectric resonators is smaller than capacitive ones. Common piezoelectric materials such as Lead Zirconium Titanate (PZT), Lithium Niobate (LiNbO₃) , Aluminum Nitride (AlN), Scandium doped AlN (ScAlN) and etc. are not low loss materials and in addition interface loss would also be strong due to the scattering of energy between electrodes and piezoelectric layer for these resonators

hence the quality factor of the piezoelectric resonators are considerably smaller than the capacitive resonators.

2.2 TPoS Resonators

Thin film piezoelectric on substrate (TPoS) resonators are a subclass of piezoelectric resonators. In this resonators, a layer of piezoelectric material is sandwiched between two metallic electrode layer is placed on top of a relatively thick substrate. The substrate material is often a low acoustic loss material with high acoustic velocity and high energy density such as single crystalline silicon or Diamond [12] [28]. A schematic view graph and SEM image of a TPoS resonator is shown in Figure 3.

Since a big portion of the resonator is made out of low loss material, TPoS resonators quality factor is larger than pure piezoelectric resonators [29] and in addition due to large coupling efficiency of the piezoelectric layer, the motional impedance of these resonators are considerably smaller than the capacitive resonators. These TPoS resonators offer the advantages of both piezoelectric and capacitive worlds. These resonators have better power handling compared to both capacitive and piezoelectric resonators. [30] and also the temperature coefficient of frequency can also be smaller compared to Piezoelectric resonators [31].

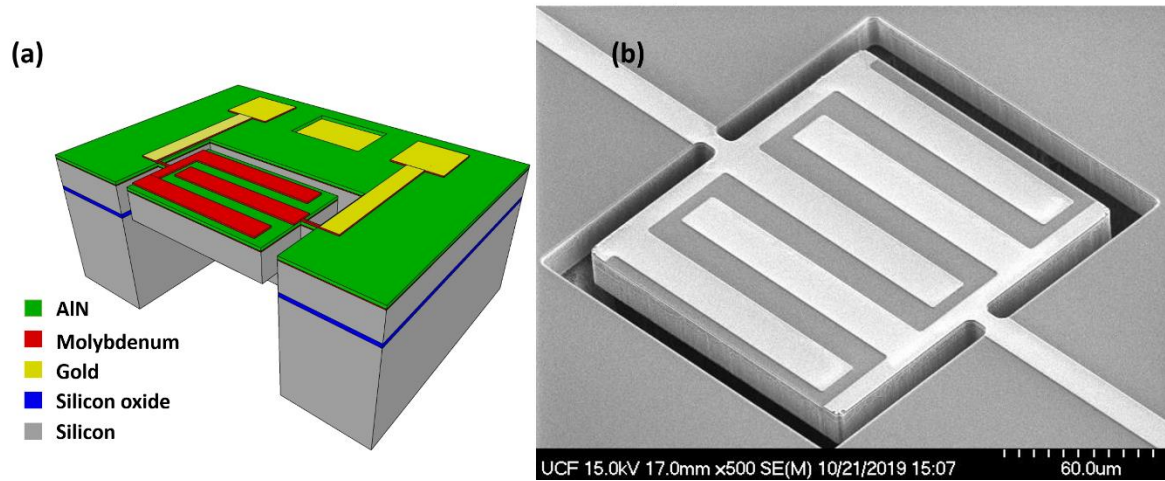


Figure 3. The schematic of a TPoS third order lateral extensional resonator (a) and the SEM image of fifth order quasi thickness Lamé TPoS resonator (b).

2.3 MEMS Based Oscillators

Oscillators are the heartbeats of most electrical systems and they are constructed of an amplifier circuitry with a frequency selective component (resonator) in the feedback (Figure 4). One of the main measures for the oscillators is the jitter (Figure 5). Resonator quality factor is directly affecting jitter and hence mechanical resonators are preferred to electrical counterparts in stable oscillator applications due to their larger quality factors [32].

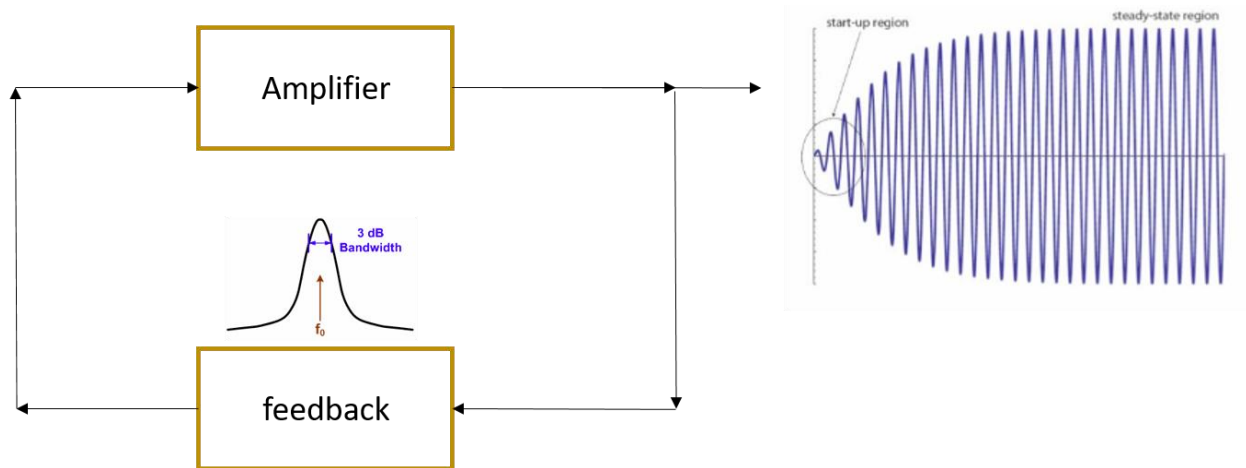


Figure 4. The block diagram for an oscillator circuit.

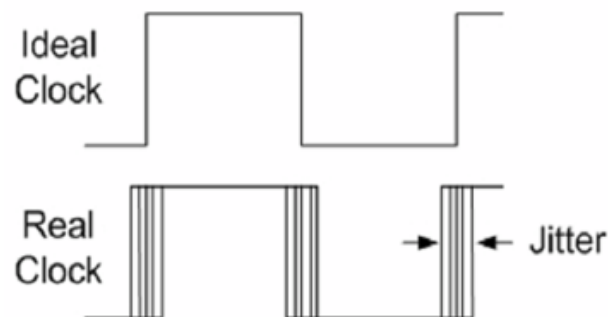


Figure 5. An ideal clock compared to a real clock.

For decades off-chip quartz crystals have dominated the oscillator market. Recently MEMS resonators have been studied thoroughly as a replacement for quartz crystals and they are started to replace quartz crystals in the oscillator commercial market as well due to their small size, the fact that these MEMS resonators could be fabricated along with other circuits on the same chip, their lower vibration and electromagnetic interference sensitivity, their lower defective part per million and their better mean time between failure. In addition to all of that, these resonance frequency of the MEMS resonators could go as high as few GHz while the resonance frequency of Quartz crystals

are limited to few hundreds of MHz. The quality factor and thermal stability of these resonators would greatly impact the oscillator performance.

2.4 Oscillator Stability

The stability of the oscillators could be classified into non-deterministic and deterministic frequency stability [33].

2.4.1 Non-Deterministic Frequency Stability

The frequency spectrum of any oscillator is expected to have only one single frequency. Non-deterministic short term noises such as flicker noise and white noise in the oscillator circuit would cause frequency fluctuation in short term and also would widen the oscillator spectrum. These noises would define the oscillator jitter and phase noise. RMS jitter could be calculated by integrating a frequency band of the phase noise spectrum.

The effect of oscillator component on the phase noise can be explained with Leeson model [34]. Based on Leeson model oscillator phase noise can be estimated with following formula:

$$\Gamma(f) = \frac{FKT}{2P_0} \left(\frac{1}{4 \times Q_{loaded}^2} \left(\frac{f_s}{f} \right)^2 + 1 \right) \quad (2-5)$$

Where $\Gamma(f)$ is the oscillator phase noise at frequency offset f from carrier, F is the noise figure of the amplifier, k is Boltzmann's constant, T the absolute temperature f_s is

the carrier frequency and Q_{loaded} is the loaded quality factor. These short term circuit noise would be filtered by the frequency selective component in the feedback and as the quality factor of this frequency selective component is higher, the better this noise would be filtered which would translate into lower jitter and phase noise.

2.4.2 Deterministic Frequency Stability

The oscillation frequency should be stable over a long period of time. The oscillation frequency would be defined by the resonance frequency of the resonator in the feedback. The resonance frequency of the resonator is dependent on the material properties of the resonator such as stiffness and density of the film. External parameters such as aging, temperature, vibration and etc. would affect these material properties and hence would affect the stability of these oscillators.

In this dissertation, both deterministic and non-deterministic oscillator stability is addressed by designing resonators with both high quality factor and high thermal stability. TPoS platform is chosen for the resonator design due to their superior quality factor compared to pure piezoelectric resonators. TPoS resonators are great candidates for oscillator applications because of their relatively high quality factor, low motional resistance, high power handling and the fact that their temperature dependent frequency fluctuations could be passively compensated with doping the silicon in the resonator stack.

CHAPTER 3: FABRICATION PROCESS OF THIN FILM PIEZOELECTRIC ON SUBSTRATE RESONATORS

In this chapter the process flow for the fabrication of the TPoS resonators is discussed. The fabrication process in each step is explained in detail and solutions for practical problem is pointed out and solved.

The TPoS resonators are fabricated on SOI wafer in a six mask process. All the processes are low temperature. The thickness and resistivity of the silicon device layer are chosen based on the designs for TCF and quality factor. In the upcoming sections, each fabrication step is discussed in detail.

3.1 Bottom Metal Deposition and Patterning

As shown in Figure 6, the first step is bottom metal layer deposition and patterning. The bottom metal is sputtered and then dry etched in SF_6/O_2 plasma with RIE (Reactive Ion Etching) to form the opening under the pads to reduce the parasitic capacitances.

The bottom material would act as a seed layer for the sputtered piezoelectric material on top and because of that it is crucial to pay careful attention in choosing a suitable metal material for the bottom metal. This bottom metal would also be exposed to Buffered Oxide Etchant (BOE) or Hydrofluoric acid in the next fabrication steps. Therefore, this metal should not be etched with BOE and HF or have a slow etch rate in these solutions. Molybdenum is chosen for the metal layer due to its small lattice and thermal expansion coefficient mismatch with piezoelectric material of choice in this work (Aluminum Nitride (AlN)) [35], low acoustic loss and high acoustic velocity [36] and slow etch rate in BOE

and HF. Molybdenum can get oxidize at relatively low temperature [37] and because of that the next fabrication steps should be designed carefully.

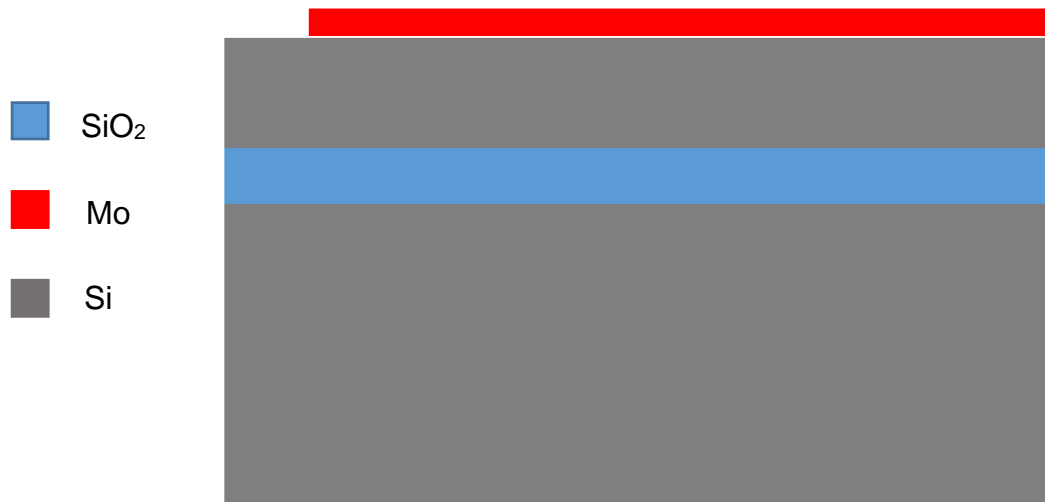


Figure 6. The bottom metal deposition and patterning. Molybdenum is the material of choice for bottom metal.

3.2 Piezoelectric Material Deposition

Zinc Oxide (ZnO), Aluminum Nitride (AlN), Scandium doped AlN (ScAlN), Lithium Niobate (LiNbO₃) and Lead zirconate titanate (PZT) are the common piezoelectric materials used in Piezo-MEMS resonators. Although piezoelectric materials such as PZT and LiNbO₃ offers high piezoelectric coefficients, their fabrication processes are troublesome and not compatible with CMOS process. Fabrication process of AlN and ScAlN on the other hand, compatible with the CMOS process. In addition to their straight forward fabrication process, their high acoustic velocity, high electrical resistivity and moderate Temperature Coefficient of Elasticity (TCE) are the reasons behind our choice of AlN and ScAlN as piezoelectric material for the devices presented in this dissertation.

A thin layer of AlN/ScAlN is sputtered on the bottom metal layer as shown in Figure 7. The piezoelectric layers deposited in this work is sputtered on the SOI wafer by AM Systems INC.

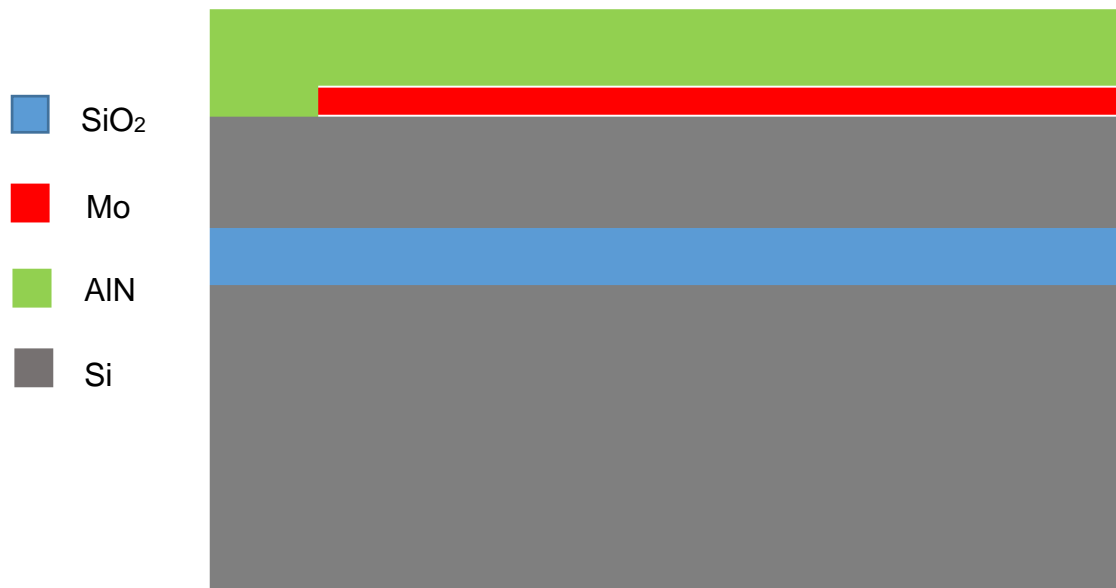


Figure 7. A thin layer of AlN is sputtered on the SOI wafer.

3.3 Top Metal Deposition and Patterning

The top metal is also sputtered on top of the deposited AlN. Molybdenum is used for the top metal as well. The deposited metal layer then patterned to create the top layer electrodes and contact pads for probing and wire bonding. S1813 is used as the positive photoresist to create a soft mask for the top metal etch. Molybdenum again etched in SF₆/O₂ plasma.



Figure 8. The top metal Mo sputtered on the AlN and then patterned to create top electrodes and contact pads.

3.4 Bottom Electrode Access Pad

In this step the piezoelectric layer (AlN or ScAlN) is wet etched to create access to the bottom metal. This opening would be used to apply electrical signal to the piezoelectric material for transverse filed excitation of the resonators. These bottom metal pads could be used for wire bonding or micro probe measurements.

A 500 nm thick silicon oxide is deposited with PECVD. The Oxide layer is then patterned using PR1-4000 positive photoresist and the silicon oxide layer is etched with CF₄/O₂ plasma in RIE. This silicon oxide hard mask is then used for wet etching of AlN in heated (80 °C) MF3-19 developer (Figure 9). For 20% Scandium doped AlN, an alteration of Heated MF3-19 and Sulfuric acid is used to etch the ScAlN layer. With this alteration, ScAlN is etched with a rate of 200 nm/minute.

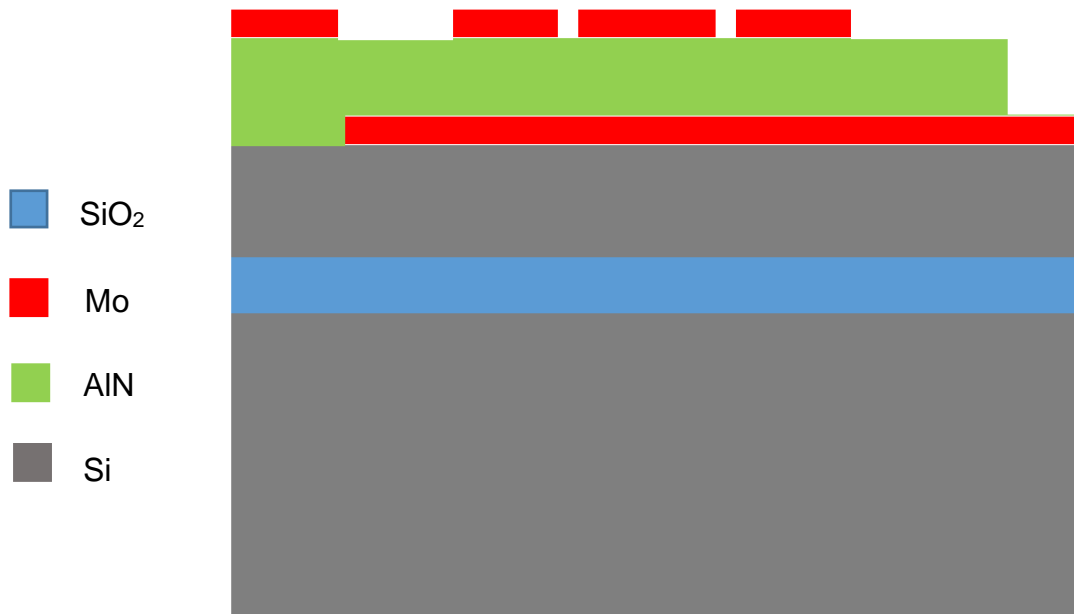


Figure 9. The AlN layer is wet etched to create access to the bottom metal.

3.5 Gold Over Layer Deposition

A thin layer of Gold is deposited on the pads to create good ohmic contact for probing and also for ease of wire bonding. A very thin layer of Titanium (25 nm) is evaporated before Gold deposition for creating good adhesion between Molybdenum and Gold layers. After that, a 75 nm gold layer is evaporated using E-Beam and then patterned using Lift off (Figure 10).

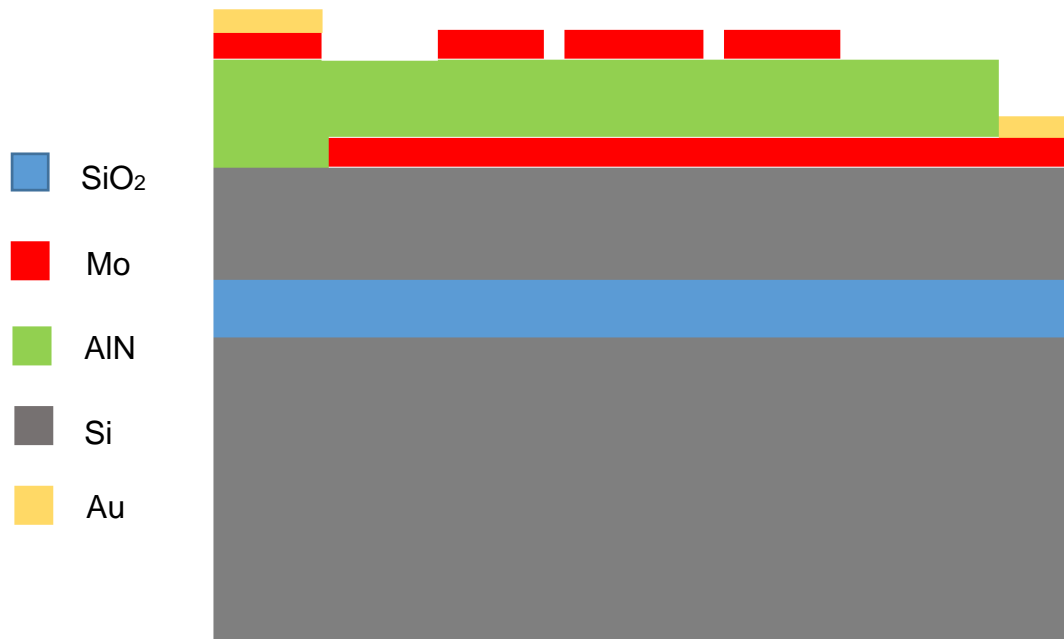


Figure 10. A thin layer of Gold is evaporated and then patterned using lift off for creating ohmic contact.

3.6 Device Stack Etch

The Mo/AlN/Mo/Si stack is etched in this step to define the resonator structures. The AlN (or ScAlN) is dry etched in Chlorine/Argon plasma in an inductive Coupled Plasma (ICP) tool. For this step photoresist mask could not be used since the photoresist mask would be etched fast in Cl₂ plasma. An oxide hard mask is used for this step. Again 3 μm to 4 μm of silicon oxide is deposited on the wafer. The thickness of Silicon oxide layer is dependent on the thickness of AlN, whether we are etching ScAlN or AlN and also the thickness of silicon device layer underneath. The silicon oxide layer is then etched in CF₄/O₂ plasma in an ICP tool. For dry etching ScAlN, an Cl₂/ Ar/ BCl₃ plasma is used and the ScAlN layer is etched with an etch rate of 100 nm/ minute and selectivity of 1:1 for ScAlN/ Silicon oxide layer.

The Silicon layer is then etched in SF_6 plasma with a Bosch process in an DRIE STS tool. An SOI recipe is used to prevent notching.

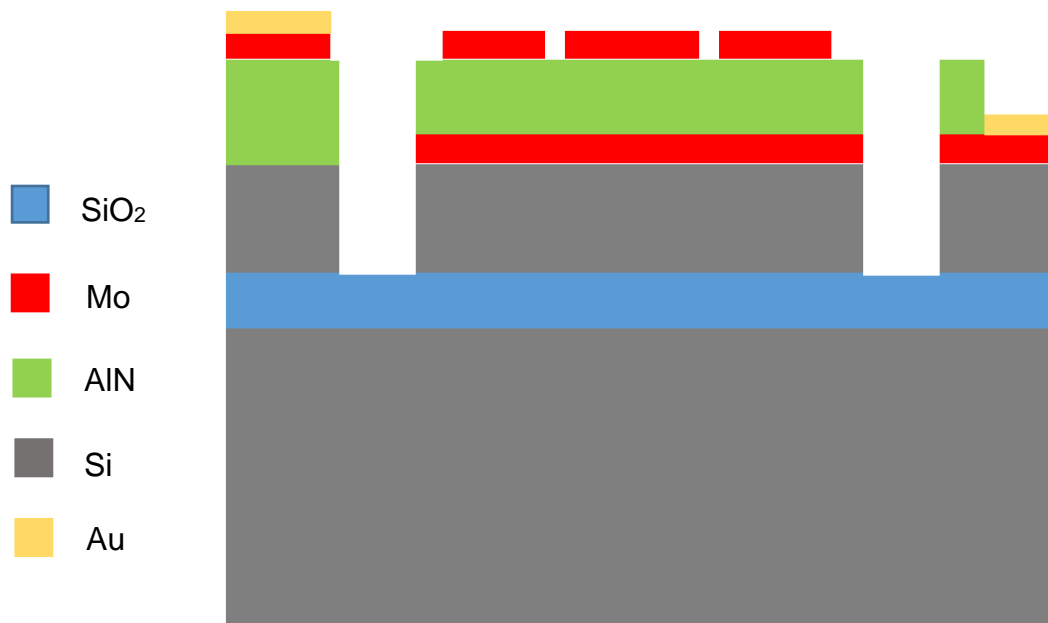


Figure 11. The stack of Mo/AlN/Mo/Si is etched to define the resonator structure.

3.7 Back Side Etching

In this step release holes would be etched from the back side of the silicon wafer to create opening underneath the resonator device layer. The silicon is again etched in SF_6 plasma with Bosch process in a DRIE STS tool. The Box Oxide layer would act as an etch stop for silicon etch (Figure 12).

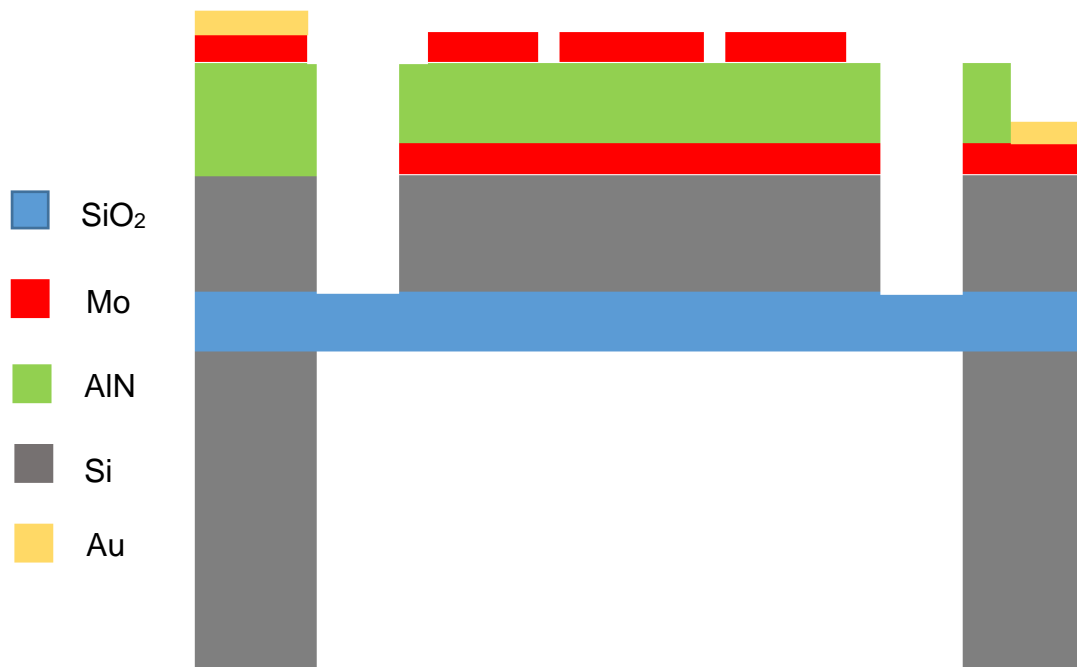


Figure 12. The silicon would be etched from backside of the wafer to create openings beneath the resonators.

3.8 Device Release

In the last fabrication step, the resonators are released by etching the Box oxide layer in BOE. After the devices are released. This BOE etch would etched all the silicon layers remained on the top side of the wafer as well as the Box oxide.

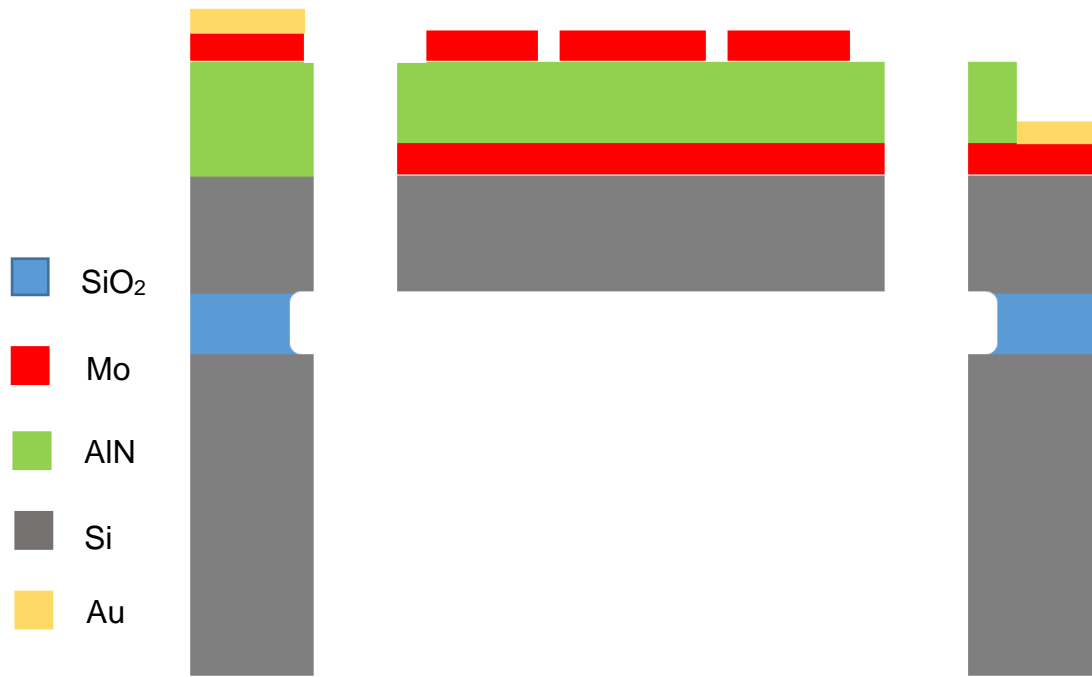


Figure 13. The resonators are released by etching the Box oxide layer in BOE.

The Scanning Electron Microscopy(SEM) image of some of the selected resonators fabricated for this dissertation is shown in Figure 14.

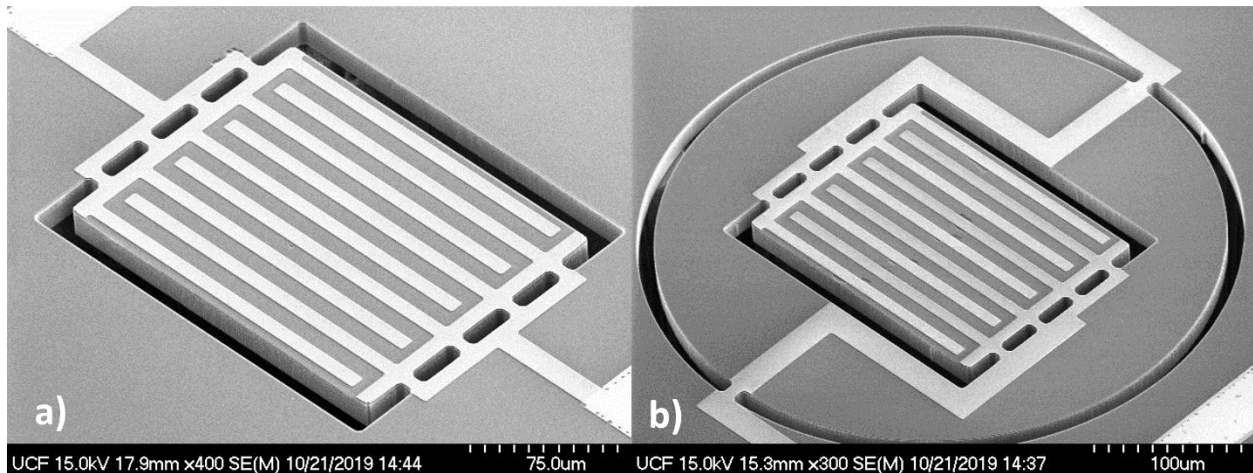


Figure 14. The SEM image of two selected resonator presented in this dissertation.

CHAPTER 4: SIDE-SUPPORTED RADIAL-MODE THIN-FILM PIEZOELECTRIC- ON-SILICON DISC RESONATOR

1

Regardless of the specific application, the resonator quality factor (Q) directly impacts the system performance as it basically determines the noise floor [14]. However, optimization of quality factor is a complicated process as the physics of loss is not fully understood and hard to control in most cases. Quality factor is a measure of energy loss in a resonance system. Energy loss in resonators could be categorized into two general groups of intrinsic and extrinsic losses [38]. Intrinsic losses are principally linked to the material properties whereas extrinsic losses strongly depend on design and implementation of the resonators. Dielectric loss ($1/Q_{die}$), phonon-phonon interaction loss ($1/Q_{p-p}$), which includes Akheiser loss [39] and thermo-elastic dissipation (TED) [40] are examples of intrinsic loss in resonators. On the other hand, anchor loss ($1/Q_{anc}$), air/fluid damping loss ($1/Q_{air}$), ohmic loss ($1/Q_{ohm}$), and interface losses ($1/Q_{interface}$) are examples of extrinsic loss in resonators and these losses could be reduced by proper design and operation in controlled environment (e.g. operation in partial vacuum). The overall Q of the resonator could be written as a function of these different loss components:

¹ Material used in this chapter is partially taken from the published papers:

- S. Shahraini, M. Shahmohammadi and R. Abdolvand, "Support loss evasion in breathing-mode high-order silicon disc resonators," *2017 IEEE International Ultrasonics Symposium (IUS)*, Washington, DC, 2017, pp. 1-4.
- S. Shahraini, M. Shahmohammadi, H. Fatemi and R. Abdolvand, "Side-Supported Radial-Mode Thin-Film Piezoelectric-on-Silicon Disk Resonators," in *IEEE Transactions on Ultrasonics, Ferroelectrics, and Frequency Control*, vol. 66, no. 4, pp. 727-736, April 2019.

$$\frac{1}{Q_{tot}} = \frac{1}{Q_{die}} + \frac{1}{Q_{p-p}} + \frac{1}{Q_{anc}} + \frac{1}{Q_{air}} + \frac{1}{Q_{ohm}} + \frac{1}{Q_{interface}} + \frac{1}{Q_{other}} \quad (4-1)$$

From this equation it is clear that if the quality factor associated with any of the individual sources of loss is small relative to others, then Q_{tot} would be dominated by that mechanism (i.e. the largest energy loss). At room temperature and at frequencies below 200 MHz (highest frequency studied in this paper), in silicon resonators, Q_{p-p} is above 125000 [41]. Air damping could also be avoided through the operation of resonator in partial vacuum. Ohmic loss could potentially be a major component of energy loss when the motional resistance of the resonator is comparable to the equivalent electrical resistance of the conductive signal path. However, this is not the case in this work as the resonators are not optimized for low motional resistance.

On the other hand, anchor loss [42] [29] and interface loss [43] [44] are the main sources of loss in piezoelectric-on-silicon MEMS resonators. Specifically, anchor loss is believed to be a significant source of energy loss at the high end of very high frequency (VHF) band. As the dimensions of the suspension tethers become comparable to the acoustic wavelength, considerable amount of stress could be applied to tether-resonator boundary in each cycle of vibration. This creates a stress wave which would propagate through the substrate transferring a portion of the acoustic energy from the resonating body to the substrate. Because the substrate is relatively large, the energy escaped

through the tethers would be mostly scattered and damped in the substrate. Therefore, anchor loss is believed to be a significant source of loss in contour-mode resonators.

A common approach to avoid excessive anchor loss is by placing the anchors at nodal points of the targeted resonance mode (i.e. regions with near-zero displacement on the acoustic cavity). Due to the near-zero displacement of these points, a minimal force would be exerted to the tether interface and anchor loss would be minimized [45] [46] [47]. The resonator/tether geometry and size could also be optimized to reduce the amount of acoustic energy lost through the tethers [42] [48] however such techniques are not effective when the tether is not located on the nodal points of the resonance mode shape. Alternatively, one could redesign the resonant cavity so that some of the acoustic energy escaping through the tethers is reflected back. This technique has been accomplished either by designing a phononic crystal structure close to (or on) the tethers [49] [50] or by utilizing structures which function as a classical acoustic reflector [29] [51] [52].

It is noteworthy that side-supported wine-glass-mode piezoelectric-based disc resonators have recently been studied in [53] [54]. For these resonators, the resonator structure is supported from four minimum displacement points around the resonator and the anchor loss is managed by tether design optimization. However, with the exception of our recent publication [23] [55], thin-film piezoelectric radial-mode disc resonators have not been studied as a center-supported design was believed to be the only reasonable design for such modes and the application of a center-supported structure was deemed complicated. This work provides both theoretical and experimental evidence for viability

of side-support radial-mode resonator on crystalline silicon and their performance superiority as the measured $f.Q$ figure of merit for the proposed side-supported radial-mode disc resonators is about four times higher than the side-supported wine-glass counterparts in [53] and about forty times higher than those in [54] a testament to the effectiveness of our approach in minimizing anchor loss.

In this dissertation, it is shown that silicon anisotropy could be exploited to minimize anchor loss for side-supported radial-mode thin-film piezoelectric-on-silicon (TPoS) disc resonators at VHF band. TPoS resonators have shown to offer some of the best $f.Q$ values amongst high frequency MEMS resonators reported in the past [56][20] and contour-mode disc resonators are amongst the most attractive designs in the literature [57] [58]. One of the reasons for the popularity of this specific design is the symmetry of the resonant cavity which results in the center of the disc to be a node for all resonance modes, hence high Q could be achieved by suspending the device from the center [57]. On the other hand, side-supported radial-mode disc resonators will have limited Q if not designed properly.

4.1 Analysis of The Radial Mode in SCS

The resonators studied in this work are designed to operate in radial (breathing) resonance mode [53]. One of the most effective approaches to minimize anchor loss for this mode is to suspend the resonant body from the center of the disc where the displacement is virtually zero. However, from the fabrication point of view, center-supported designs are generally not convenient to implement and specifically

troublesome to manufacture in TPoS structures as multiple isolated metal paths have to be routed to the suspended structure through the support stem. Thin-film piezoelectric resonators are commonly supported from the outer edge of the resonator body which is not conventionally considered an option with radial disc resonators.

For isotropic materials such as sputtered AlN, polycrystalline diamond and polycrystalline silicon, the in-plane acoustic velocity is not direction dependent and consequently the displacement is uniform at the edge of the resonator body for a radial mode disc resonator, regardless of the harmonic number (as shown in Figure 15). Therefore, there is no nodal point at the edge of the disc resonator and the only way to support the structure without substantially limiting the Q is to support it from the center.

A similar modal analysis reveals that contrary to the case for isotropic materials, for single crystalline silicon a non-uniform displacement field in the radial-mode disc resonators is established (Figure 16). Single crystalline silicon has a cubic symmetry and its effective Young's modulus is orientation dependent and could vary up to 45% for different crystalline planes [59]. Main crystalline planes of single crystalline silicon are [100], [110] and [111] and sound velocity in [110] direction is higher than sound velocity in [100] direction (7460 m/s in [100] and 8540 m/s in [110]).

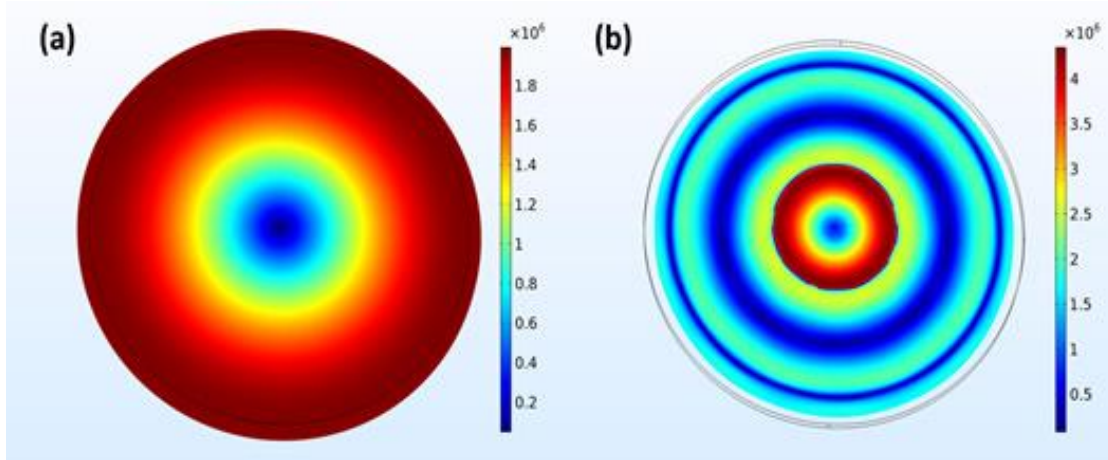


Figure 15. The simulated total displacement for first- (a) and fourth- (b) harmonic radial resonance mode of a disc structure made from material with isotropic acoustic velocity. No nodal points on the edge of the disc.

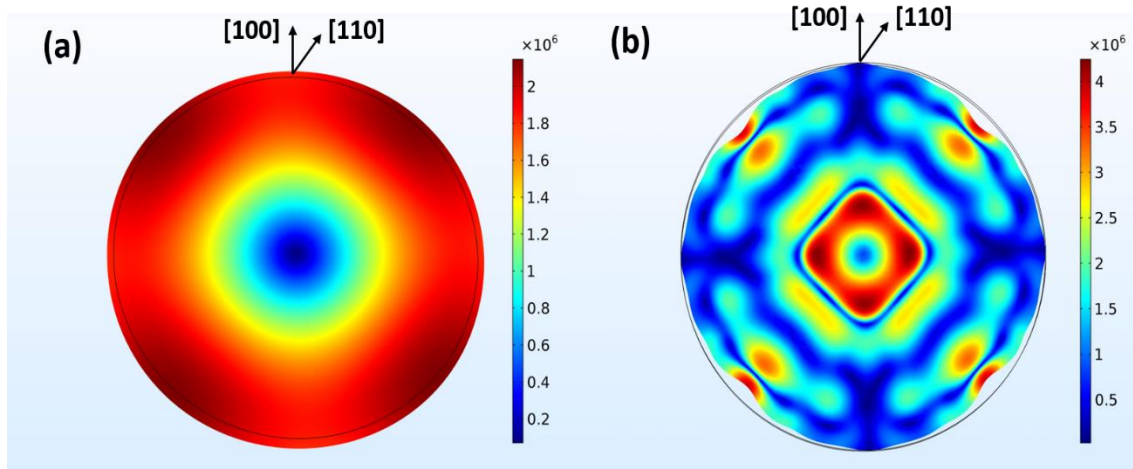


Figure 16. The simulated total displacement for first- (a) and fourth- (b) harmonic radial resonance modes of a disc structure made on a [100] single crystalline silicon substrate. Pseudo-nodal points appear on the edges for higher harmonics (e.g. fourth-harmonic)

As seen in Figure 16, the total displacement at the disc edge is much larger in [110] direction compared to the [100] direction. This non-uniformity is more prominent for high order harmonic resonance modes, rendering pseudo-nodal points to appear on the edges (e.g. fourth-harmonic in Figure 16.b). We will exploit such nodal points to support the

structure from the edges while preserving the Q . Results of modal analysis for fourth-harmonic disc resonators with suspension tethers aligned to $[100]$ and $[110]$ crystalline planes are shown in Figure 17. As expected tethers would distort the mode shape for the radial-mode disc resonator on a $[100]$ silicon wafer if the tethers are aligned to $[110]$ crystalline plane. For the same resonator rotated by 45° , tethers would be aligned to $[100]$ crystalline orientation and the mode shape would not be distorted due to the minimal displacement of the tether-resonator interface boundary.

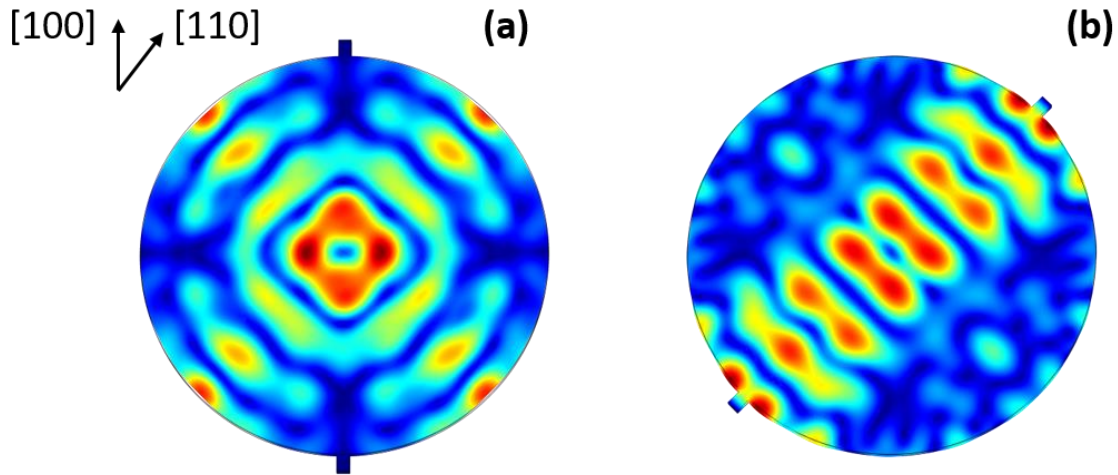


Figure 17. The simulated total displacement for fourth-order radial-mode SCS disc resonator with tethers aligned to $[100]$ crystalline plane (a) and with tethers aligned to $[110]$ crystalline plane (b) with fixed boundary condition at the outer edges of the tethers.

4.2 Finite Element Modeling

4.2.1 Anchor Loss Modeling

MEMS resonators are often much smaller than the frame to which they are connected and as a result, the frame/substrate could be assumed a semi-infinite media. Although, tethers are often at the nodal points, nevertheless there is some periodic displacement at

the resonator-tether boundary, which would transfer a portion of the acoustic energy to the substrate. It is safe to assume that the majority of the transferred acoustic wave would be scattered and dissipated rather than reflecting back to the resonant body.

There are few cases for which analytical studies exist on the energy loss of resonant systems through tethers. One such case is the bending-mode clamped-free and clamped-clamped beam resonators [60] [61] [62]. These studies are mostly limited to anchor loss in beam resonators and there are some simplifying assumptions made in all of them that further limits their application. Therefore, the usage of finite element analysis in designing resonators with optimized anchor loss becomes a necessity. The high order absorption boundary condition (ABC) and the perfectly matched layer (PML) are the most common approaches to model anchor loss [63]. PML modeling was first used for the electromagnetic wave propagation [64] and then generalized to all wave propagation with linear wave equations [63] and since has been used for modeling anchor loss for a variety of structures including disc resonators [65]. PML in finite element analysis is a layer of artificial material with finite length that is placed on the boundaries of the substrate to which the resonant structure is connected. This layer is matched with the substrate so that there is no reflected acoustic wave from the interface boundary. There are two approaches for implementing PML; modifying material properties and coordinate stretching [66]. With complex coordinate change the artificial layer is perfectly matched for all incident waves in all angles while for the material properties modification approach, the artificial layer is only matched for waves with 90° incident angle.

In this study we used PML definition in COMSOL to simulate anchor loss for which

the complex coordinate change is implemented internally. For the model to work properly, the PML region should be large enough to attenuate all the acoustic wave propagating through this medium [67]. It is also essential to choose proper PML parameters including PML scaling factor (α), substrate dimension, PML dimension and mesh size to guarantee an accurate estimation for anchor quality factor [67] [68] [69]. PML scaling factor is used by COMSOL to produce an effective scaled width for PML for waves with incident angles other than 90° to compensate for longer wavelength seen by PML in complex coordinate stretching method.

In 3D modeling of a PML, for smooth dissipation of acoustic wave and to avoid reflection from PML, dissipation over a single mesh element should be limited [67]:

$$\alpha kh < \frac{1}{5} \quad (4-2)$$

Where α is the PML scaling factor, k is the wavenumber and h is the element size. Choosing a large PML and small scaling factor or choosing a small PML and large scaling factor are two different ways to satisfy the requirement mentioned above. In [67] it was suggested to choose PML and substrate dimensions as a function of k :

$$kW_s > \frac{1}{20} \sim \frac{1}{10} \quad (4-3)$$

$$kW_{pml} > \frac{1}{10} \sim \frac{1}{5} \quad (4-4)$$

Where W_s is the substrate radius and W_{pml} is the PML radius. It is essential to model a big portion of the substrate in the low frequency resonance modes to have an accurate model since the wavelength (λ) is large for low frequencies. On the other hand, for high

frequency resonances, modeling a small portion of the substrate would suffice.

In order to verify the validity of our PML model, anchor loss was first simulated for in-plane bending mode of a clamped-free beam resonator and the results are compared with the analytical predictions. The quality factor for a bending mode cantilever beam could be estimated from (4-5) assuming that anchor loss is the dominant source of loss [61]:

$$Q = A \frac{L}{T} \left(\frac{L}{V} \right)^4 \quad (4-5)$$

where L , V and T are the beam length, width and thickness respectively and A is a constant which changes with Poison ratio (e.g. $A=3.175$ for $\nu=0.33$, $A=3.23$ for $\nu=0.3$, and $A=3.45$ for $\nu=0.25$).

In COMSOL, quality factor could be calculated from the complex eigenfrequencies resulted from running a modal analysis that contains a source of loss [70] [71]:

$$Q = \frac{Re(f)}{2 Im(f)} \quad (4-6)$$

Table 1. Anchor quality factor for bending mode beam resonator

Dimensions			Analytical anchor Q	Simulated anchor Q
L (μm)	V (μm)	T (μm)		
25	2.5	0.5	1.61×10^6	1.59×10^6
25	1.25	0.5	25.84×10^6	25.24×10^6
25	2.5	0.25	3.23×10^6	3.03×10^6
50	2.5	0.5	51.68×10^6	50.44×10^6

where $Re(f)$ is the real part of the complex eigenfrequency and the $Im(f)$ is its imaginary part.

The meshed structure and the stress field for the fundamental in-plane bending mode of a cantilever beam resonator are shown in Figure 18. The simulated quality factor is found to be dependent on the PML and substrate dimensions and PML scaling factor. From (4-3) and (4-4) we chose $W_s = \frac{\lambda}{10}$ and $W_{pml} = \frac{\lambda}{5}$ and then tuned PML scaling factor to achieve the minimum Q. The dependency of Q on the PML scaling factor is presented in Figure 20 and the lowest simulated value of Q is assumed to be the most accurate. The simulation and analytical results for several beam dimensions are compared in Table 1 and are in good agreement.

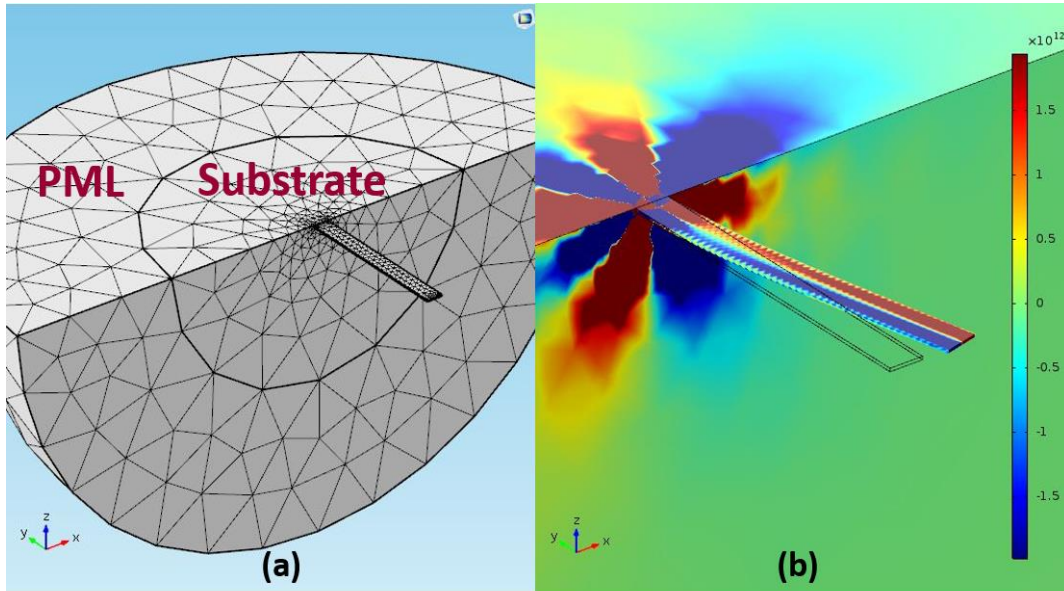


Figure 18. The meshed resonant structure (a) and the stress field for the fundamental in-plane bending mode of a cantilever (b) modeled in COMSOL. The complex eigenfrequency is utilized to calculate the Q.

Next, the same PML model and procedure is used for the radial-mode TPoS disc

resonator. The substrate and the PML radiuses are set to be equal to λ and 2λ respectively. For each harmonic mode, the substrate and the PML radiuses are adjusted to the new wavelength and the PML scaling factor is tuned for minimum Q .

In order to decrease computational load, a one-way symmetry is used for TPoS disc resonators and only half of the resonator is modeled. Meshing and stress field for radial mode disc resonators are shown in Figure 20. The simulated and fabricated TPOS disc resonator dimensions are summarized in Table 2.

Table 2. Simulated and fabricated resonator dimensions.

	Radius (μm)	AlN thickness (μm)	Substrate thickness (μm)	Moly thickness (μm)
silicon resonator	160	0.5	8	0.2
UNCD resonator	160	0.5	3	0.2

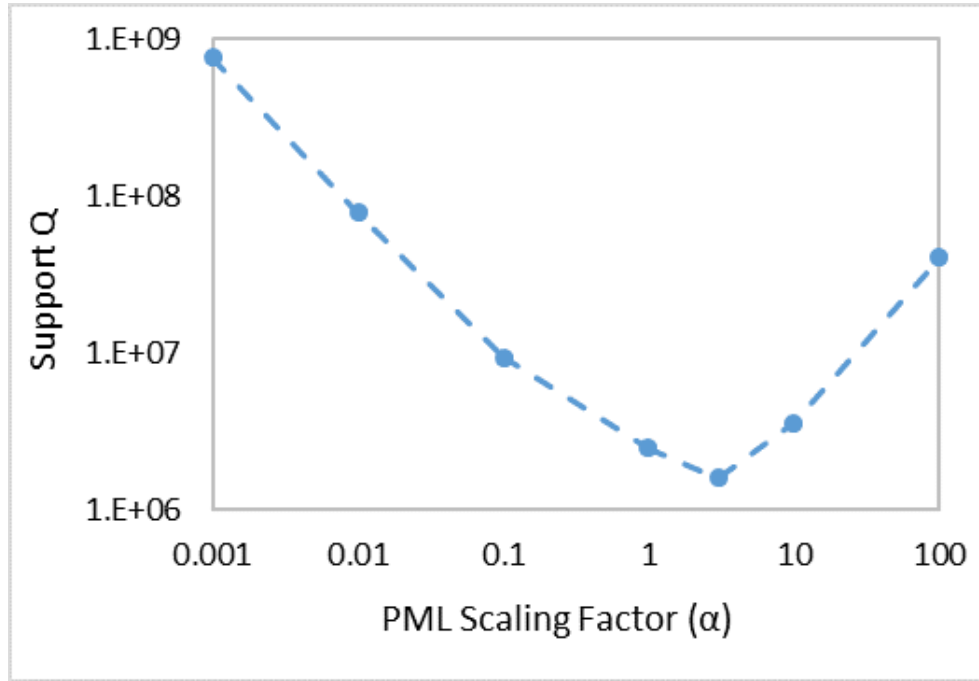


Figure 19. The anchor Q as a function of PML scaling factor for a cantilever beam resonator (similar to Figure 18). The minimum Q is assumed to be the most accurate.

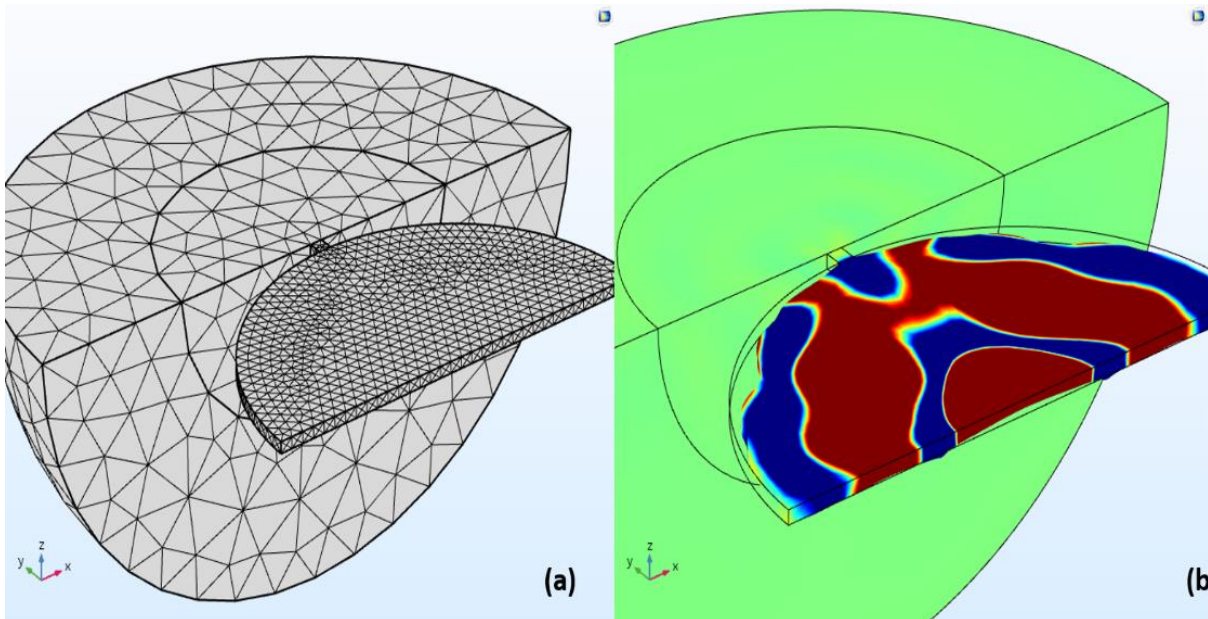


Figure 20. The meshed resonant structure (a) and the stress field (b) for a radial-mode TPoS disc resonator modeled in COMSOL. The PML and the substrate radiuses are adjusted to λ and 2λ for each harmonic mode.

Table 3. Simulated anchor quality factor for radial mode disc resonators.

Harmonic #	Single Crystalline Silicon				UNC Diamond	
	Tethers aligned to [100]		Tethers aligned to [110]			
	f_0 (MHz)	Q (k)	f_0 (MHz)	Q (k)	f_0 (MHz)	Q (k)
Second	43.42	0.46	43.56	0.63	83.38	0.75
Third	68.93	3.30	69.44	0.88	133.08	0.86
Forth	94.77	6.60	95.35	0.62	-	-
Fifth	120.48	33.26	-	-	-	-
Eighth	196.33	793.27	-	-	-	-

The simulation is also performed for resonators made of two different materials: ultra-nano-crystalline diamond (isotropic) and SCS (anisotropic) with suspension tethers aligned to [100] and [110] crystalline planes. The simulated anchor Q are compiled in Table 3.

The stress field for different harmonic order of the radial mode is plotted using Eigen frequency analysis in Comsol. The stress field in X and Y directions are added to plot the total stress field in the disc shown in Figure 21 for different harmonic mode. We ran a loss less simulation to have different mode shapes. For the data reported in Table III we added the tethers, large substrate and PML. For that simulation, due to the presence of PML anchor loss was considered in the model and because of that the Eigen frequencies here and the ones reported in Table III are a slightly different.

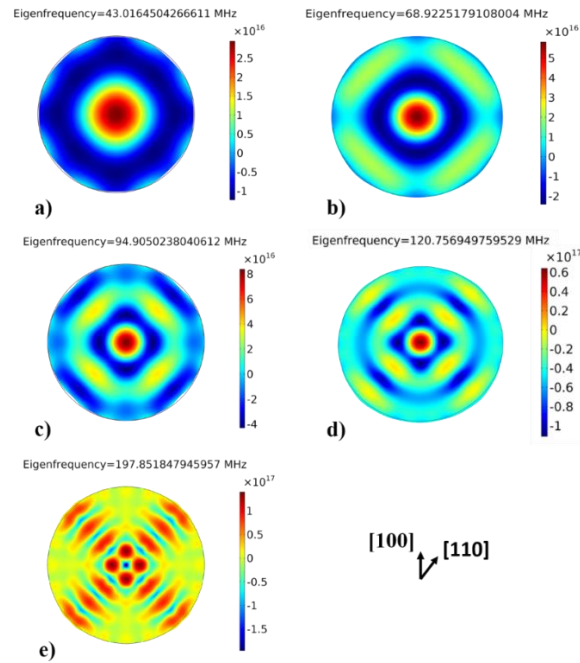


Figure 21. The stress field for 2nd (a), 3rd (b), 4th (c), 5th (d) and 8th (e) order radial mode disc resonator.

As expected, for TPoS resonators made of ultra-nano-crystalline diamond (UNCD) and also for resonators made of single crystalline silicon with tethers aligned to the [110] plane, anchor loss is significant regardless of the harmonic number. On the other hand, for the silicon devices with tethers aligned to [100] plane, Q_{anc} is predicted to improve for higher order harmonic modes by orders of magnitude.

Diamond resonators are also studied to support the hypothesis that the sharp increase in the quality factor of the high-order mode silicon disc resonators when the tethers are rotated and aligned to [100] crystalline plane could be linked to the existence of the pseudo-nodal points and not some unknown factor. As shown by simulation the same increase is not predicted in isotropic material (such as nonocrystalline diamond).

By supporting the resonant structure from its pseudo-nodal point the anchor loss could be reduced more effectively than most other support loss reduction methods. In order to confirm that, support loss is modeled for forth order radial mode TPoS resonator with different tether length. Using the tether length as a parameter for optimization of support loss will not result in a significant improvement of the support Q if the tethers are aligned to [110] (Table 4).

4.2.2 TCF Modeling

To predict the frequency drift versus temperature for radial mode SCS disc resonators, eigenfrequency analysis is utilized in COMSOL. Frequency drift versus temperature curves are generated for radial-mode disc resonators and also for [100] and [110] extensional mode resonators, all fabricated on the same single crystalline silicon device

layers.

Table 4. Simulated support Q for tether with variable length

	Tether				Tether			
	aligned to				aligned to			
	[100]				[110]			
Tether length	11 μ m	2 λ /8	3 λ /8	4 λ /8	11 μ m	2 λ /8	3 λ /8	4 λ /8
4 th								
Harmonic	6.6	1.9	5.9	3.2	0.6	0.8	1.6	0.7
Q (k)								

In order to develop the curves silicon stiffness coefficients and their corresponding temperature coefficients for Phosphorous-doped single crystalline silicon ($n=6 \times 10^{19} \text{ cm}^{-3}$) are borrowed from [16] (Table 5) ($TC^{(1)}$ is the first order temperature coefficient of elastic constant and $TC^{(2)}$ is the second order temperature coefficient of elastic constant). The stiffness matrix is then calculated for each temperature and is used to repeat the modal analysis and calculate the shifted resonance frequency.

As shown in Figure 22, the turn-over temperature for the radial-mode disc resonator is predicted to be between the turn-over temperature of lateral extensional resonators aligned to [100] and [110] crystalline planes [31]. In radial-mode disc resonators, there are significant stress field components in both [100] and [110] crystalline

planes and therefore, the predicted temperature-frequency dependency is reasonable.

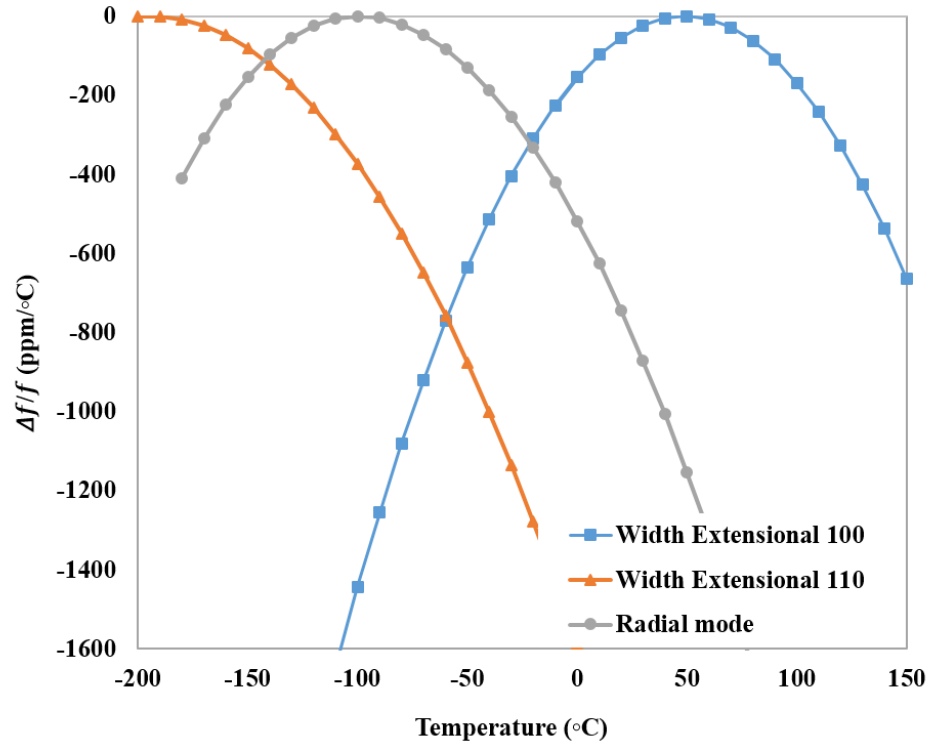


Figure 22. The simulated temperature-frequency dependency for radial mode disc resonator fabricated on n-type doped silicon ($n=6 \times 10^{19} \text{cm}^{-3}$) compared with width-extensional resonators oriented in two different directions.

Table 5. Elastic constants of phosphorus doped ($N=6 \times 10^{19} \text{cm}^{-3}$) silicon and their corresponding first and second order temperature coefficients [16]

Dopant	C_{11}	C_{12}	C_{44}	$T_{C_{11}}^{(1)}$	$T_{C_{12}}^{(1)}$	$T_{C_{44}}^{(1)}$	$T_{C_{11}}^{(2)}$	$T_{C_{12}}^{(2)}$	$T_{C_{44}}^{(2)}$
	(GPa)	(GPa)	(GPa)	(ppm/°C)	(ppm/°C)	(ppm/°C)	(ppb/°C ²)	(ppb/°C ²)	(ppb/°C ²)
Phosphorus									
6.6	164.0	66.7	78.2	-34.2	-135.2	-67.8	-103	-1	-40
$\times 10^{19} \text{cm}^{-3}$									

4.3 Fabrication Process

TPoS resonators are constituted of a piezoelectric layer deposited on a layer of low acoustic loss material sandwiched between two metal layers. Piezoelectric layer is actuated by an applied electric field between these metal electrodes. A schematic of the TPoS disc resonators of this work is shown in Figure 23. The radial-mode disc resonators of this work are fabricated both on SCS and UNCD device layers. The fabrication process of TPoS resonators on silicon is thoroughly discussed in Chapter 3.

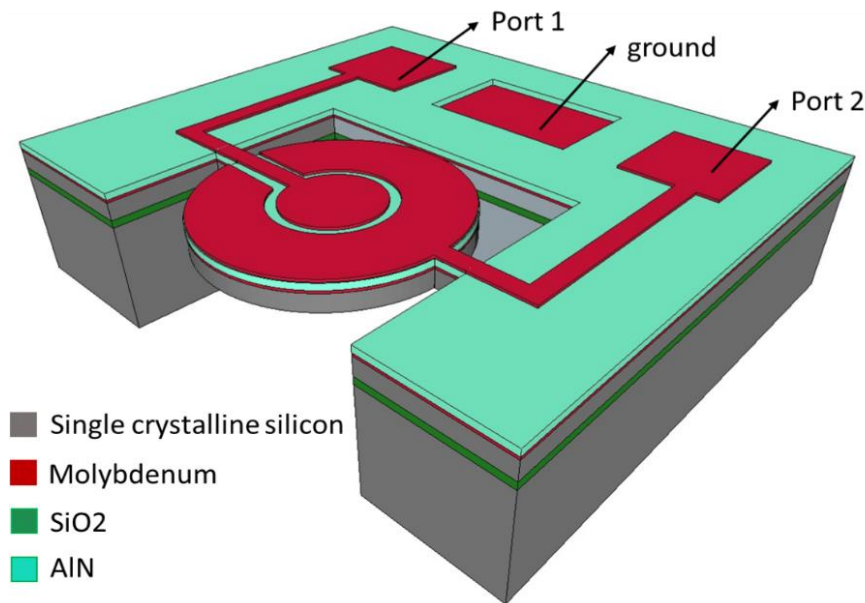


Figure 23. The schematic of a TPoS disc resonator fabricated in this study.

Disc resonators are also fabricated on ultra-nano-crystalline diamond (UNCD). A UNCD film with average grain size of less than 10 nm was deposited by hot filament chemical vapor deposition (HFCVD). To promote C-plane grain growth in the following

sputtered AlN layer, UNCD deposition is followed by two polishing steps. The rest of the process is very similar to the fabrication steps on an SOI wafer explained above. The diamond layer is etched in an inductively coupled plasma (ICP) etching chamber with O_2/CF_4 plasma. The detailed process flow for devices made on UNCD device layer could be found in [28].

4.4 Experiment Results

4.4.1 Quality Factor Measurements

Frequency response of the TPoS disc resonators are measured both in atmospheric pressure and partial vacuum (1 Torr) using a Rohde & Schwarz *ZNB 8* network analyzer and a pair of GSG probes (Cascade Microtech Inc) at ambient temperature while terminated with the internal $50\ \Omega$ impedance of the network analyzer. The loaded quality factors (Q_{loaded}) are measured and the unloaded quality factors are extracted by de-embedding the loading effect of the termination resistances.

Frequency responses are measured for disc resonators on anisotropic (single crystalline silicon) device layer with tethers aligned to [100] and [110] crystalline planes and also for the disc resonators fabricated on isotropic UNCD device layer. For the UNCD disc resonators, the radial-mode resonance frequencies are higher due to the higher Young's modulus of the UNCD [28].

As shown in TABLE VI, for the UNCD disc resonators and also the SCS disc resonator with tethers aligned to [110] direction, Q values are extremely low. This is believed to

support our hypothesis indicating that a large portion of acoustic energy would be lost through tethers considering that the structure was not supported from its pseudo-nodal points in these resonators. On the other hand, for higher harmonic radial-mode disc resonators with tethers aligned to [100] plane, unloaded quality factor improves from an average of 290 at 43 MHz to 6300 at 196 MHz for the eight-harmonic mode. Frequency responses for 5 different disc resonators are measured in atmospheric pressure in order to report the values for maximum quality factor (Q_{max}) and average quality factor (Q_{avg}) reported in Table 6.

Table 6. Measured quality factor data for radial mode disc resonators.

Harmonic	single crystalline silicon								UNC Diamond			
	Tethers aligned to [100]				Tethers aligned to [110]							
	f_0	Q_{max}	R_m	Q_{avg}	f_0	Q_{max}	R_m	Q_{avg}	f_0	Q_{max}	R_m	Q_{avg}
#	(MHz)	(k)	(k Ω)	(k)	(MHz)	(k)	(k Ω)	(k)	(MHz)	(k)	(k Ω)	(k)
Second	42.8	0.4	6.0	0.3	43.3	0.5	20.3	0.5	80.0	0.9	6.1	0.7
Third	69.0	2.8	0.3	1.8	70.2	0.65	7.7	0.47	128.1	0.2	9.4	0.17
Forth	94.7	5.6	1.0	3.8	95.9	0.8	33.1	0.65	-	-	-	-
Fifth	120.3	7.4	1.0	4.3	-	-	-	-	-	-	-	-
Eighth	195.8	9.7	1.2	6.3	-	-	-	-	-	-	-	-

The frequency response for a UNCD radial-mode disc resonator is shown in Figure 24. The frequency response for a SCS radial-mode TPoS disc resonators with tethers aligned to [100] crystalline plane measured in partial vacuum is shown in Figure 25. The frequency span for this measurement is 40-200MHz and the second, third, fourth, fifth and eighth radial modes are detected for SCS device (inset figures on the frequency plot of Figure 25). The anchor quality factor is modeled for all the resonance modes within a region around the measured resonance frequencies for each harmonic mode. For the mode shapes which has a reasonable quality factor the TCF curves are modeled and compared to the measured TCF curve to confirm that the measured resonance peaks are assuredly higher order harmonic radial modes.

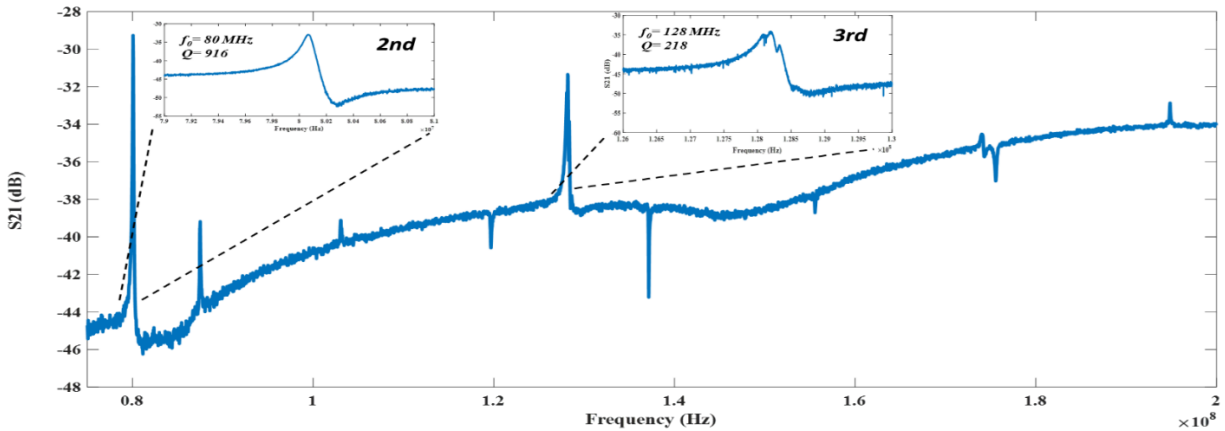


Figure 24. The recorded S21 for a UNCD radial-mode TPoS disc resonator simultaneously presenting the resonance peaks of 2nd, 3rd harmonics with their corresponding Q.

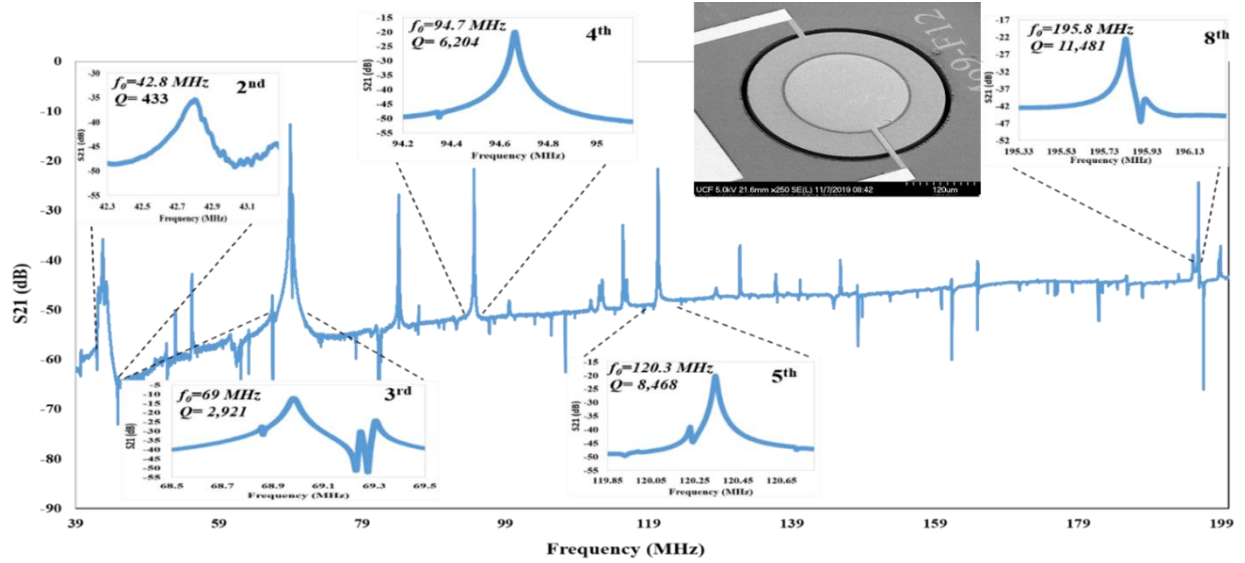


Figure 25. The recorded S21 for a SCS radial-mode TPoS disc resonator with tethers aligned to [100] direction measured in partial vacuum simultaneously presenting the resonance peaks of 2nd, 3rd, 4th, 5th and 8th harmonics with their corresponding Q.

For the single crystalline silicon resonators with tethers aligned to [100] plane, the simulated and measured quality factor are matched fairly well. This confirms our hypothesis that the support loss is the dominant source of loss for the side supported radial mode TPoS resonators when the structure is not supported from its pseudo-nodal points. However, considering the simulated quality factor for the higher order harmonic radial mode TPoS resonators with tethers aligned to [100] plane, the support loss is almost eliminated. For these resonators, we believe other sources of loss such as interface loss, surface loss, etc. are playing a more important role.

It is necessary to mention that the top electrode pattern is not designed for the optimum coupling factor. A portion of electrical charge accumulated under the electrodes might be canceled with the charge with different polarities for higher order radial mode resonators. Only two electrodes are designed for radial mode TPoS resonator so all the

harmonic modes could be excited on the same resonator and the quality factor could be fairly compared for different harmonic radial mode TPoS resonators.

The unloaded quality factors measured both at atmospheric pressure and partial vacuum for different harmonics of the radial-mode TPoS disc resonator exhibiting the highest Q are compared in Table 7. For lower harmonic modes it appears that the quality factors do not change significantly under vacuum which further confirms that the anchor loss is the dominant source of loss for the second and third harmonics. For the high order modes on the other hand, the anchor loss is no longer the main source of loss and the quality factor improves about 19 % in vacuum in the absence of air damping loss for eighth harmonic mode (increased from 9,660 to 11,480).

The 8th harmonic radial mode TPoS resonator quality factor is compared to some resonators in the same range of frequencies which are already studied in the literature (Table 8). As seen here, quality factor of the TPoS disc resonator (this work) is the second best only after the capacitive resonators while the $kt^2.Q$ in this device surpasses that of the capacitive resonator by a large margin. Also, it is notable that for a capacitive resonator, the quality factor improves significantly when measured in the vacuum. This is because squeezed-film air damping is one of the main sources of loss in the capacitive resonators due to the extremely small size of the capacitive gaps that are necessary for improving the coupling factor [17]. This sensitivity to air damping will put stringent requirement on the packaging of such resonators that could be relaxed for TPoS resonators.

Table 7. Measured data for single crystalline silicon disc resonator with tethers aligned to [100] direction.

Harmonic #	In Atmospheric pressure			In partial Vacuum (1 Torr)		
	f_0	Q	R_m	f_0	Q	R_m
	(MHz)	(k)	(k Ω)	(MHz)	(k)	(k Ω)
Second	42.78	0.43	6.04	42.78	0.45	5.79
Third	68.98	2.80	0.31	68.98	2.92	0.29
Forth	94.66	5.60	1.01	94.66	6.20	0.90
Fifth	120.34	7.44	0.98	120.34	8.47	0.91
Eighth	195.82	9.66	1.22	195.82	11.48	1.20

Table 8. Comparison of the best results reported in this work with selected published data in the same frequency range.

Resonator	f_0	Q_{air}	Q_{vac}	Resonance	Reference
Type	(MHz)	(K)	(K)	mode	
TPOS	195.82	9.66	11.48	Radial	This work
TPOS	142	6.8	-	Lateral extensional	[72]
Capacitive	193	8.8	23	Radial	[58]
Piezoelectric	229.9	-	4.3	Lateral extensional	[25]

4.4.2 TCF Measurements

Temperature coefficient of frequency is measured for a radial-mode TPoS resonator and lateral-extensional mode TPoS resonators aligned to [100] and [110] planes. The center frequency drift is measured in the range of -60 °C to 80 °C in a Janis cryogenic vacuum probe station in which liquid nitrogen is used to cool down the chuck below ambient temperatures. The results are plotted in Figure 26. All three devices used for this measurement are made on the same substrate with a doping concentration of $n \sim 4 \times 10^{19} \text{ cm}^{-3}$. As predicted by the simulation results of section III.B the turn-over temperature for the radial-mode disc is between the two turn-over temperatures for the extensional mode resonators aligned to [100] and [110].

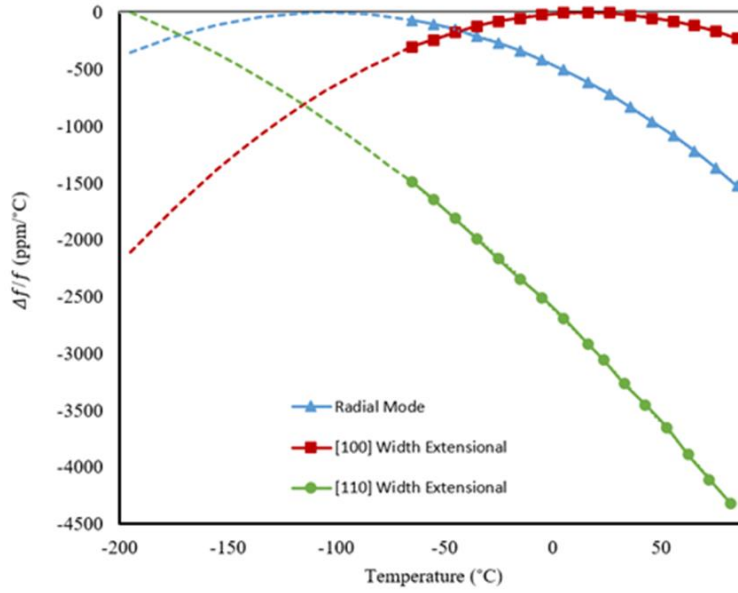


Figure 26. The frequency-temperature plot measured for a radial-mode TPoS disc resonator and extensional mode TPoS resonators aligned to [100] and [110] silicon planes.

However, the turn-over temperature for all three resonator types are at lower temperatures than predicted in Figure 22. This is mainly because the available stiffness coefficients used for the simulation section are reported for a doping concentration higher than what was used for fabrication in this work and also only the silicon layer was considered in the simulation and the contribution of AlN and Molybdenum layers were neglected in the simulation. For the radial-mode disc resonator, the extrapolated turn-over temperature is at ~ -105 °C, when it's at ~ 16 °C for the [100] extensional mode resonator and below -200 °C for the [110] extensional mode resonator.

4.5 Harmonic Radial Mode Disc TPoS Resonators

The disc resonators are fabricated with only two electrodes as shown in Figure 23 to fairly compare the quality factor of different harmonic on the same device. However,

this electrode design is not efficient for charge collection and the coupling efficiency and motional resistance of the higher harmonics are negatively affected.

The electrode design should be optimized for each harmonic radial mode. The optimized electrode design for a fourth harmonic radial mode TPoS resonator is shown in Figure 27.

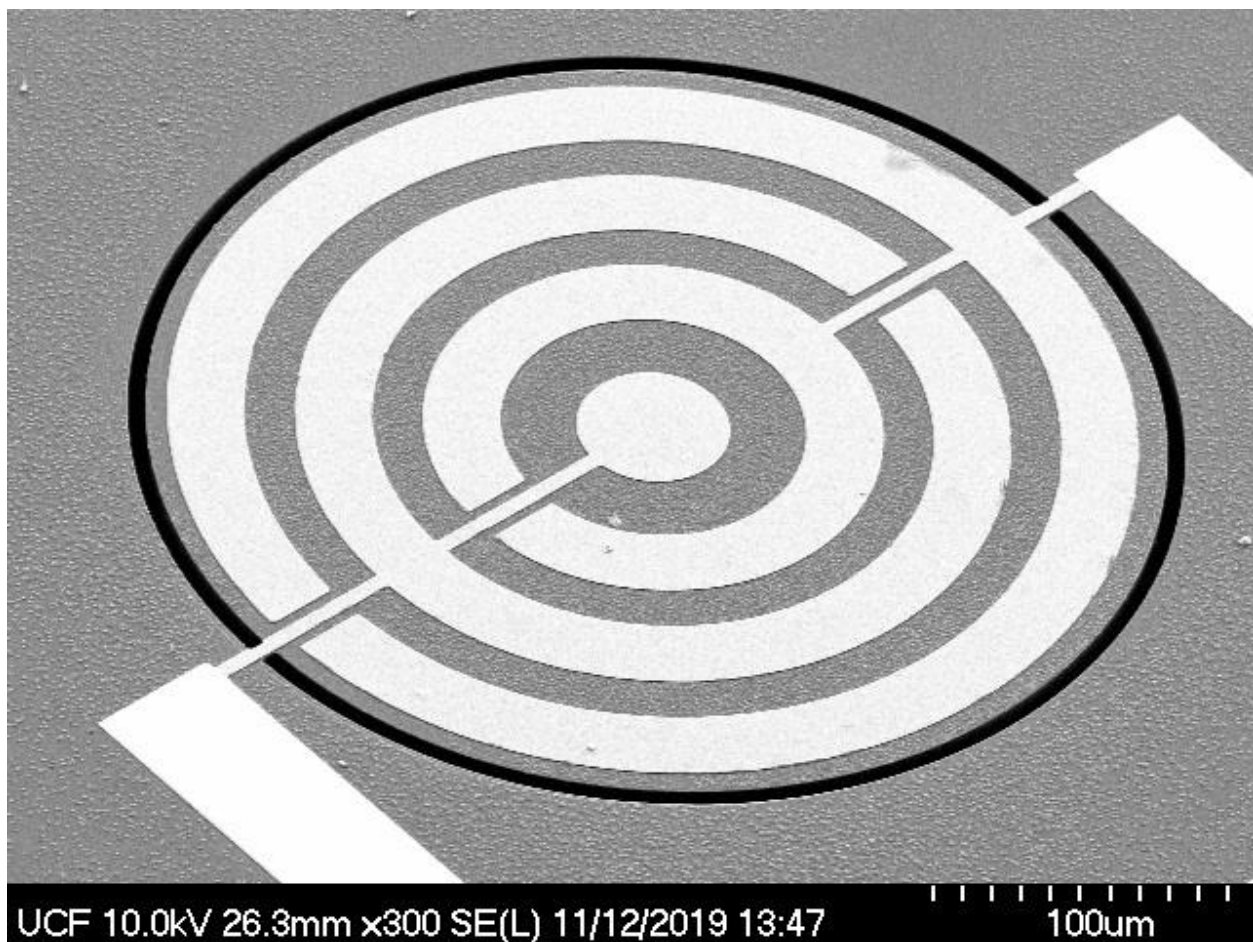


Figure 27. The SEM photo for the 4th harmonic radial mode TPoS disc resonator.

These resonators are fabricated on a 25 μm silicon topped with 1 μm 20% Scandium doped AlN with the same disc diameter as the radial mode disc resonators presented in

the previous sections of this chapter. The measured frequency response for this fourth order radial mode TPoS resonator is plotted in Figure 28. The measured motional resistance is improved from 1 k Ω for the two electrode design to about 0.2 k Ω with the optimized electrode design.

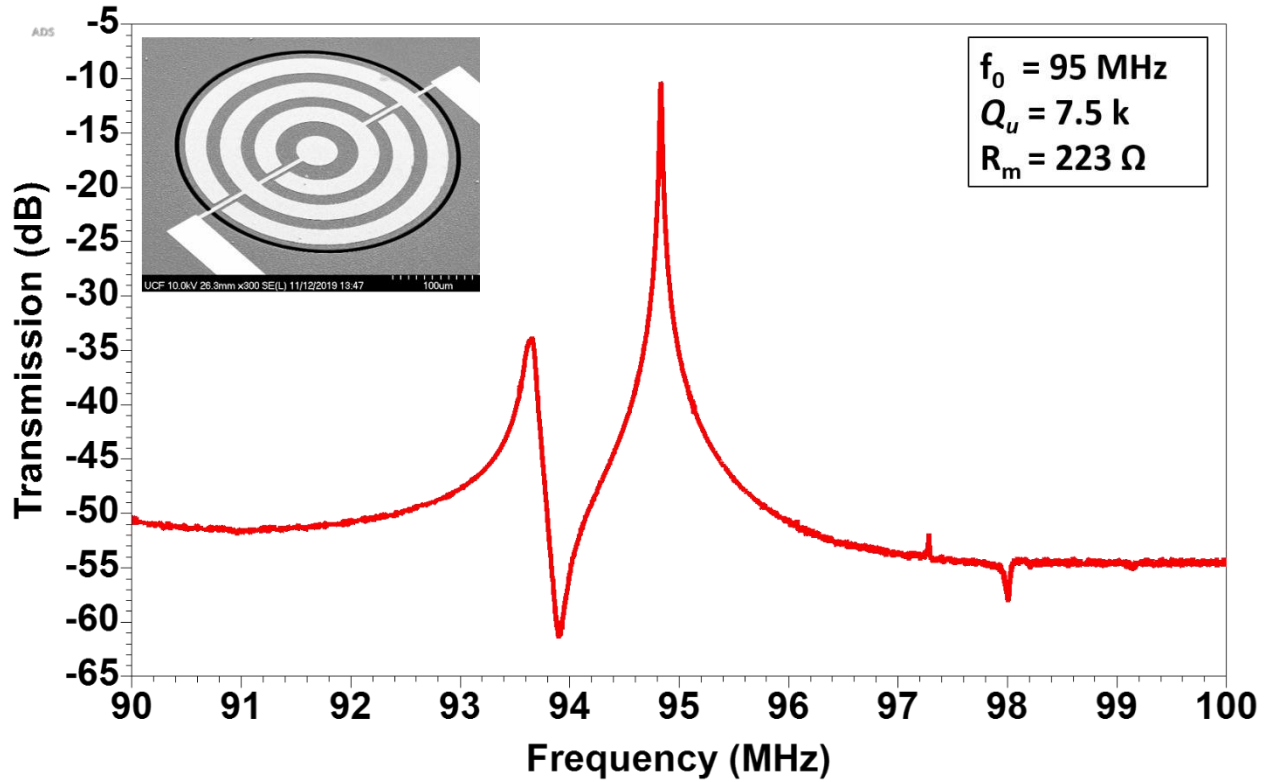


Figure 28. The measured frequency response for a 4th harmonic radial mode disc TPoS resonator. Lower motional resistance is measured compared to design with just two electrodes.

4.6 Conclusions

Radial-mode disk resonators are commonly supported from the center of the disk due to the expected excessive anchor loss for side-supported radial modes. Therefore, piezoelectric radial-mode disk resonators are seldom developed. In this work, it was

demonstrated that in a TPoS radial-mode disk resonator by rotating the anchors to align with [100] plane, anchor loss would be reduced significantly. Specifically, anchor loss would no longer be the dominant source of loss for high-order harmonic modes. Devices are fabricated on SCS and UNCD and the validity of this claim is confirmed both with experimental measurements and finite-element simulations. Due to their reported high-quality factor, high-order radial-mode TPoS disk resonators are excellent candidates for stable oscillator designs in VHF band.

CHAPTER 5: QUASI THICKNESS LAMÉ MODES IN THIN-FILM PIEZOELECTRIC- ON-SILICON RESONATORS

Micro electromechanical resonators are at the heart of integrated low-noise oscillators, filters and sensors [73] [74] [33] [14].

High quality factor and large coupling efficiency combined with high thermal stability and power handling in small form factors are desired for such applications. Although MEMS resonators offer high quality factor and coupling efficiency in small size, they generally suffer from relatively high temperature coefficient of frequency (TCF). The temperature coefficient of elasticity (TCE) is around -60 ppm/°C (TCF~ -30 ppm/°C) for lightly-doped silicon based MEMS resonators [16], around -50 ppm/°C (TCF~ -25 ppm/°C) for AlN based resonators [25] and around -140 to -180 ppm/ °C (TCF~ -70 ppm/°C to -90 ppm/°C) for Lithium Niobate (LN) resonators [75]. The reported high TCF for MEMS resonators limits their usage in ultra-stable oscillator applications.

Active and passive temperature compensation methods have been studied to reduce the frequency drift. Degenerate doping of the silicon device layer [32] , or using composite structures with positive TCE materials (such as silicon dioxide) in the form of over layers [32] or pillars [76] are amongst the proposed passive temperature compensation methods. Using an over layer of oxide however, adversely impacts both the quality factor (due to energy scattering between layers) and the coupling efficiency. It also adds to the fabrication complexity. With passive temperature compensation of MEMS resonators, sub

ppm temperature stability remains out of reach, even though required for many ultra-stable clock applications.

In active temperature compensation methods on the other hand, the resonance frequency is actively tuned in real-time to compensate for the frequency drift caused by the ambient temperature variations. The most widely studied methods for active temperature compensation are tuning the termination impedance [77] [78], inducing a mechanical stress [79] and operating the resonator at a constant elevated temperature [80] (e.g. oven controlled oscillators). With active temperature methods sub ppm temperature stability could be achieved over the desired temperature range. Oven controlled quartz crystal oscillators (OCXO) have been widely studied in the literature [81]. The same method could be used for temperature compensation in MEMS resonators specially if the turn-over temperature (the temperature at which the TCF changes polarity) of the resonator is greater than the highest nominal operation range. This is because the TCF is virtually zero at turn-over temperature and therefore the oscillator stability would be only marginally affected by the temperature control circuitry. Hence, designing resonators with turn-over temperature values above the commercial range (80 °C) is critical in realizing oven-controlled oscillators.

Based on the results reported in literature [16], Lamé mode silicon resonators exhibit the highest turn-over temperature amongst conventional resonance modes for the same silicon doping concentration.

Although capacitive excitation of planar Lamé modes is frequently reported in silicon resonators at MHz regime [82], [83] but the motional impedance is usually large for these resonators. Thin-film piezoelectric-on-substrate (TPoS) platform offers a pathway to reducing the motional resistance high Q silicon-based resonator. The substrate layer which is usually single crystalline silicon concurrently improves the power handling of these resonators as well [30].

That said, planar Lamé modes, cannot be efficiently actuated in silicon through piezoelectric transduction. This is because of the fact that the sputtered piezoelectric thin-films such as AlN are isotropic in the plane of the substrate. As discussed in Figure 29, the stress field is the same but with opposite polarities in the X and Y directions for a planar Lamé mode and therefore charges cancel out for any electrode that is laid out across a piezoelectric film thickness. In the case of piezoelectric on substrate resonators, since the symmetry would be disrupted with the presence of the substrate layer (i.e. silicon) planar Lamé mode could be actuated but still the coupling efficiency would be limited (<0.0015%) which would drastically increase the motional resistance of the resonator [84].

An alternative family of Lamé resonators coined as Cross-sectional Lamé mode resonators (CLMR) have been recently demonstrated in thin-film AlN resonators [24], [85] by exciting Lamé modes in the thickness of the AlN resonator. In CLMRs both d_{31} and d_{33} piezoelectric coefficients constructively contribute in the excitation of a two-dimensional mechanical vibration (excitation of the Lamé mode in the cross section of AlN film). As a result, these resonators offer coupling factors larger than what is achievable in lateral-

extensional mode (Contour-mode) resonator. A limitation of such resonators is that the range of center frequencies that could be achieved is relatively restricted to high frequencies considering that the thickness of the sputtered piezoelectric layers cannot be practically greater than a few micrometers.

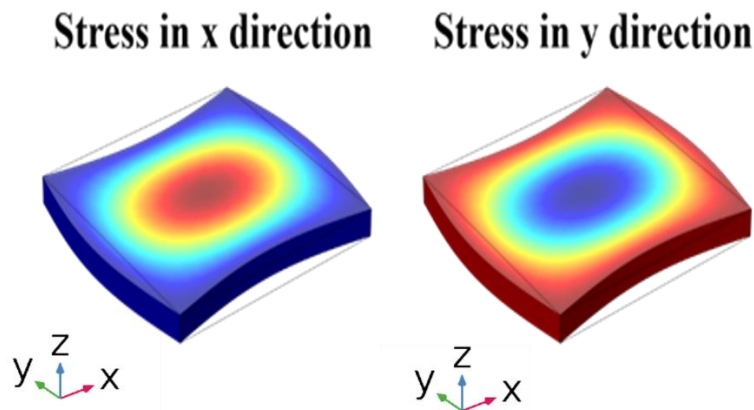


Figure 29. The simulated stress field in the x and y directions for a pure AlN planar Lamé mode. In each half vibration cycle, stress field is tensile in one planer axis and compressive in the other axis (dark blue and dark red indicate maximum opposing stress in the center). Therefore, such planar Lamé mode cannot be efficiently excited with thin polycrystalline films laid on top of the resonator body.

5.1 Thickness Lamé Mode in TPoS Resonators

Commonly, the d_{31} piezoelectric coefficient of sputtered piezoelectric films (e.g. AlN) is utilized to excite lateral-extensional (LE) modes in TPoS resonators. For the fundamental LE mode, the width of the resonator is equal to resonance half wavelength. To actuate higher harmonics, interdigitated electrode patterns are used. In such patterns the distance between two adjacent electrodes is called finger-pitch (FP) and is equal to half resonance wavelength.

As shown in Figure 30.a, lateral-extensional mode is actuated in a silicon slab when the $FP \gg$ thickness (T). As the finger pitch decreases and approaches the thickness of the resonator, mode shapes with properties between lateral-extensional mode and Lamé mode emerge in the thickness of the resonator (Figure 30.b and Figure 30.c). For the dimensions in which the lateral and vertical displacements are the same, a pure Thickness-Lamé mode would be actuated in the resonator slab (Figure 30.d).

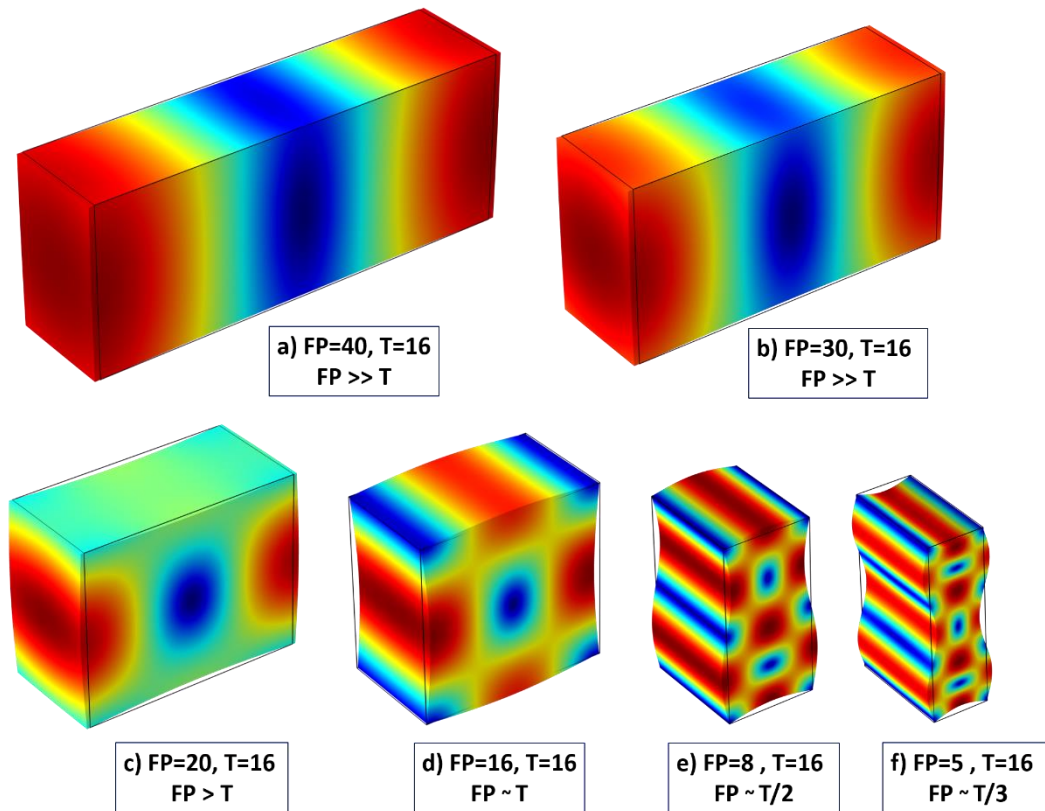


Figure 30. The displacement field for a silicon resonator with thickness (T) and different finger pitches. For the finger pitches close to the thickness of the resonator, Lamé mode (d) would replace lateral extensional mode (a) in the resonator slab. For the finger pitches close to a fraction of the thickness of the resonator, higher harmonic Lamé are actuated in the resonator slab (second harmonic (e) and third harmonic (f)).

If a thin piezoelectric film sandwiched between two metal layers is laid out on top of the silicon slab as is the case in TPoS platform, the d_{31} and d_{33} piezoelectric coefficients of the film, constructively contribute in actuating Lamé-mode in the composite structure of (Mo/AlN/Mo/Si). Caused by the presence of the piezoelectric film and metal layers, the acoustic symmetry of the medium is disrupted and therefore technically the mode is no longer a pure Lamé-mode. We refer to these mode shapes as quasi thickness-lamé modes (QTLM). For QTLM resonators if the FP is close to the thickness of the resonator, the resonator would have properties closer to the property of pure Lamé mode resonator. As the FP increases the behavior of the resonator transitions from Lamé mode and becomes similar to the property of lateral-extensional mode.

5.2 Harmonic QTLM TPoS Resonators

Harmonic QTLM Lamé modes could also be actuated in the thickness of the TPoS resonator. When the FP is chosen $\sim \frac{thickness}{n}$, the n^{th} harmonic in the thickness of the resonator is excited. For example, second and third harmonic QTLM are shown in Figure 30.e and Figure 30. f. Actuating higher order harmonics in the thickness of the resonator extends the range of frequencies that could be achieved on the same substrate with QTLM resonators.

Second and third harmonic QTLM TPoS resonators are designed on a 1 μm ScAlN/16 μm Si. For these resonators, piezoelectric polarization is modeled for QTLM using eigen frequency analysis in COMSOL. As shown in Figure 31.a, the mode shape is no longer symmetric. In order to collect the most charge possible an asymmetric electrode design

is proposed. In this design, the electrodes are shifted to align the charge center modeled in the Eigen frequency model.

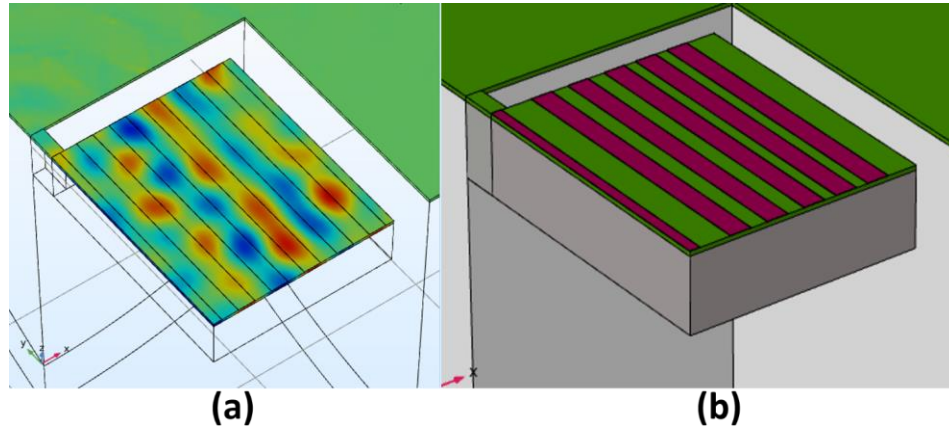


Figure 31. The piezoelectric polarization field (a) and asymmetric electrode design (b)

A schematic view graph of a third order QTLM TPoS resonator is shown in Figure 32. Based on the FP/T ratio the same structure enables actuation of lateral-extensional and thickness quasi Lamé modes.

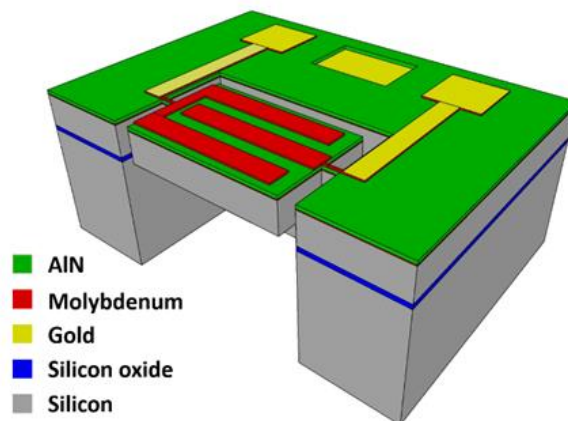


Figure 32. A schematic view graph of a third-order QLM TPoS resonator. Electrode patterns are the same as the ones for lateral extensional mode.

5.3 Quasi Thickness Lamé Mode TPoS Resonator

5.3.1 Coupling Efficiency for QTLM TPoS Resonators

For the fundamental QTLM TPoS resonator, the stress field is concentrated in the center of resonator stack (mostly in the silicon). Therefore, the stress concentration in the piezoelectric film is relatively small and the coupling efficiency is compromised. As higher order QTLM is actuated in the thickness of the resonator, the stress field in the piezoelectric region of the TPoS resonator increases (Figure 33) and the coupling efficiency is expected to improve correspondingly.

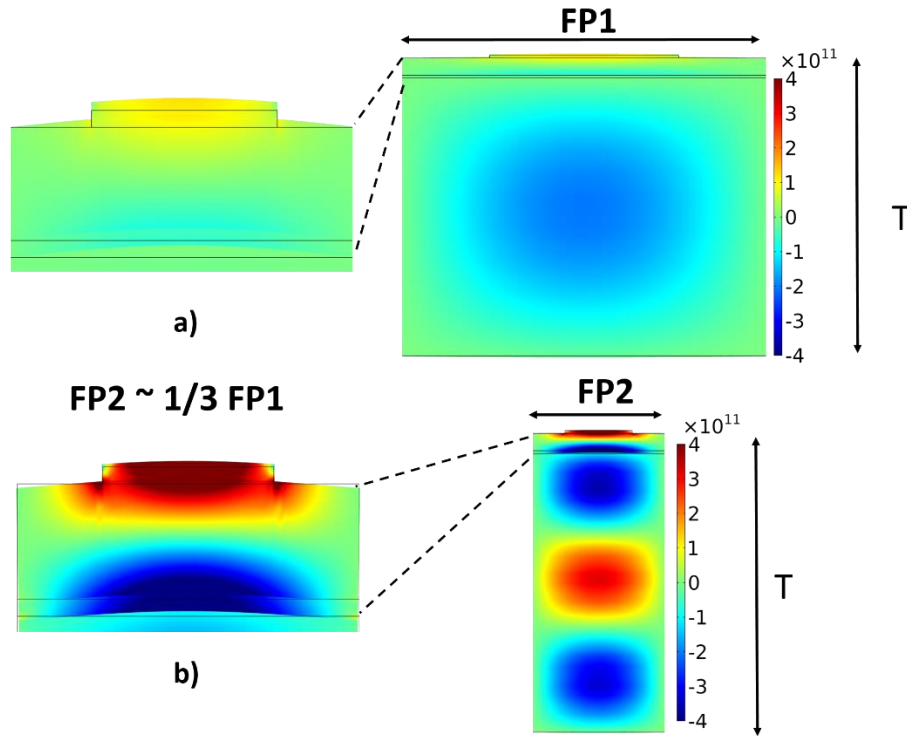


Figure 33. The stress field in the fundamental a) and third harmonic QTLM resonators. The stress field in the piezoelectric portion of the third harmonic mode is larger and because of that higher coupling efficiencies are expected for third harmonic QLM.

A 2D loss-less frequency analysis model in COMSOL is used to study the coupling efficiency of the QTLM TPoS resonators. The resonator stack includes a 16 μm silicon covered by 1 μm of 20% ScAlN sandwiched between two 100 nm Mo layers. The one port admittance is simulated using the frequency response analysis and the coupling efficiency is calculated using modeled series and parallel frequencies. The modeled admittance for the third order QLM TPoS resonator is shown in Figure 34 and the coupling coefficient for different harmonics are summarized in Table 9. The material data for 20% ScAlN is borrowed from [86].

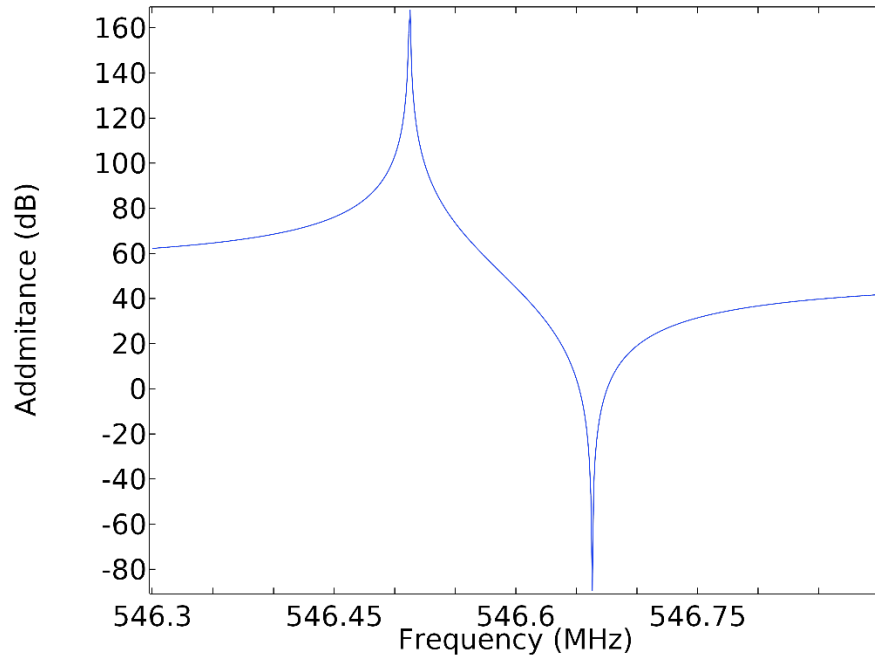


Figure 34. The modeled admittance for a third order QLM TPoS resonator. The coupling efficiencies are calculated using the series and parallel frequencies.

Table 9. The modeled coupling efficiencies for TPoS resonators. A full stack of Mo/AlN/Mo/Si is considered with the same thickness of the fabricated resonators (0.1 μm Mo/1 μm ScAlN/ 0.1 μm Mo/ 16 μm Si)

Mode shape	Silicon Thickness (μm)	20% ScAlN Thickness (μm)	Modeled K_t^2
Lateral-extensional	16	1	0.85%
1 st harmonic QTLM	16	1	0.03%
2 nd harmonic QTLM	16	1	0.08%
3 rd harmonic QTLM	16	1	0.14%
Lateral-extensional	4	2	3.8%
2 nd harmonic QTLM	4	2	7.8%

As expected the coupling efficiency increases for higher harmonic QTLM TPoS resonators but never-the-less the lateral-extensional modes will offer higher coupling (Table 9). This trend will change and the QTLM will offer a higher coupling factor than the lateral-extensional mode if the thickness of the piezoelectric film approaches half wavelength of the thickness Lamé mode. A second-harmonic QTLM excited in a 4 μm of silicon slab covered with a 2 μm of piezoelectric film (20% ScAlN) is presented in Figure 35. The simulated coupling factor is 7.8% for the second harmonic QTLM TPoS resonator.

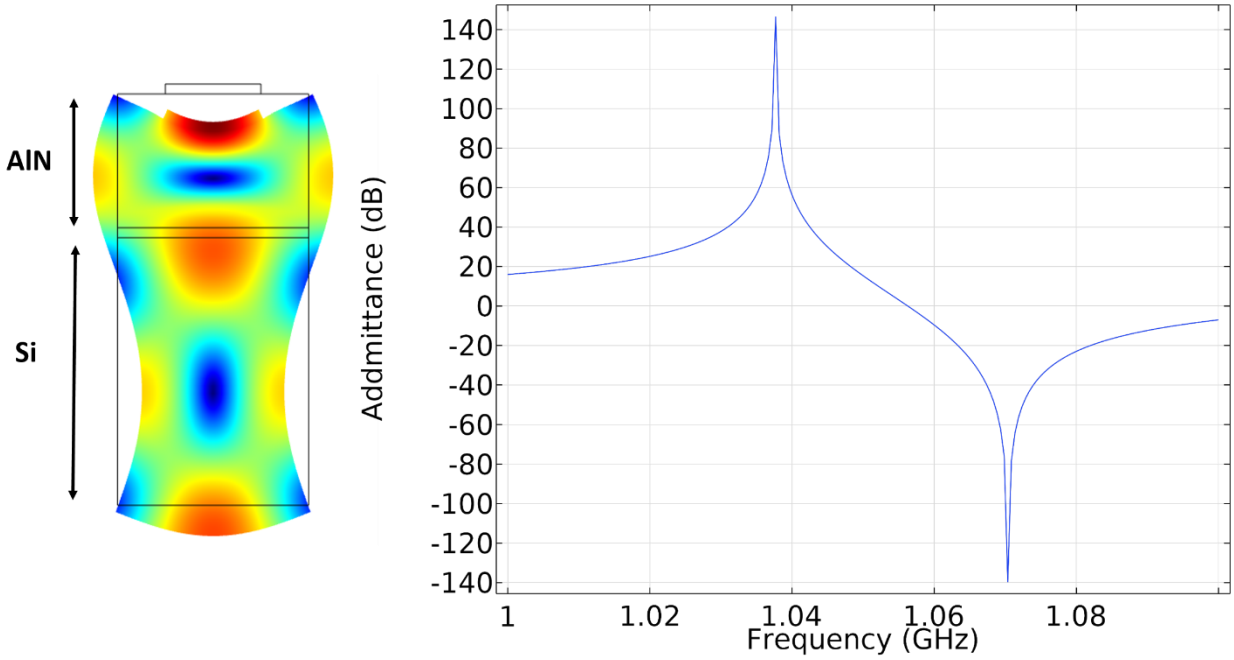


Figure 35. The admittance modeled for a fourth harmonic QTLM TPoS resonator with 4 μm silicon topped with 2 μm AlN.

5.3.2 Support Loss in QTLM TPoS Resonators

The resonator quality factor directly impacts the noise floor of the system in which the resonator is utilized. Therefore, achieving high quality factors are crucial for many applications such as oscillators and sensors. Anchor loss, ohmic loss and interface loss are the main sources of loss in piezoelectric resonators. Although improving the interface loss might be challenging, these resonators can be designed for optimum anchor loss.

Since the Lamé mode in the QTLM TPoS resonators is formed on the cross-section of the resonator, there are no pseudo-nodal points at the side of the resonator. Consequently, a substantial portion of acoustic energy could be radiated to the substrate through the tethers. By placing planar acoustic reflectors (etching trenches in the

substrate), the acoustic wave is reflected due to very large acoustic mismatch between air and silicon. If these reflectors are designed at the proper distance from the resonator tether, the reflected wave would be constructively interfering with the resonators standing wave [29], [87], [88].

In this work, we present a novel acoustic isolation frame to minimize the anchor loss for QTLM. As shown in Figure 36, the resonator is carved out of a suspended circular frame. The radiated acoustic energy through tethers is reflected from the edges of this frame. The anchor quality factor is optimized by optimizing the dimensions of the structure.

A 3D perfectly matched layer (PML) based model is developed in COMSOL to study the anchor loss for QTLM TPoS resonators. The dimension of the acoustic isolation frame is varied to search for the optimized frame dimensions. Based on the modeled data, the anchor quality factor is optimized when the acoustic isolation frame has a diameter of $(2n \times \lambda/4) + 2 \times (\text{tether-length})$. The support quality factor is improved by an order of magnitude for the optimum frame dimensions Table 10 for the fundamental QTLM TPoS resonator with $FP = 17\mu\text{m}$ at 185 MHz.

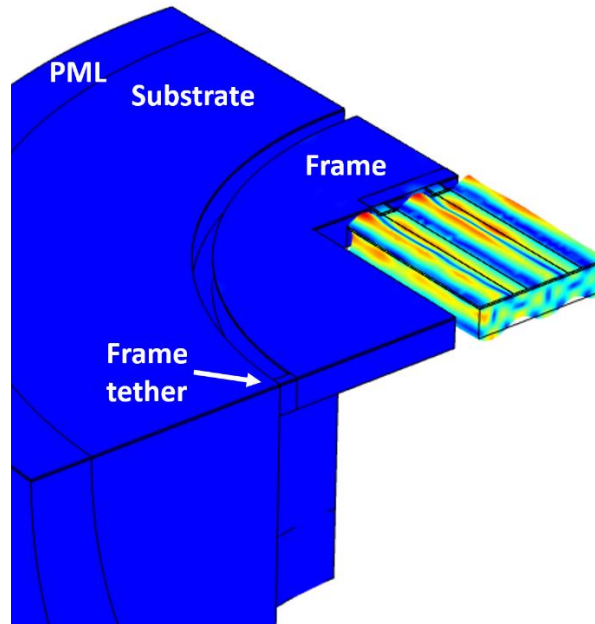


Figure 36. The PML based model developed for support loss prediction for a fundamental QLM TPoS resonator with an acoustic isolation frame. The resonator and frame dimensions are chosen to resemble the fabricated resonators.

Table 10. The modeled anchor quality factor for the resonator with and without acoustic isolation frame.

Mode shape	Q_{anc} without isolation-frame	Q_{anc} With isolation-frame
1 st harmonic QTLM TPoS	7.6 k	70 k

5.3.3 Turn Over Temperature in QTLM TPoS Resonators

Lamé mode resonators in highly n-type doped silicon are excellent choices for oven-controlled oscillator applications. For this application the oscillator operates at a constant elevated temperature. If this elevated temperature is close to the turn over-temperature of the resonator, the system would be robust to the errors of the control system.

For [100] aligned QTLM TPoS resonator, all the resonator boundaries would be aligned to [100] crystalline plane of silicon Figure 37. Therefore, it is expected that the temperature behavior of the [100]-aligned QTLM to be similar to planar Lamé modes fabricated on a 100 silicon substrate and reported before [89].

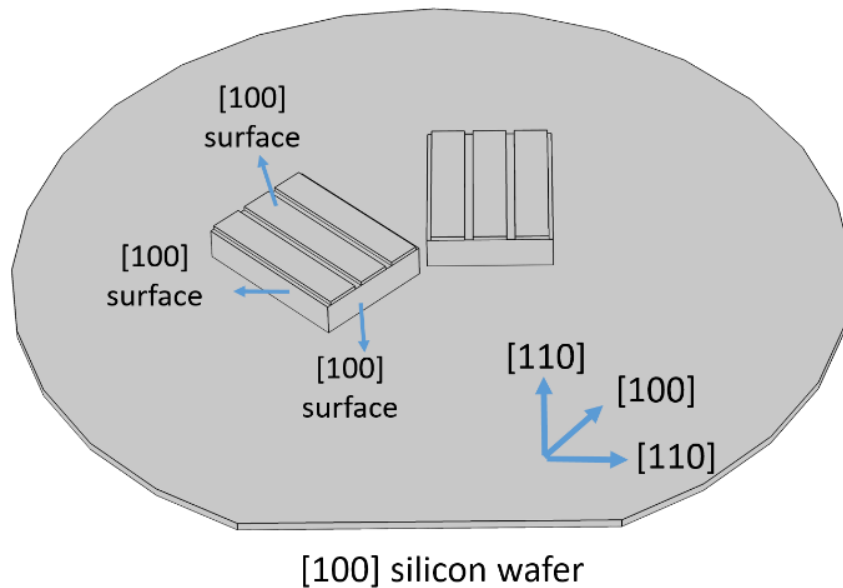


Figure 37. On a [100] silicon wafer, for the resonators aligned to [100] crystalline plane, should be rotated 45 degrees. All the faces of the resonator block are [100] which would be similar to the Lamé mode.

To predict the frequency-shift as a function of the temperature for QTLM TPoS resonators, a 2-D model of the whole stack of TPoS resonators is developed in COMSOL. The layer thicknesses in the model replicates the fabricated devices as follows: top Molybdenum 100 nm, Scandium doped AlN (ScAlN) 1 μm , bottom Molybdenum 100 nm and silicon 16 μm .

In order to develop TCF curves, stiffness values for silicon, AlN and Molybdenum and their temperature coefficients were borrowed from [16] (Table 11) for phosphorus doped single crystalline silicon ($n=6.6\times 10^{19} \text{ cm}^{-3}$), [90] and [91] for AlN and Molybdenum respectively. The temperature coefficient of elasticity (TCE) of AlN is assumed to be an adequate replacement for Scandium doped AlN TCE data.

Table 11. The elastic constants of Phosphorus-Doped ($n=6.6 \times 10^{19} \text{ cm}^{-3}$) Silicon and their corresponding first and second order temperature coefficients [16].

Dopant	C_{11}	C_{12}	C_{44}	$T_{C_{11}}^{(1)}$	$T_{C_{12}}^{(1)}$	$T_{C_{44}}^{(1)}$	$T_{C_{11}}^{(2)}$	$T_{C_{12}}^{(2)}$	$T_{C_{44}}^{(2)}$
	(GPa)	(GPa)	(GPa)	(ppm/°C)	(ppm/°C)	(ppm/°C)	(ppb/°C ²)	(ppb/°C ²)	(ppb/°C ²)
Phosphorus									
6.6×10^{19}	164.0	66.7	78.2	-34.2	-135.2	-67.8	-103	-1	-40

For single crystalline silicon, the stiffness matrix is calculated for each temperature using (5-1), (5-2) and (5-3):

$$C_{11t} = C_{110} + TC_{11}^1 \times C_{110} \times 10^{-6} \times (t - t_0) + TC_{11}^2 \times C_{110} \times 10^{-9} \times (t - t_0)^2 \quad (5-1)$$

$$C_{12t} = C_{120} + TC_{12}^1 \times C_{120} \times 10^{-6} \times (t - t_0) + TC_{12}^2 \times C_{120} \times 10^{-9} \times (t - t_0)^2 \quad (5-2)$$

$$C_{44t} = C_{440} + TC_{44}^1 \times C_{440} \times 10^{-6} \times (t - t_0) + TC_{44}^2 \times C_{440} \times 10^{-9} \times (t - t_0)^2 \quad (5-3)$$

Where C_{11t} , C_{12t} and C_{44t} are the single crystalline silicon stiffness coefficients at an arbitrary temperature t and C_{110} , C_{120} and C_{440} are the stiffness coefficient at room temperature (t_0).

The new stiffness matrix for silicon and stiffness values for ScAlN and Molybdenum is then used to repeat the modal analysis and to calculate the shifted resonance frequency.

The modeled TCF curves for TPoS resonators with FP 40 μm , 30 μm and 17 μm are shown in Figure 38. For the quasi thickness Lamé mode resonators (FP=17 μm), it was expected that the resonator behavior would be similar to the pure Lamé mode which is confirmed with our model.

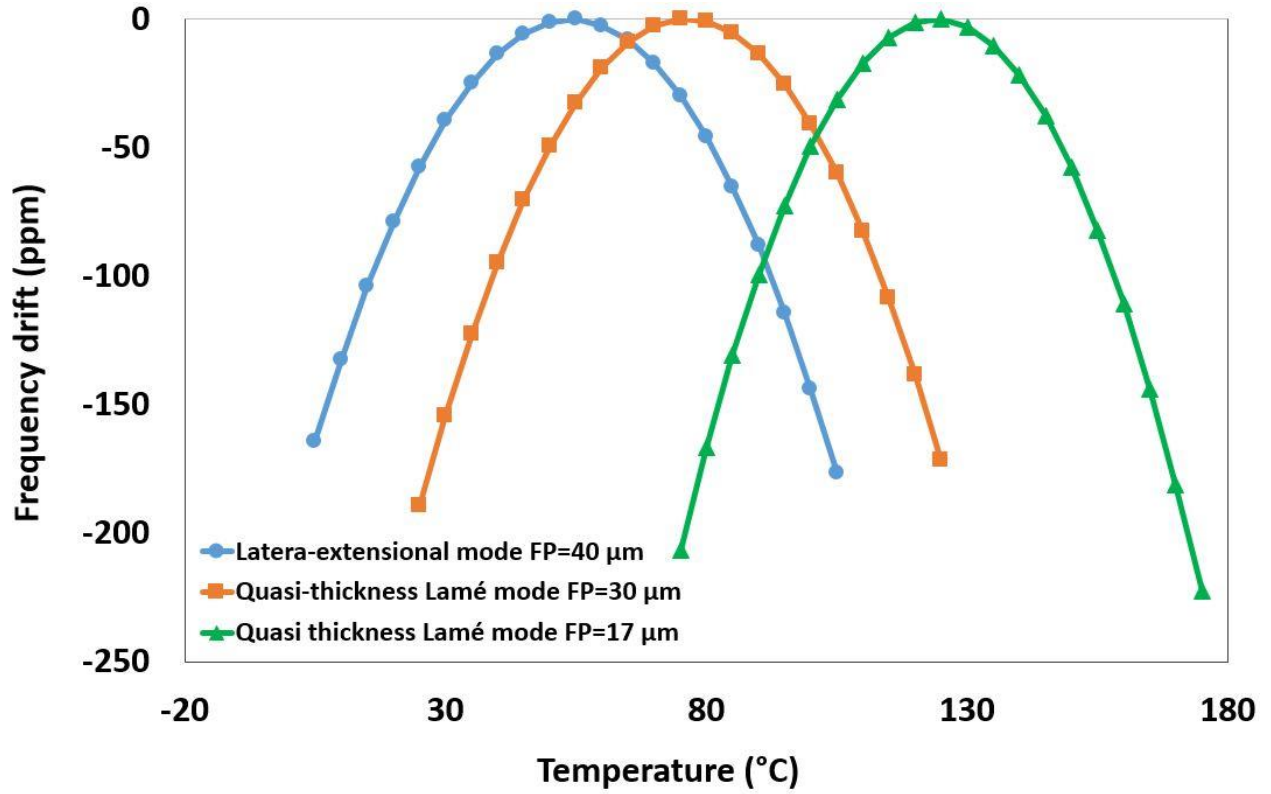


Figure 38. The modeled TCF curves for resonators with FP 40, 30 and 17 μm . The turn-over temperature shifts toward higher temperature as the FP/ T ratio approaches unity. Quasi Lamé mode shows the highest and lateral-extensional mode shows the lowest turn-over temperatures.

As the finger-pitch to thickness ratio increases the temperature-frequency behavior of the resonator transitions from what is known of pure Lamé to what is expected for extensional modes (i.e. the turnover temperature shifts down (Figure 39).

Therefore, the turn-over temperature in QTLM-TPoS resonators can be tuned lithographically by adjusting the FP/T ratio. This feature can be used to design resonators with the turn-over temperatures slightly above the desired temperature range for oven controlled oscillator application.

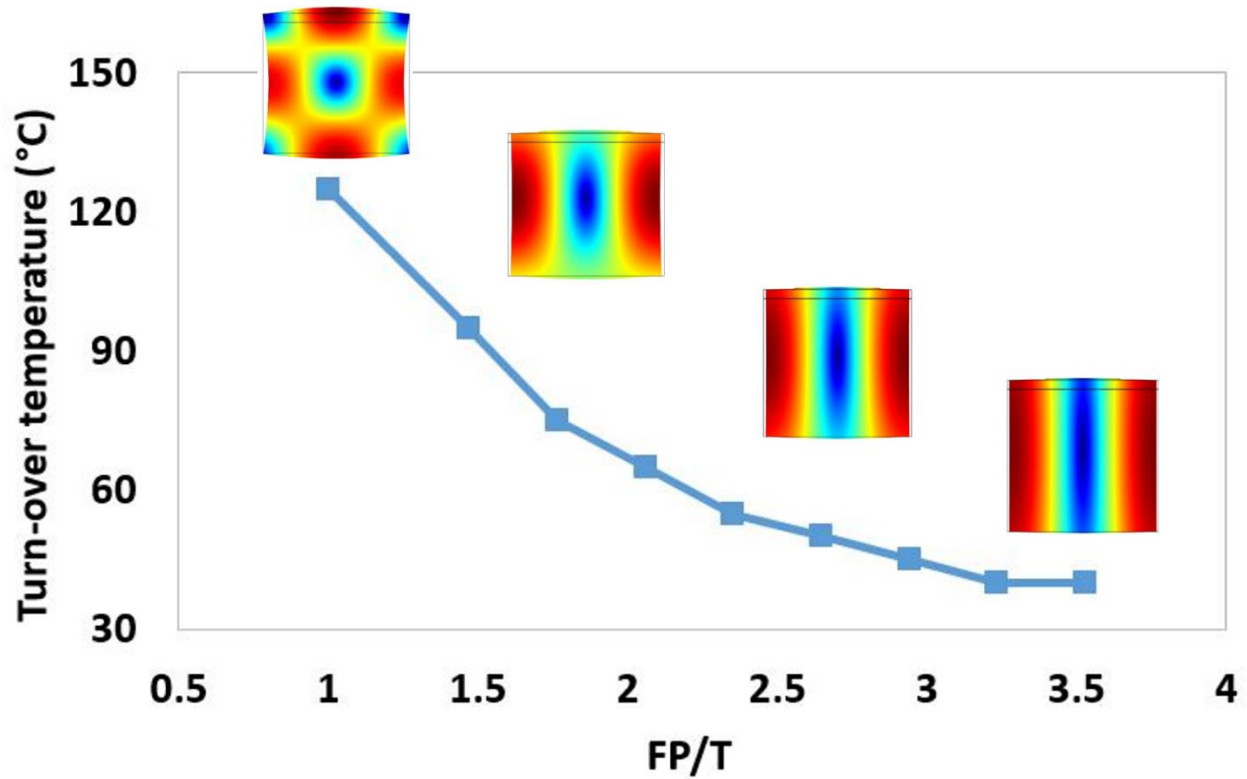


Figure 39. The Turn-over temperature of a QLM TPoS resonator as a function of FP/T ratio. Higher turn-over temperature is predicted for the resonators with FP/T ratio closer to one. The turn-over temperature could be adjusted lithographically.

The TCF curves are also modeled for higher harmonics of QTLM TPoS resonator. For these higher order modes, the turn-over temperatures are predicted to be slightly lower than the fundamental mode (turn-over temperature = 120 °C). For the temperature range reported in this study, TCE is negative for both AlN and Molybdenum and positive for highly doped silicon. The stress field is mostly concentrated in the center of the resonator (silicon portion) and because of that for the fundamental mode the TCF is mostly dominated by the silicon properties. On the other hand, for higher harmonic QTLM, a larger portion of the total stress field is in Mo/AlN/Mo compared to the fundamental

mode and therefore Mo/AlN/Mo stack impact on the TCF is larger hence lower turnover temperature is predicted for these higher order modes.

5.4 Experimental Results

The fabricated QTLM TPoS resonators are characterized in atmospheric pressure and partial vacuum using a ZNB8 network analyzer and a pair of GSG probes (from FormFactor inc) at ambient temperature. The loaded quality factors are measured and the unloaded quality factors are calculated using the motional resistance of the resonator. One port admittance response is also measured and the coupling coefficients are calculated using the measured parallel and series resonance frequencies. The temperature-frequency curves are also measured in a Janis cryogenic vacuum probe station.

TPoS resonators are fabricated on 16 μm thick silicon with finger pitches ranging from 40 μm (lateral-extensional mode) to 17 μm (fundamental QTLM), as well as 9 μm (2nd harmonic QTLM) and 6 μm (3rd harmonic QTLM).

The frequency response for the fundamental QTLM with and without acoustic isolation frame in air is shown in Figure 40. It is observed that, both quality factor and motional resistance are improved for the device with isolation frame. The measured unloaded quality factor of 16.2 k and motional resistance of 235 Ohm at 185 MHz for the fundamental QTLM resonator is amongst the best performance reported for any MEMS resonator at this frequency range ($f \times Q \sim 3 \times 10^{12}$). The measured Q's are in good

agreement with the trend predicted by our finite element COMSOL model for anchor quality factor.

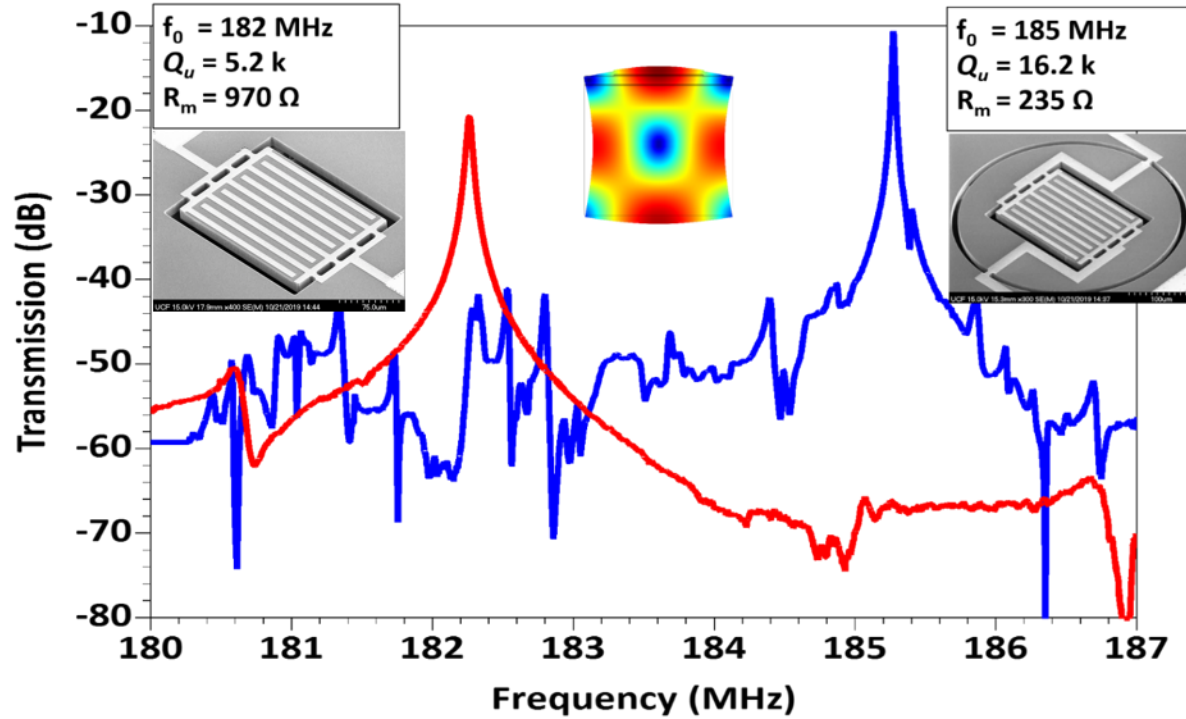


Figure 40. The measured frequency response in air for the fundamental QTLM TPoS resonator with and without acoustic isolation frame in air. The unloaded quality factor improved significantly by adding an isolation frame.

As shown in Figure 41, the frequency response for the fundamental QTLM TPoS resonator is also measured in partial vacuum. An unloaded quality factor of ~ 23.2 k is measured for this mode shape in vacuum resulting in an $f \times Q \sim 4.3 \times 10^{12}$.

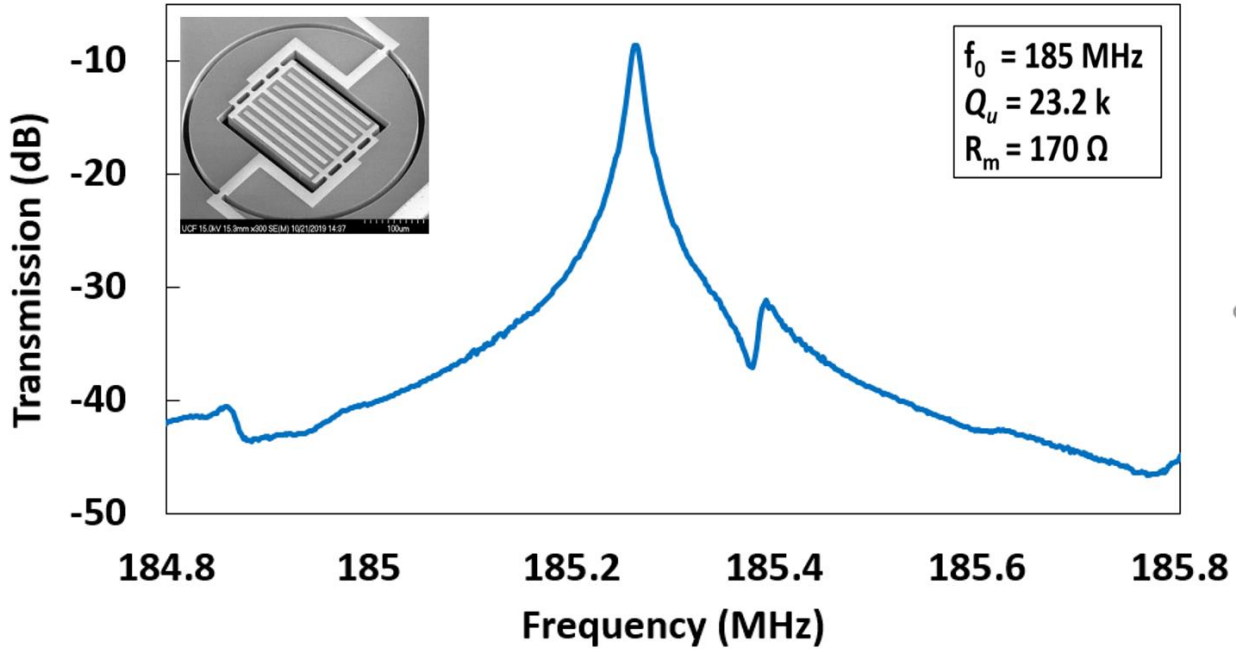


Figure 41 .The measured frequency response for the fundamental QTLM TPoS resonator in partial vacuum. Unloaded quality factor of 23.2 k is measured at 185 MHz for this resonance mode.

The measured frequency response for the second (FP=9 μm) and third (FP=6 μm) harmonic QTLM TPoS resonators are plotted in Figure 42 and Figure 43 respectively. We measure unloaded quality factors of 11.2 k and 5.5 k at 366 MHz and 555 MHz for the second and third harmonic QLM resonator. A $f \times Q$ of 4.1×10^{12} is measured for the second harmonic QLM TPoS resonator. The measured unloaded quality factor in vacuum is 12.6 k for the second harmonic and 6 k for the third harmonic QLM TPoS resonators. The TCF curves are measured for all three harmonics to confirm that the measured peaks are indeed quasi Lamé modes.

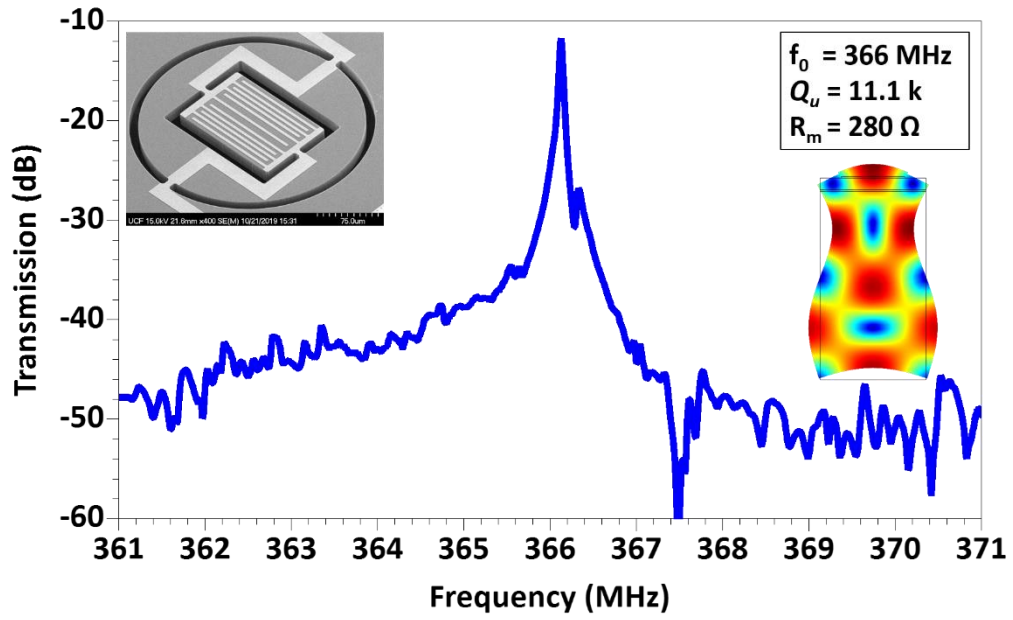


Figure 42. The measured frequency response for a 2nd harmonic QTLM TPoS resonator in air.

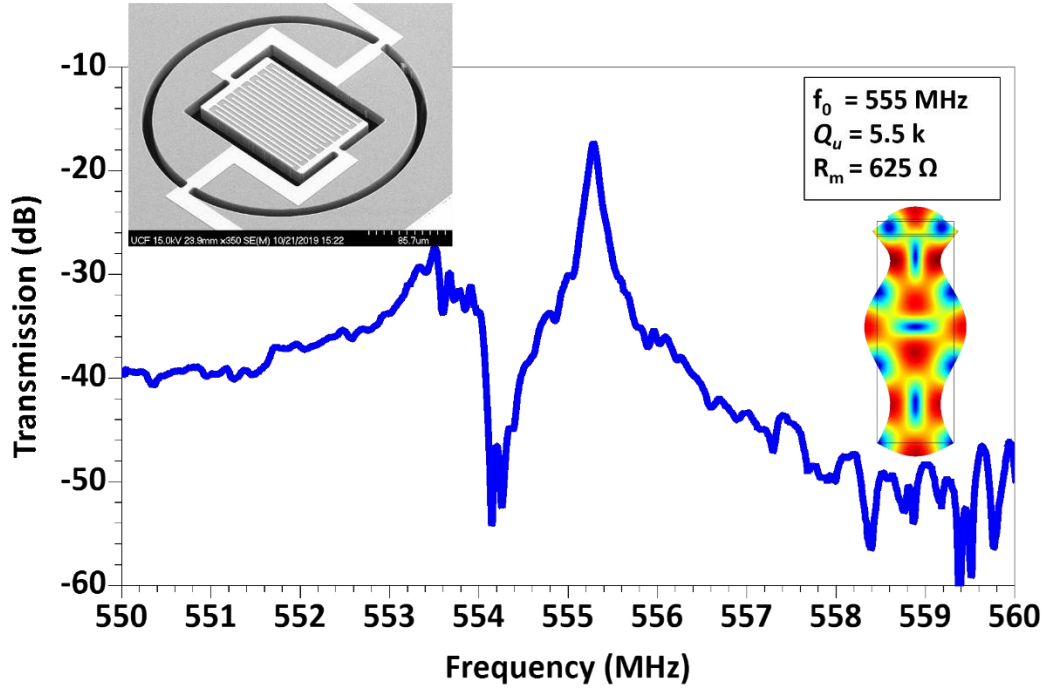


Figure 43. The measured frequency response for a 3rd harmonic QTLM TPoS resonator in air.

A wide spectrum is also measured for all three harmonics. We found that there is no strong spurious mode close to these Quasi Lamé modes. The second harmonic QTLM spectral response is plotted in Figure 44. A wide frequency range is deliberately chosen. It is apparent that there are no other strong modes in the vicinity of the QTLM.

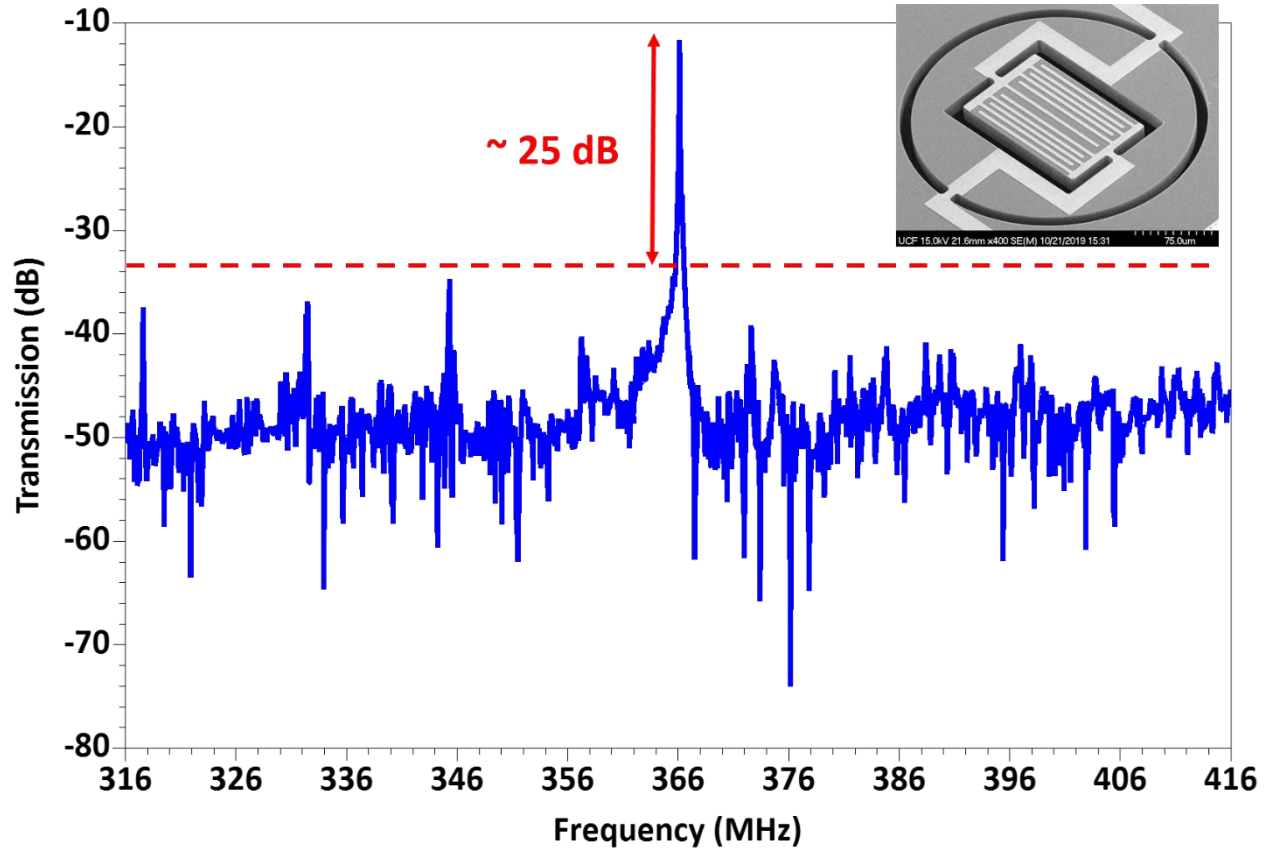


Figure 44. The wide spectrum frequency response for a second harmonic QLM TPoS resonator. There are no other strong peak close to this mode which make it a good candidate for oscillator application.

We calculate the coupling efficiencies from the measured series and parallel frequencies for five different resonators in each class and the highest measured coupling efficiencies are reported in Table 12. As shown in this table the coupling efficiency

improves by actuating higher harmonic QLM TPoS resonator. The measured coupling efficiencies are in good agreement with the finite element model.

Table 12. The measured coupling efficiencies for different classes of TPoS resonator.

Mode shape	FP (μm)	Modeled K_t^2
Lateral-extensional	40	0.21%
1 st harmonic QLM	17	0.02%
2 nd harmonic QLM	9	0.07%
3 rd harmonic QLM	6	0.1%

The TCF curves are also measured in vacuum probe station for Lateral extensional, quasi-thickness Lamé mode TPoS resonator. As reported in Figure 45, the TCF is measured for TPoS resonator with FP=40 μm , FP=30 μm and FP=17 μm and the measured data are in good agreement with the modeled TCF curves. We measure the turnover temperature of 45 °C, 80 °C and 150 °C for these devices respectively. Turnover temperatures reported for QTLM TPoS resonators are the highest turnover temperatures reported for piezoelectric actuated MEMS resonators without any additional over layers. Adding a silicon oxide layer would negatively impact both quality factor and electromechanical coupling efficiencies of the resonators which both are important

parameters in defining the noise floor in oscillator (negatively impact the phase noise and jitter) or other MEMS resonator applications.

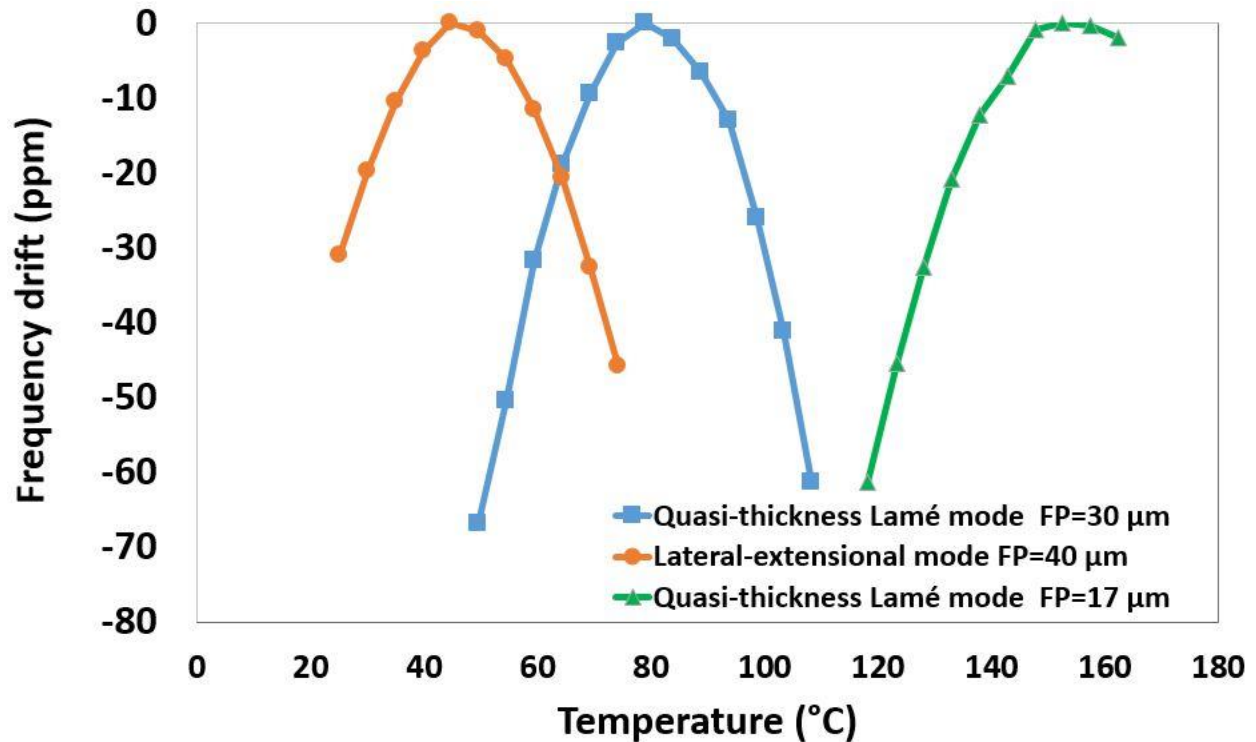


Figure 45. The measured CF curves for lateral-extensional, and quasi thickness Lamé mode resonators.

The quality factor of the fundamental QTLM TPoS resonator is compared to several other published results from resonators in the same range of frequencies in Table 13. The fundamental QTLM TPoS resonator offer the best quality factor even compared to measured quality factor for capacitive resonators for this range of frequencies. The low motional resistance of the fundamental mode QTLM TPoS resonator is almost an order of magnitude smaller than the capacitive counterparts.

Table 13. The measured quality factor for the fundamental QTLM TPoS resonator compared to a selected published results in the same frequency range.

Resonator Type	f_0 (MHz)	Q_{air} (k)	Q_{vac} (k)	R_m Ohm	Resonance mode	Reference
TPoS	185	16.2	23.2	235	Thickness Quasi Lamé	This work
Capacitive	173	9.3	-	18 k	Lamé	[82]
Capacitive	128	12	-	31 k	Lamé	[83]
TPoS	195	9.6	11.5	1.2 k	Radial	[55]
Capacitive	193	8.8	23	-	Radial	[58]

The measured data for Lateral extensional mode compared to QTLM resonators with properties transitioning from LE to QTLM is shown in Table 14 amongst which resonators with $FP=30\text{ }\mu\text{m}$ with turn-over temperature of $80\text{ }^{\circ}\text{C}$ is suitable for Oven-controlled oscillator application for commercial range of $-40\text{ }^{\circ}\text{C}$ to $80\text{ }^{\circ}\text{C}$. A measured frequency response for this resonator is plotted in Figure 46. As seen in the table, the turnover temperature of QTLM resonators can be tuned from $45\text{ }^{\circ}\text{C}$ to $150\text{ }^{\circ}\text{C}$ just by designing the FP of the resonator on the same wafer with the same doping level of the silicon layer. This phenomenon could be used to design resonators suitable for oven controlled oscillator applications over any desired temperature range.

Table 14. The measured data for Lateral extensional mode compared to QTLM resonators with properties transitioning from LE to QTLM.

Mode shape	FP (μm)	f_0 (MHz)	Q_{air} (k)	R_m (Ohm)	Turn-Over temperature ($^{\circ}\text{C}$)
Lateral- extensional	40	95	7.2	80	45
QTLM	30	125	8.2	120	80
QTLM	25	145	7.2	70	95
QTLM	20	170	13.5	225	140
QTLM	17	185	16.2	235	150

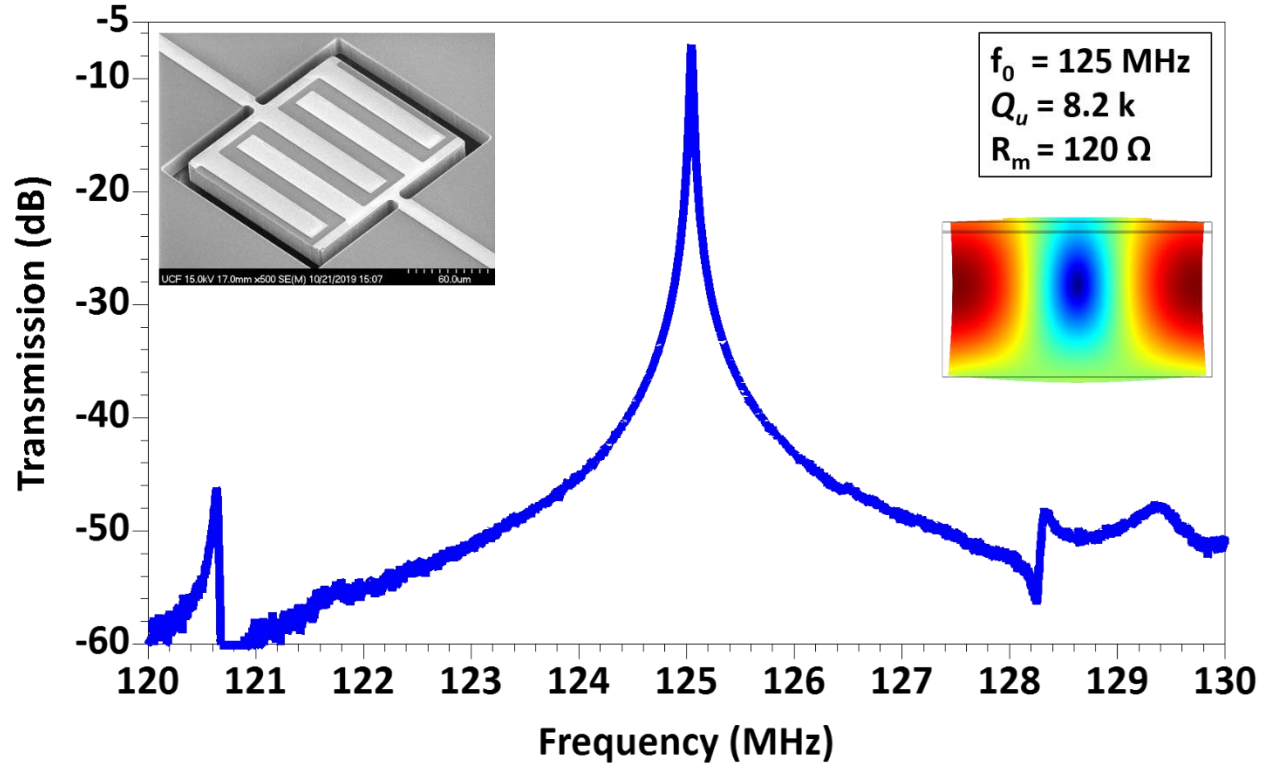


Figure 46. The measured frequency response for a quasi-thickness Lamé mode resonator with FP=30 μm .

5.5 Conclusions

Quasi thickness Lamé mode is successfully actuated in the thickness of Thin Film Piezoelectric on silicon resonators. Anchor quality factor is improved by designing an acoustic reflector frame for QTLM TPoS resonators. Higher harmonic QTLM is also excited in the cross section of the resonator. The resonators are fabricated on a 16 μm thick highly Arsenic doped silicon layer. A quality factor of 23.2 k is measured for the fundamental QTLM TPoS resonator at 185 MHz with a measured turn over temperature of above 100 $^{\circ}\text{C}$ which is the highest turn-over temperature reported for piezoelectric resonators without the need for any additional silicon oxide over layer. Quality factors of

12.6 k and 6 k is also measured at 366 MHz and 555 MHz for second and third harmonic QTLM TPoS resonator. High measured quality factor with low motional resistance and high turn –over temperature makes these resonators great candidate for oven controlled oscillator applications.

CHAPTER 6: TEMPERATURE COMPENSATION OF TPOS RESONATORS USING FLUORINE DOPED SILICON OXIDE

2

At room temperature, the thermal coefficient of elasticity (TCE) of silicon dioxide is positive [92], a distinctive feature that has been exploited for temperature compensation of acoustic resonators [93] [76] [94]. The most straightforward approach for temperature compensation using silicon dioxide, is to deposit a layer of silicon dioxide on the resonator. However, the silicon dioxide layer is known to cause degradation of the functionality (i.e. Q and loss) proportional to the thickness of the required overlay. An approach to avoid exceedingly thick oxide layers is to alter the chemistry of silicon dioxide in order to achieve larger positive TCE. For example, Fluorine-doped silicon dioxide (SiOF) deposited using a C2F6/TEOS chemistry have been found to exhibit TCE values larger than pure SiO₂ [95].

6.1 Temperature Compensation with Silicon Dioxide

The resonance frequency of lateral-extensional-mode thin film piezoelectric-on-substrate (TPoS) resonators is a function of the elastic properties of its constituting materials. Using the Taylor expansion for the resonance frequency (f_0) this relationship can be summarized as follows [96]:

² Material used in this chapter is partially taken from the published paper:

- S. Moradian, S. Shahraini and R. Abdolvand, "Temperature compensation of MEMS resonators using sputtered Fluorine-doped silicon dioxide," *2016 IEEE International Frequency Control Symposium (IFCS)*, New Orleans, LA, 2016, pp. 1-4. doi: 10.1109/IFCS.2016.7563551

$$f(T) \approx f_0 \sum_{n=1}^{\infty} \frac{\sum_{m=1}^{\infty} \frac{t_m}{v_m} \times TCF_{m,n} \times (T-T_0)^n}{\sum_{m=1}^N \frac{t_m}{v_m}} + f_0 \quad (6-1)$$

Where T_0 is the temperature corresponding to f_0 , T is the operating temperature, v_m is the speed of sound in the m th layer, t_m is the thickness of the m th layer. Here m indicates the layer number, and N is the number of layers in the resonator. The n th expansion of the TCF can be calculated as follows:

$$TCF_n = \frac{1}{n! f_0} \frac{\partial^n f_T}{\partial T^n} \quad (6-2)$$

The temperature coefficient of frequency (TCF) depends on the compound change in the elastic properties and thermal expansion of the layers making up the resonator. In the case of the materials in the resonators used in this paper the thermal expansion is insignificant in the studied temperature range thus making their contribution to frequency shift negligible. With this approximation the TCF can be calculated as [76]:

$$TCF_{m,n} = 0.5 \times TCE_{m,n} \quad (6-3)$$

The above equations are not accurate and did not agree with simulation and measurement results, furthermore there is no exact equation relating the resonance

frequency of a device to the constituting material. Nevertheless, (6-3) can be used as a rough guideline on the impact of various factors on the TCF of the resonator. According to (6-3) an oxide layer with an improved $\frac{TCE}{v_m}$ ratio compared to pure oxide is desired for temperature compensation applications.

It is already reported that low concentration of Fluorine in SiO₂ film could further increases its TCE [94]. Negative temperature coefficient of Frequency(TCF) of SAW and BAW devices caused by negative TCE of substrates such as ALN and Lithium niobate used in BAW and SAW devices respectively, could be reduced or cancel out (if designed properly). In these methods SiOF over-layer is deposited on the piezoelectric layer to cancel out its negative TCE.

Incorporation of Fluorine atoms into SiO₂ network could cause structural changes. High electronegative Fluorine ions could affect strength and length of the Si-O bonds in SiO₂ network and could cause the enlargement of Si-O-Si bond angle. These structural changes could shift Si-O stretching vibrational mode peak in the Fourier transform infrared spectra toward higher wave numbers as reported in several studies. The results reported in [94] shows that there is a strong correlation between the position of Si-O stretching peak and TCE of deposited film. Films with higher TCE have Si-O stretching peak with higher wave numbers. It was shown in several studies that Fluorine doped silicon dioxide films possess Si-O stretching peak with higher wave number in comparison with pure silicon dioxide.

Thin film SiO_2 exhibits different properties in comparison with bulk silica. These properties are closely related to deposition conditions of silicon dioxide films. Chemical vapor deposition is one of the methods which mostly used to deposit thin oxide films at low temperature. The other method which could be used to deposit Fluorine doped Silicon dioxide films is magnetron sputtering. With sputtering a wide variety of parameters such as power, substrate temperature, process pressure, target angle and distance between target and the substrate could be controlled. As a result, it is easier to control film properties with sputtering compared to depositing oxide with CVD. In this study reactive magnetron sputtering was used to sputter Fluorine doped SiO_2 films.

NF_3 gas is chosen for this work as the doping agent instead of C_xF_y and SF_6 gases which were used in several studies, due to its chemical stability and low health hazard compared to most other fluorine containing gases.

6.2 SiOF Structural Composition

Silicon dioxide possess a tetrahedral network as shown in Figure 47 .Each silicon atom is surrounded with four oxygen atoms and only linked through ring structure. n-fold rings are the rings with n Si-O-Si folder within the ring. Three and four fold rings mostly observed in the Raman spectroscopy of silicon dioxide films as reported in [97]. It has been assumed in the early studies of Fluorine doped silicon dioxide films that the presence of Si-F_n bonds changes the structural body of silicon dioxide significantly and cause transition of Si-O bonding from tetrahedral state SP^3 to planar state SP^2 and the above mentioned transition could cause enlargement of Si-O-Si bond angle and Si-O

bond strength. However, it was shown in [98] by molecular orbital modeling, that the presence of Fluorine atoms in the structural composition of Fluorine doped silicon dioxide does not significantly change structural body of SiOF and Si-O-Si bond angles Figure 48. Presence of two Fluorine atoms in the rings structure correspond to approximately 25 at. % of Fluorine in the structure of the film. Only minutes' change observed in the Si-O-Si bond with MO modeling which is not in agreement with the practical data. These structural changes in the Fluorine doped silicon dioxide film observed as shift and narrowing of Si-O stretching vibrational peak in Fourier Transform Infrared (FTIR) absorbance Spectrum.

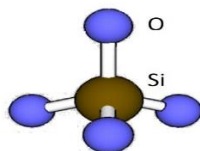


Figure 47. Si atom surrounded with four oxygen atom in a tetrahedral structure in SiO_2 .

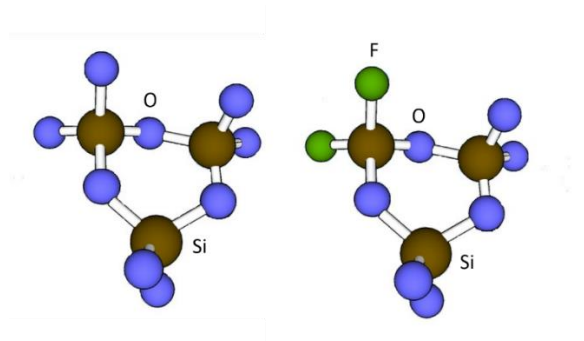


Figure 48. Threefold SiO_2 ring in the presence of Fluorine and without Fluorine.

The above mentioned structural changes are not the effect of Fluorine in the deposited film but the effect of highly active Fluorine radicals in the plasma. These active Fluorine radicals etch away SiOF film during the deposition process. These Fluorine

radicals break the bond of bridging Oxygen in the most strained rings. The probability of replacement of Fluorine atom in the place of oxygen is higher in the lower order rings since they possess most strained Si-O bond. As the result two n_1 and n_2 folder rings join and create a higher order ring with $n_1 + n_2 - 2$ folder ring structures as shown in Figure 49. The enlargement of Si-O-Si angle could be explained through ring structure changes and creation of higher order rings. The above mentioned shift in the stretching vibrational peak in FTIR absorbance spectrum could be explained with the enlargement of Si-O-Si angle θ . θ increases initially as the number of folders increases in the ring structure and then slightly decrease and saturates when the number of folders exceed 7 [98]. It is due to the increased flexibility of ring structure. In higher order rings (more than 7 folder), interaction between nearest Oxygen atoms determine the ring structure. The enlargement of θ creates larger voids in the film. The results are the creation of more porous films with smaller density.

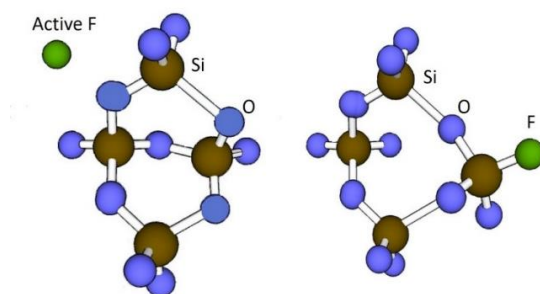


Figure 49. Transition of lower order rings to relaxed higher order rings in the presence of active Fluorine in the plasma.

6.3 Film Preparation

Fluorine doped SiO_2 films are sputtered on 4-inch P-type silicon wafers with $\langle 100 \rangle$ crystalline orientation. All films were deposited with AJA sputtering system using a 99.995%, 3" silicon dioxide target with Argon used as the ambient gas. Oxygen is added to fine tune the stoichiometry of the deposited SiO_x films prior to deposition of Fluorine doped films. Power, Temperature, process pressure and oxygen partial pressure of deposition process were characterized in order to achieve SiO_2 films with minimum extinction coefficient prior to usage of NF_3 in the process. At the end power of 205 W, temperature of 150 °C and process pressure of 2.5 mtorr and Oxygen partial pressure of 2.5% were used to deposit Fluorine doped SiO_2 layers. To deposit SIOF film, diluted NF_3 in Ar gas was introduced to the plasma in addition to Ar and O_2 gases. Various NF_3 partial pressure were used to achieve different concentration of Fluorine in the films. To fairly compare different films, the substrate temperature, deposition geometry (i.e. target-substrate distance, gun angle, and substrate rotation speed), power, base pressure, and substrate bias voltage are kept constant while the partial pressure of NF_3 is varied.

6.3.1 Refractive Index and Extinction Coefficient

Thickness, refractive index and extinction coefficient of each Fluorine doped SiO_2 film were measured at 632 nm wavelength with JAW ellipsometer. As shown in Figure 50,. refractive index decreases when NF_3 partial pressure increases. As explained in the previous section, active Fluorine radicals in the plasma attacks most strained Si-O bonds placed in the lower order ring and replace the Oxygen atoms in those bonds and create

Si-F termination bonds. Creation of more relaxed Higher order rings could lead to enlargement of nano-voids and porosity in the film. Enlargement of nano-voids could explain downturn in refractive index by increase of Fluorine concentration in the film.

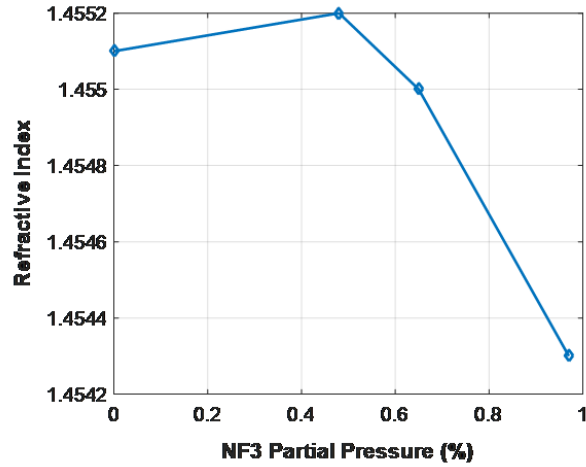


Figure 50. The Refractive index measured by ellipsometer for films deposited with different NF_3 partial pressure.

In fig.2 extinction coefficient is plotted as a function of NF_3 partial pressure. As seen, K decreases as the Fluorine concentration increases in the film.

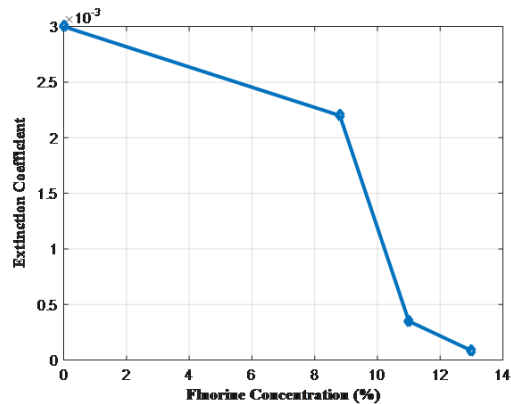


Figure 51. The Extinction coefficient of the films deposited with different NF_3 partial pressure.

6.3.2 FTIR Absorbance Spectrum

In order to plot absorbance spectrum, transmission spectrum of Fluorine doped SiO₂ films were measured by Fourier-transform infrared spectroscopy (FTIR) system. For background subtraction, an uncovered silicon wafer was used. Absorbance spectrum of the film can be formed with

$$A = -\log T \quad (6-4)$$

Where T is the transmission spectrum and A is the absorbance spectrum.

FTIR absorbance spectrum of Fluorine doped SiO₂ films with different NF₃ partial pressure are shown in Figure 52 in the wave number region of 700 Cm⁻¹ to 1400 Cm⁻¹ with a pitch of 3.85 Cm⁻¹. As reported in several studies, transverse optical (TO) phonon modes of SiO₂ films are located at 450 Cm⁻¹ and 800 (W3) Cm⁻¹ and 1070 (W4) Cm⁻¹ which correspond to rocking, bending and stretching vibrational mode of a typical Si-O bond respectively. Two of these peaks can be seen in the wave number region shown in Figure 52.

For Fluorine doped SiO₂ films, FTIR absorbance spectrum exhibit a stretching mode peak for Si-F bonds around 940 Cm⁻¹. IR absorption for Si-F stretching mode is increased in the film deposited with higher NF₃ partial pressure during deposition. As a result of Fluorine incorporation, Si-O stretching mode peak position shifts toward higher wave numbers. As Fluorine concentration increases in the film (Si-F stretching peak

becomes more intense), this peak shifts toward higher wave numbers and becomes narrower (FWHM decreases).

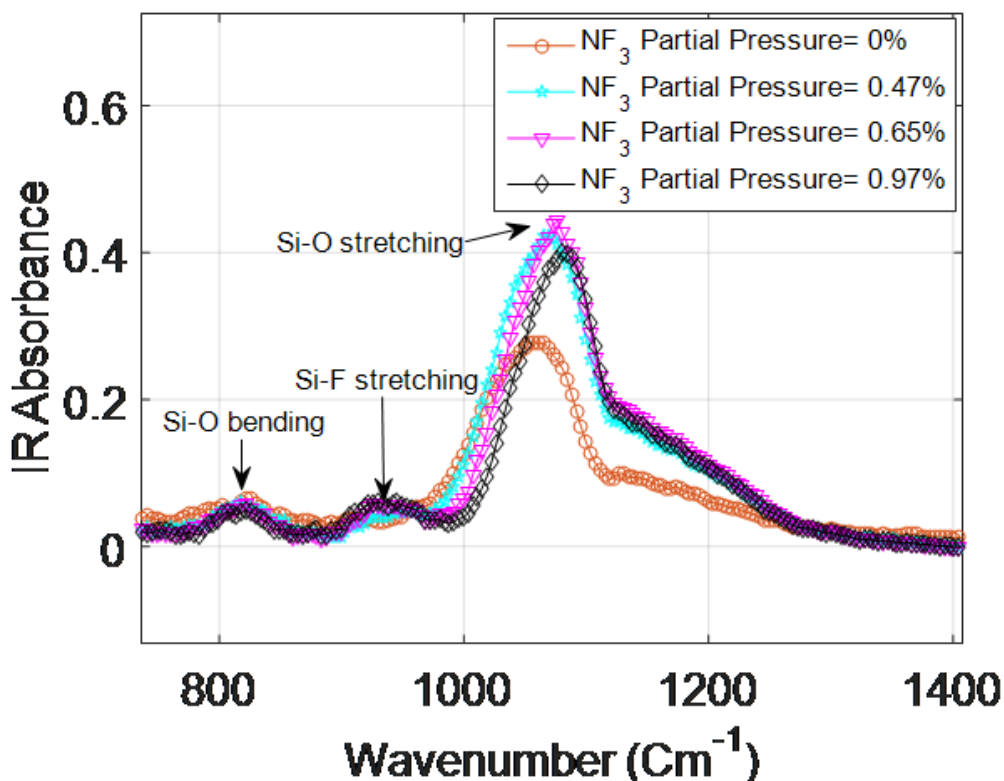


Figure 52. The normalized FTIR spectrum measured for different sputtered silicon oxide layers.

The peak shift for different levels of doping is a proof of depositing Fluorine doped silicon dioxide films using $\text{NF}_3/\text{O}_2/\text{Ar}$ chemistry. An increase in both the shift of the Si-O stretching peak and height of the Si-F stretching peak correspond with an increased level of doping.

6.3.3 SIMS Measurements

Doping concentration was measured using Secondary ion mass spectrometry (SIMS) and the results are shown in Fig.2. In this figure thickness is measured from the film surface. The maximum doping level achieved was $5.2 \times 10^{22} \text{ atoms/cm}^3$. This data shows that the fluorine concentration increases monotonically with NF_3 partial pressure in the studied partial pressure range. The fluorine concentration increases slightly with depth, for the 0.47% NF_3 partial pressure sample, while it peaks and then drops for the samples with higher partial pressure.

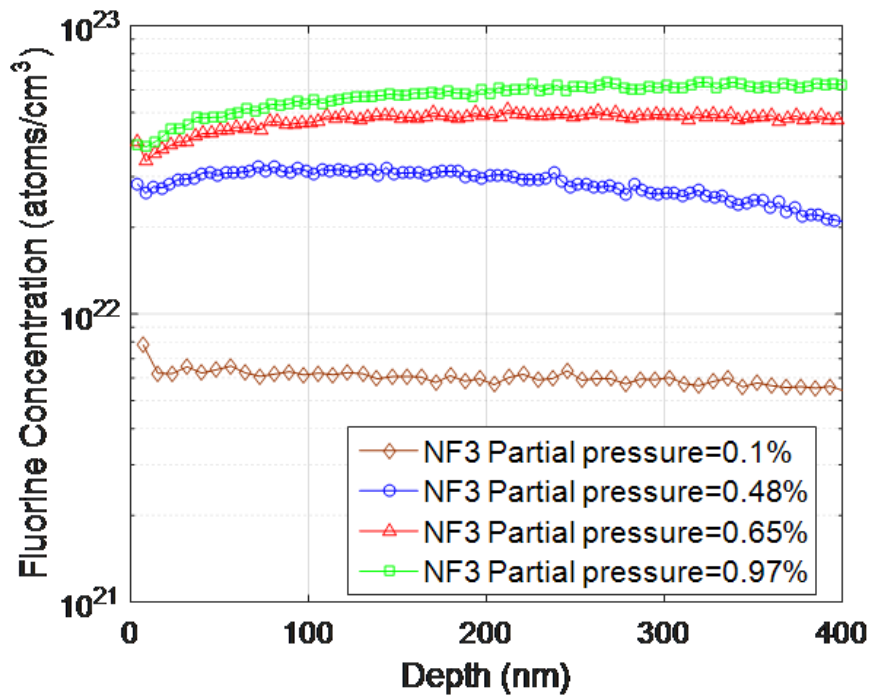


Figure 53. The Fluorine concentration profile measured for different sputtered Fluorine doped SiO_2 .

6.4 TPoS Resonators Passive Temperature Compensation with Fluorine Doped Silicon Oxide Over Layer

Pure oxide and Fluorine-doped silicon dioxide films were deposited on 0.5 μm AlN-on- 3 μm diamond resonators [99]. The schematic of the resonator is shown in Figure 54. The top metal interdigitated fingers enables efficient excitation of the first and the third lateral-extensional mode shapes (Figure 55). For this work we have used these resonators for their relatively thin substrate to enhance the effect of the overlay oxide on the overall TCF.

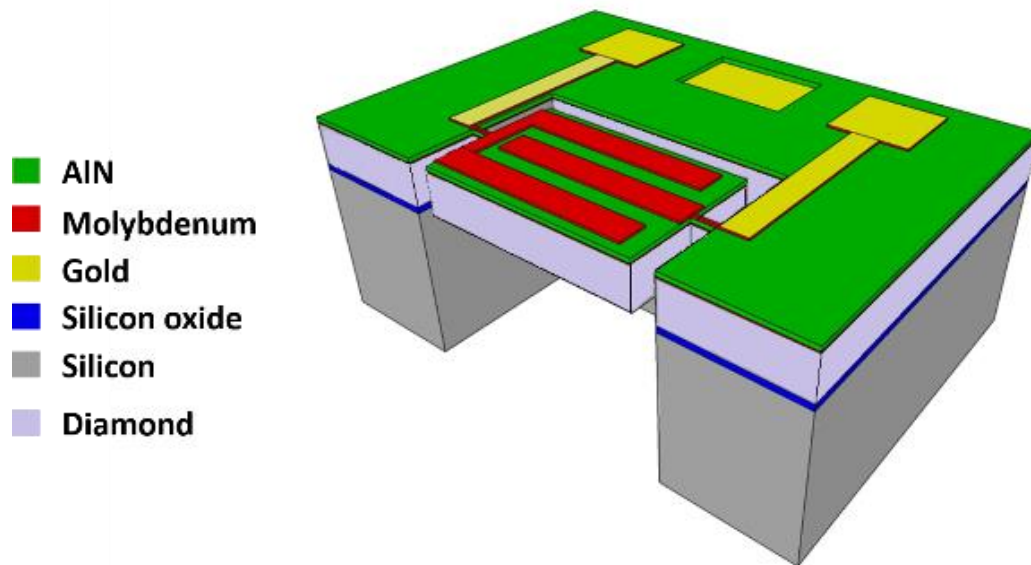


Figure 54. The schematic of TPoS resonators used for Fluorine doped oxide over layer deposition.

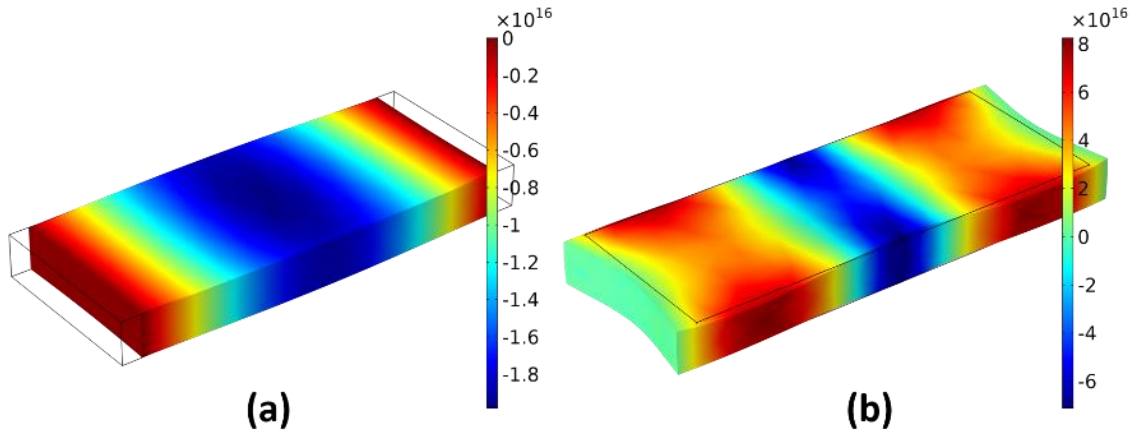


Figure 55. The stress field for the first order (a) and third order (b) Lateral extensional mode.

The frequency response of the resonators before and after deposition of a thin 800 nm film of pure oxide and 570 nm of fluorine-doped (6 at.%) oxide are reported in Figure 56. For both films the quality factor decreased after silicon oxide film deposition.

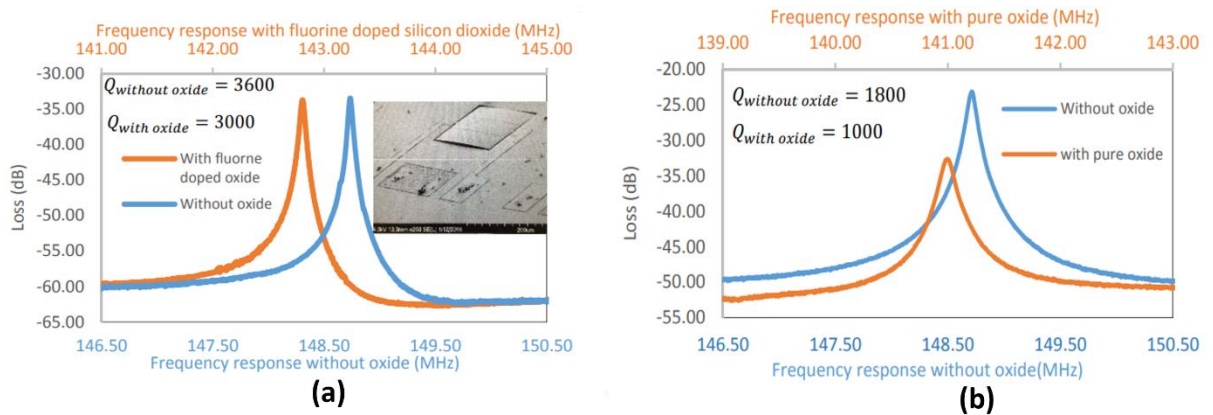


Figure 56. The frequency response of the TPOs resonators with and without oxide for (a) Fluorine doped silicon oxide and (b) pure silicon oxide.

The frequency drift for the TPOs resonators without any silicon oxide layer, with pure sputtered and PECVD silicon oxide and with two different level of Fluorine in the

oxide film is measured and plotted in Figure 57. Resonators with Fluorine doped silicon oxide have almost two times better temperature stability over the measured temperature range.

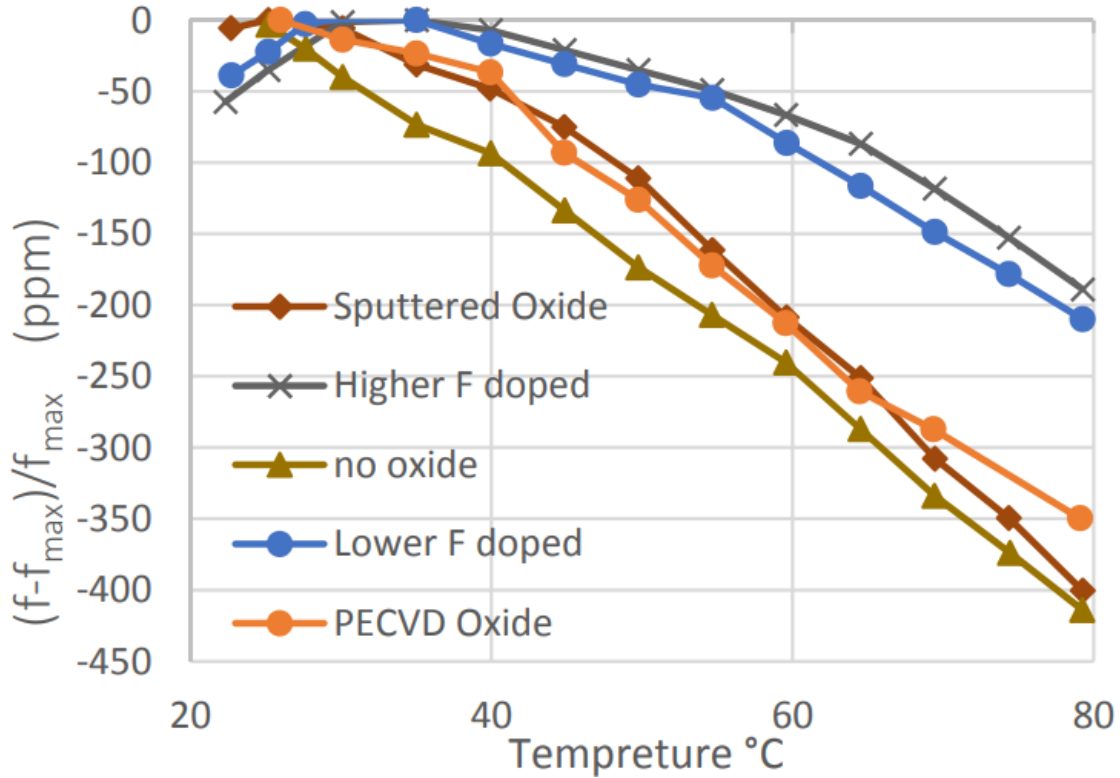


Figure 57. The measured frequency drift for LE TPoS resonators with different silicon oxide over layer. Resonators with Fluorine doped oxide over layer has almost two times better temperature stability over the measured temperature range.

6.5 Conclusions

Fluorine doped silicon oxide layers are successfully sputtered over TPoS resonators for passive temperature compensation using NF_3/Ar chemistry. The sputtered silicon oxide films are thoroughly characterized with FTIR, SIMS and films with 4 and 6 at.% of Fluorine are deposited on LE TPoS resonators. A twice smaller TCF is measured over

temperature range of 20 °C to 80 °C for the devices with Fluorine doped silicon oxide compared to the devices with Pure sputtered and PECVD silicon oxide over layer.

CHAPTER 7: CONCLUSIONS AND FUTURE WORKS

7.1 Accomplishments

In this dissertation we focused on the optimization of MEMS resonators for ultra-stable high frequency oscillator applications. Thin film piezoelectric on substrate is used as a platform for the resonator designs. The resonators are fabricated on single crystalline silicon with different doping level and different thickness and solutions are proposed and implemented for the resonator design to improve both deterministic a (temperature stability of the resonators) and non-deterministic (improving resonators quality factor) stability of the oscillator.

First we improved the quality factor by an order of magnitude for breathing mode disc resonators. For these resonators, anisotropy of single-crystalline silicon (SCS) is exploited to enable side-supported radial-mode thin-film piezoelectric-on-substrate (TPoS) disk resonators. In contrast to the case for isotropic material, it is demonstrated that the displacement of the disk periphery is not uniform for the radial-mode resonance in SCS disks. Specifically, for high-order harmonics, nodal points are formed on the edges, creating an opportunity for placing suspension tethers and enabling side-supported silicon disk resonators at the very high-frequency band with negligible anchor loss. In order to thoroughly study the effect of material properties and the tether location, anchor loss is simulated using a 3-D perfectly matched layer in COMSOL. Through modeling, it is shown that eighth-harmonic side-supported SCS disk resonators could potentially have orders of magnitude lower anchor loss in comparison to their

nonocrystalline diamond (NCD) disk resonator counterparts given the tethers are aligned to the [100] crystalline plane of silicon. It is then experimentally demonstrated that in TPoS disk, resonators fabricated on an 8- μm silicon-on-insulator (SOI) wafer, unloaded quality factor improves from ~ 450 for the second-harmonic mode at 43 MHz to ~ 11500 for the eighth-harmonic mode at 196 MHz if tethers are aligned to [100] plane. The same trend is not observed for NCD disk resonators and SCS disk resonators with tethers aligned to [110] plane. Finally, the temperature coefficient of frequency is simulated and measured for the radial-mode disk resonators fabricated on the 8- μm -thick degenerately n-type doped SCS, and the TFC data are utilized to guarantee proper identification of the harmonic radial-mode resonance peaks among others.

Next, Fluorine doped SiO_2 layers were deposited on silicon wafers by reactive magnetron sputtering with $\text{NF}_3/\text{Ar}/\text{O}_2$ chemistry. Different NF_3 partial pressure from 0% to 0.97% were used to form films with various Fluorine Concentration. Fluorine concentration of deposited films were characterized by measurements of the area of Si-F stretching vibrational mode peak relative to Si-O stretching mode peak in Fourier transform Infrared (FTIR) absorbance spectrum. Relation between Fluorine atom count in the films and NF_3 partial pressure was studied by Secondary Ion Mass Spectrometry (SIMS). Atom count of Fluorine increased when NF_3 partial pressure increased in the deposition process. optical properties and FTIR absorbance spectrum of the films are measured. This fluorine doped silicon oxide film is deposited as an over layer on TPoS resonators and frequency drift almost half of what was achieved with pure oxide is measured for these resonators.

Finally, Thickness-Lamé (TL) mode piezoelectrically-transduced silicon resonators are studied and demonstrated. It will be shown that unlike Planar-Lamé resonance modes, Thickness-Lamé modes could be efficiently excited using sputtered polycrystalline piezoelectric films such as Scandium Aluminum Nitride (ScAlN) as both d_{31} and d_{33} piezoelectric coefficients of ScAlN constructively contribute in the coupling coefficient. Moreover, it is shown through finite element analysis and experimental results that the coupling coefficient improves with the order of the TL harmonic mode excited in a silicon slab. It is also shown that the quality-factor of TL resonators substantially enhances through utilization of properly-designed acoustic reflectors (i.e. acoustic isolation frames) around the tethered resonator block. Temperature coefficient of frequency is also modeled using finite-element eigen-frequency analysis. It is shown that the turn-over temperature of resonators aligned to $\langle 100 \rangle$ plane of a degenerately-doped n-type silicon substrate varies considerably as the mode shape transitions from a Thickness- Lamé to a Lateral-Extensional mode by varying the electrode size (i.e. finger pitch). A record Q of 23.2k is measured for a ~ 185 MHz fundamental TL resonator in vacuum ($f \times Q = 4.3 \times 10^{12}$) while quality factors of 12.6k and 6k are also measured in vacuum for second and third harmonic TL resonators at 326 MHz and 555 MHz respectively. The combination of turn-over temperatures of above 80 °C, high quality factor, and low motional resistance, promises the suitability of such resonators for extremely-stable oven-controlled oscillator applications.

Another research opportunity is to design high frequency (GHz range) QTLM on AlN / Si platform. For high frequency resonator, if the thickness of the piezoelectric film approaches half wavelength of the thickness Lamé mode, the electromechanical coupling efficiencies could be improved significantly.

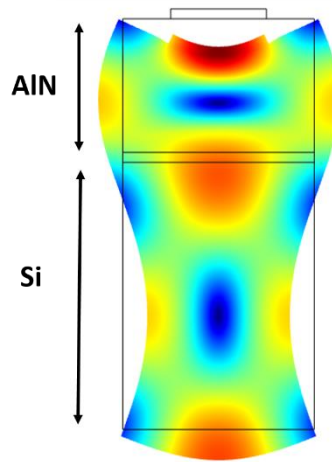


Figure 59. The proposed high order QTLM TPoS resonator.

As reported in [16], $\langle 110 \rangle$ aligned Lamé on highly p-type doped silicon offers less than 150 ppm frequency drift over the full temperature range. The proposed high frequency resonators could be fabricated on the highly p-type doped silicon wafer for passive temperature compensation.

In general, QTLM TPoS resonators could be designed and implemented on LiNbO_3 platform for improved coupling efficiencies. However, large negative TCF of LiNbO_3 could increase the TCF of the TPoS resonator.

**APPENDIX: PERMISSIONS FOR REUSING THE PUBLISHED PAPERS
[23, 53, 93,94] IN THE DISSERTATION**

- IEEE (

- **Does IEEE require individuals working on a thesis or dissertation to obtain formal permission for reuse?**

The IEEE does not require individuals working on a thesis to obtain a formal reuse license, however, you must follow the requirements listed below:

Textual Material

Using short quotes or referring to the work within these papers) users must give full credit to the original source (author, paper, publication) followed by the IEEE copyright line © 2011 IEEE.

In the case of illustrations or tabular material, we require that the copyright line © [Year of original publication] IEEE appear prominently with each reprinted figure and/or table.

If a substantial portion of the original paper is to be used, and if you are not the senior author, also obtain the senior author's approval.

Full-Text Article

If you are using the entire IEEE copyright owned article, the following IEEE copyright/ credit notice should be placed prominently in the references: © [year of original publication] IEEE. Reprinted, with permission, from [author names, paper title, IEEE publication title, and month/year of publication]

Only the accepted version of an IEEE copyrighted paper can be used when posting the paper or your thesis on-line.

REFERENCES

- [1] H. Chang, L. Wei Qin, G. Yuan and W. Yuan, "An Integrated MEMS Gyroscope Array with Higher Accuracy Output," *Sensors*, vol. 8, no. 4, 2008.
- [2] V. K. Varadan, W. D. Suh, P. B. Xavier, K. A. Jose and V. V. Varadan, "Design and development of a MEMS-IDT gyroscope," *Smart Materials and Structures*, vol. 9, no. 6, 2000.
- [3] H. Luo, G. K. Fedder and L. R. Carley, "A 1 mG lateral CMOS-MEMS accelerometer," in *IEEE Thirteenth Annual International Conference on Micro Electro Mechanical Systems*, Miyazaki, Japan, 2000.
- [4] H. G. Yu, L. Zou, K. Deng, R. Wolf, S. Tadigadapa and S. Troler-McKinstry, "Lead zirconate titanate MEMS accelerometer using interdigitated electrodes," *Sensors and Actuators A: Physical*, vol. 107, no. 1, pp. 26-35, 2003.
- [5] S. Choi, N. Kim and R. Ha, "Micro Sensor Node for Air Pollutant Monitoring: Hardware and Software Issues," *Sensors*, vol. 9, no. 10, 2009.
- [6] M. Takeda, "Applications of MEMS to industrial inspection," in *IEEE International Conference on Micro Electro Mechanical Systems*, Interlaken, Switzerland, 2001.

- [7] A. Abdul Razak, A. Zayegh, R. K. Begg and Y. Wahab, "Foot Plantar Pressure Measurement System: A Review," *Sensors*, vol. 12, no. 7, p. 9884–9912, 2012.
- [8] E. Y. Chow, A. L. Chlebowski, S. Chakraborty, W. J. Chappell and P. P. Irazoqui, "Fully Wireless Implantable Cardiovascular Pressure Monitor Integrated with a Medical Stent," *IEEE Transactions on Biomedical Engineering*, vol. 57, no. 6, pp. 1487-1496, 2010.
- [9] H. J. Lee, N. Choi, E. Yoon and I. Cho, "MEMS devices for drug delivery," *Elsevier*, vol. 128, pp. 132-147, 2018.
- [10] S. Karman, F. Ibrahim and N. Soin, "A review of MEMS drug delivery in medical application," in *3rd Kuala Lumpur International Conference on Biomedical Engineering*, 2006.
- [11] S. Pourkamali, R. Abdolvand, G. K. Ho and F. Ayazi, "Electrostatically coupled micromechanical beam filters," in *17th IEEE International Conference on Micro Electro Mechanical Systems*, Maastricht, Netherlands, 2004.
- [12] R. Abdolvand and F. Ayazi, "High-frequency monolithic thin-film piezoelectric-on-substrate filters," *International Journal of Microwave and Wireless Technologies*, vol. 1, no. 1, pp. 29-35, 2009.

- [13] M. Shahmohammadi, M. J. Modarres-Zadeh and R. Abdolvand, "Low jitter thin-film piezoelectric-on-substrate oscillators," in *IEEE International Frequency Control Symposium*, Newport Beach, CA, 2010.
- [14] R. Abdolvand, B. Bahreyni, J. E. Y. Lee and F. Nabki, "Micromachined resonators: A review," *Micromachines*, vol. 7, no. 9, p. 160, 2016.
- [15] C. Zuo, N. Sinha, J. Van der Spiegel and G. Piazza, "Multifrequency Pierce Oscillators Based on Piezoelectric AlN Contour-Mode MEMS Technology," *Journal of Microelectromechanical Systems*, vol. 19, no. 3, pp. 570-580, 2010.
- [16] E. J. Ng, V. A. Hong, Y. Yang, C. H. Ahn, C. L. M. Everhart and T. W. Kenny, "Temperature Dependence of the Elastic Constants of Doped Silicon," *Journal of Microelectromechanical Systems*, vol. 24, no. 3, pp. 730-741, 2015.
- [17] M. Bao and H. Yang, "Squeeze film air damping in MEMS," *Sens. Actuat. A*, 2007.
- [18] M. Y. Elsayed and F. Nabki, "870 000 Q-Factor Capacitive Lamé Mode Resonator With Gap Closing Electrodes Enabling 4.4 k Ohm Equivalent Resistance at 50 V," *IEEE Transactions on Ultrasonics, Ferroelectrics, and Frequency Control*, vol. 66, no. 4, pp. 717-726, 2019.
- [19] M. U. Demirci and C. T. C. Nguyen, "Mechanically corner-coupled square microresonator array for reduced series motional resistance," *Journal of Microelectromechanical Systems*, vol. 15, no. 6, pp. 1419-1436, 2006.

- [20] S. Pourkamali, G. K. Ho and F. Ayazi, "Low-impedance VHF and UHF capacitive silicon bulk acoustic wave resonators—Part I: concept and fabrication," *IEEE Transactions on Electron Devices*, vol. 54, no. 8, pp. 2017-2023, 2007.
- [21] A. Bhave and R. T. Howe, "Silicon nitride-on-silicon bar resonator using internal electrostatic transduction," in *International Conference on Solid-State Sensors, Actuators and Microsystems (TRANSDUCERS '05)*, 2005.
- [22] L. Yu-Wei, L. Sheng-Shian, X. Yuan, R. Zeing and C. T. C. Nguyen, "Vibrating micromechanical resonators with solid dielectric capacitive transducer gaps," in *Frequency Control Symposium and Exposition*, 2005.
- [23] S. Shahraini, M. Shahmohammadi and R. Abdolvand, "Support loss evasion in breathing-mode high-order silicon disc resonators," in *IEEE International Ultrasonics Symposium (IUS)*, Washington, DC, 2017.
- [24] C. Cassella, G. Chen, Z. Qian, G. Hummel and M. Rinaldi, "Cross-Sectional Lamé Mode Ladder Filters for UHF Wideband Applications," *IEEE Electron Device Letters*, vol. 37, no. 5, pp. 681-683, 2016.
- [25] G. Piazza, P. J. Stephanou and A. P. Pisano, "Piezoelectric Aluminum Nitride Vibrating Contour-Mode MEMS Resonators," *Journal of Microelectromechanical Systems*, vol. 15, no. 6, pp. 1406-1418, 2006.

- [26] M. Feneberg and K. Thonke, "Polarization fields of III-nitrides grown in different crystal orientations," *Journal of Physics: Condensed Matter*, vol. 19, no. 40, 2007.
- [27] L. Colombo, A. Kochhar, C. Xu, G. Piazza, S. Mishin and Y. Oshmyansky, "Investigation of 20% scandium-doped aluminum nitride films for MEMS laterally vibrating resonators," in *2017 IEEE International Ultrasonics Symposium (IUS)*, Washington, DC, 2017.
- [28] H. Fatemi and R. Abdolvand, "Low-loss lateral-extensional piezoelectric filters on ultrananocrystalline diamond," *IEEE transactions on ultrasonics, ferroelectrics, and frequency control*, vol. 60, no. 9, pp. 1978-1988, 2013.
- [29] B. P. Harrington and R. Abdolvand, "In-plane acoustic reflectors for reducing effective anchor loss in lateral–extensional MEMS resonators," *Micromechanics and Microengineering*, vol. 21, no. 8, 2011.
- [30] H. Fatemi and R. Abdolvand, "Fracture limit in thin-film piezoelectric-on-substrate resonators: Silicon VS. diamond," in *International Conference on Micro Electro Mechanical Systems (MEMS)*, Taipei, 2013.
- [31] M. Shahmohammadi, B. P. Harrington and R. Abdolvand, "Turnover Temperature Point in Extensional-Mode Highly Doped Silicon Microresonators," *IEEE Transactions on Electron Devices*, vol. 60, no. 3, pp. 1213-1220, 2013.

- [32] R. Abdolvand, H. M. Lavasani, G. K. Ho and F. Ayazi, "Thin-film piezoelectric-on-silicon resonators for high-frequency reference oscillator applications," *IEEE Transactions on Ultrasonics, Ferroelectrics, and Frequency Control*, vol. 55, no. 12, pp. 2596-2606, 2008.
- [33] J. T. M. Beek and R. Puers, "A review of MEMS oscillators for frequency reference and timing applications," *Journal of Micromechanics and Microengineering*, vol. 22, no. 1, 2011.
- [34] D. B. Leeson, "A simple model of feedback oscillator noise spectrum," *Proceedings of the IEEE*, vol. 54, no. 2, pp. 329-330, 1966.
- [35] S. Mishin, D. R. Marx, B. Sylvia, V. Lughi, K. L. Turner and D. R. Clarke, "Sputtered AlN thin films on Si and electrodes for MEMS resonators: relationship between surface quality microstructure and film properties," in *IEEE Symposium on Ultrasonics*, Honolulu, HI, USA, 2003.
- [36] T. Yokoyama, T. Nishihara, S. Taniguchi, M. Iwaki, Y. Satoh, M. Ueda and T. Miyashita, "New electrode material for low-loss and high-Q FBAR filters," in *IEEE Ultrasonics Symposium*, Montreal, Quebec, Canada, 2004.
- [37] E. A. Gulbransen and W. S. Wyson, "Thin oxide films on molybdenum," *Trans. AIME Met. Div.*, vol. 175, pp. 628-647, 1948.

- [38] R. Abdolvand, H. Fatemi and S. Moradian, Quality Factor and Coupling in Piezoelectric MEMS Resonators in Piezoelectric MEMS resonators, Switzerland: Springer Nature, 2017.
- [39] T. O. Woodruff and H. Ehrenreich, "Absorption of sound in insulators," *Physical Review*, vol. 123, no. 5, 1961.
- [40] A. S. Nowick, Anelastic relaxation in crystalline solids, Elsevier, 2012.
- [41] R. Tabrizian, M. Rais-Zadeh and F. Ayazi, "Effect of phonon interactions on limiting the f.Q product of micromechanical resonators," in *TRANSDUCERS*, 2009.
- [42] S. Fernandez, M. Cremonesi, C. Cassella, A. Frangi and G. Piazza, "Anchor losses in AlN contour mode resonators," *microelectromechanical systems*, vol. 24, no. 2, pp. 265-275, 2015.
- [43] S. Gong, N. K. Kuo and G. Piazza, "GHz AlN lateral overmoded bulk acoustic wave resonators with a $f \cdot Q$ of 1.17×10^{13} ," in *IEEE International Frequency Control and the European Frequency and Time Forum (FCS)*, San Fransisco, CA, 2011.
- [44] Z. L. Hao and B. X. Liao, "An analytical study on interfacial dissipation in piezoelectric rectangular block resonators with in-plane longitudinal-mode vibrations," *Sensor Actuat. A: Phys*, vol. 163, pp. 401-409, 2010.

- [45] W. Kun, A. C. Wong and C. T. C. Nguyen, "VHF free-free beam high-Q micromechanical resonators," *Microelectromechanical systems*, vol. 9, no. 3, 2000.
- [46] W. Jing, Z. Ren and C. T. C. Nguyen, "1.156-GHz self-aligned vibrating micromechanical disk resonator," *IEEE Trans Ultrason Ferroelectr Freq Control*, vol. 51, no. 12, p. 1607–1628, 2004.
- [47] S. S. Li, Y. W. Lin, Y. Xie, Z. Ren and C. T. C. Nguyen, "Micromechanical "hollow-disk" ring resonators," in *IEEE international conference on (MEMS) micro electro mechanical systems*, 2004.
- [48] J. Lee, J. Yan and A. A. Seshia, "Study of lateral mode SOI-MEMS resonators for reduced anchor loss," *Micromechanics and Microengineering*, vol. 21, no. 4, 2011.
- [49] F. Hsu, J. Hsu, T. Huang, C. Wang and P. Chang, "Design of lossless anchors for microacoustic-wave resonators utilizing phononic crystal strips," *Applied Physics Letters*, vol. 98, no. 14, 2011.
- [50] L. Sorenson, J. L. Fu and F. Ayazi, "One-dimensional linear acoustic bandgap structures for performance enhancement of AlN-on-silicon micromechanical resonators," in *TRANSDUCERS*, 2011.
- [51] V. Tas, S. Olcum, M. D. Aksoy and A. Atalar, "Reducing anchor loss in micromechanical extensional mode resonators," *IEEE Transactions on*

- Ultrasonics, Ferroelectrics, and Frequency Control*, vol. 57, no. 2, pp. 448-454, 2010.
- [52] M. Pandey, R. B. Reichenbach, A. T. Zehnder, A. Lal and H. G. Craighead, "Reducing Anchor Loss in MEMS Resonators Using Mesa Isolation," *Journal of Microelectromechanical Systems*, vol. 18, no. 4, pp. 836-844, 2009.
- [53] M. Y. Elsayed, P. V. Cicek, F. Nabki and M. N. El-Gamal, "Bulk Mode Disk Resonator With Transverse Piezoelectric Actuation and Electrostatic Tuning," *Journal of Microelectromechanical Systems*, vol. 25, no. 2, pp. 252-261, 2016.
- [54] M. Y. Elsayed and F. Nabki, "Piezoelectric Bulk Mode Disk Resonator Post-Processed for Enhanced Quality Factor Performance," *Journal of Microelectromechanical Systems*, vol. 26, no. 1, pp. 75-83, 2017.
- [55] S. Shahraini, M. Shahmohammadi, H. Fatemi and R. Abdolvand, "Side-Supported Radial-Mode Thin-Film Piezoelectric-on-Silicon Disk Resonators," *IEEE Transactions on Ultrasonics, Ferroelectrics, and Frequency Control*, vol. 66, no. 4, pp. 727-736, 2019.
- [56] B. P. Harrington, M. Shahmohammadi and R. Abdolvand, "Toward ultimate performance in GHZ MEMS resonators: Low impedance and high Q," in *IEEE 23rd International Conference on Micro Electro Mechanical Systems (MEMS)*, Wanchai, Hong Kong, 2010.

- [57] R. A. a. C. T. N. Schneider, "On/off switchable high-Q capacitive-piezoelectric AlN resonators," in *Micro Electro Mechanical Systems (MEMS)*, 2014.
- [58] J. R. Clark, W. T. Hsu, M. A. Abdelmoneum and C. T. C. Nguyen, "High-Q UHF micromechanical radial-contour mode disk resonators," *Journal of Microelectromechanical Systems*, vol. 14, no. 6, pp. 1298-1310, 2005.
- [59] M. A. Hopcroft, W. D. Nix and T. W. Kenny, "What is the Young's Modulus of Silicon?," *Journal of microelectromechanical systems*, vol. 19, no. 2, pp. 229-238, 2010.
- [60] Y. Jimbo and K. Itao, "Energy loss of a cantilever vibrator," *J. Horolog. Inst*, vol. 47, pp. 1-15, 1968.
- [61] J. A. Judge, D. M. Photiadis, J. F. Vignola, B. H. Houston and J. Jarzynski, "Attachment loss of micromechanical and nanomechanical resonators in the limits of thick and thin support structures," *Journal of Applied Physics*, vol. 101, no. 1, 2007.
- [62] H. Zhili, A. Erbil and F. Ayazi, "An analytical model for support loss in micromachined beam resonators with in-plane flexural vibrations," *Sensors and Actuators A: Physical*, vol. 109, no. 1, pp. 156-164, 2003.
- [63] D. Rabinovich, D. Givoli and E. Becache, "Comparison of high-order absorbing boundary conditions and perfectly matched layers in the frequency domain,"

International Journal for Numerical Methods in Biomedical Engineering, vol. 26, no. 10, pp. 1351-1369, 2010.

- [64] J. P. Berenger, "A perfectly matched layer for the absorption of electromagnetic waves," *Journal of computational physics*, vol. 114, no. 2, pp. 185-200, 1994.
- [65] U. Basu and A. K. Chopra, "Perfectly matched layers for time-harmonic elastodynamics of unbounded domains: theory and finite-element implementation," *Computer methods in applied mechanics and engineering*, vol. 192, no. 11, pp. 1337-1375, 2003.
- [66] W. C. Chew, J. M. Jin and E. Michielssen, "Complex coordinate system as a generalized absorbing boundary condition," in *IEEE Antennas and Propagation Society International Symposium*, Montreal, Quebec, Canada, 1997.
- [67] A. Frangi, A. Bugada, M. Martello and P. T. Savadkoohi, "Validation of PML-based models for the evaluation of anchor dissipation in MEMS resonators," *European Journal of Mechanics-A/Solids*, vol. 37, pp. 256-265, 2013.
- [68] D. D. Gerrard, J. N. Eldwin, H. A. Chae, A. H. Vu, Y. Yushi and T. W. Kenny, "Modeling the effect of anchor geometry on the quality factor of bulk mode resonators," in *Solid-State Sensors, Actuators and Microsystems (TRANSDUCERS)*, 2015.

- [69] V. Thakar and M. Rais-Zadeh, "Optimization of tether geometry to achieve low anchor loss in Lamé-mode resonators," in *European Frequency and Time Forum & International Frequency Control Symposium (EFTF/IFC)*, 2013.
- [70] P. G. Steeneken, J. J. Ruigrok, S. Kang, J. T. M. Van Beek, J. Bontemps and J. J. koning, "Parameter extraction and support-loss in MEMS resonators," *arXiv*, 2013.
- [71] R. Abdolvand, J. Gonzales and G. Ho, "Finite element modeling of resonators," in *Resonant MEM*, Wiley-VCH, 2015.
- [72] H. Zhua and Y. Leea, "Design of phononic crystal tethers for frequency-selective quality factor enhancement in AlN piezoelectric-on-silicon resonators," *science direct*, vol. 120, pp. 516-519, 2015.
- [73] A. Albarbar, A. Badri, K. Sinha and A. Starr, Performance evaluation of MEMS accelerometers, Elsevier, 2009.
- [74] S. Gong and G. Piazza, "Monolithic Multi-Frequency Wideband RF Filters Using Two-Port Laterally Vibrating Lithium Niobate MEMS Resonators," *Microelectromechanical Systems*, vol. 23, no. 5, pp. 1188-1197, 2014.
- [75] R. T. Smith and F. S. Welsh, "Temperature Dependence of the Elastic, Piezoelectric, and Dielectric Constant of Lithium Tantalate and Lithium Niobate," *Applied Physics*, vol. 42, pp. 2219-2230, 1971.

- [76] R. Tabrizian, G. Casinovi and F. Ayazi, "Temperature-Stable Silicon Oxide (SiO₂) Micromechanical Resonators," *IEEE Transactions on Electron Devices*, vol. 60, no. 8, pp. 2656-2663, 2013.
- [77] W. Pan, P. Soussan, B. Nauwelaers and H. A. C. Tilmans, "Design and fabrication of a surface micromachined frequency tunable film bulk acoustic resonator with an extended electrostatic tuning range," in *IEEE international ultrasonics symposium (IUS)*, Rotterdam, 2005.
- [78] M. Shahmohammadi, D. Dikbas, B. P. Harrington and R. Abdolvand, "Passive tuning in lateral-mode thin-film piezoelectric oscillators," in *Joint Conference of the IEEE International Frequency Control and the European Frequency and Time Forum (FCS)*, San Francisco, CA, USA, 2011.
- [79] D. E. Serrano, R. Tabrizian and F. Ayazi, "Electrostatically tunable piezoelectric-on-silicon micromechanical resonator for real-time clock," *IEEE Transaction on Ultrasonic Ferroelectric and frequency control*, vol. 59, no. 3, pp. 358-365, 2012.
- [80] z. Wu, A. Peczalski and M. Rais-Zadeh, "Device-layer ovenization of fused silica micromechanical resonators for temperature-stable operation," in *Solid-state sensors, actuators, and microsystems workshop*, Hilton Head Island, 2014.

- [81] J. Lim, K. Choi, H. Kim, T. Jackson and D. Kenny, "Miniature Oven Controlled Crystal Oscillator (OCXO) on a CMOS Chip," in *IEEE International Frequency Control Symposium and Exposition*, Miami, FL, 2006.
- [82] S. A. Bhawe, D. Gao, R. Maboudian and R. T. Howe, "Fully-differential poly-SiC Lamé mode resonator and checkerboard filter," in *International Conference on Micro Electro Mechanical Systems*, Miami Beach, FL, 2005.
- [83] M. Ziaei-Moayyed, D. Elata, J. Hsieh, J. P. Chen, E. P. Quevy and R. T. Howe, "Fully Differential Internal Electrostatic Transduction of a Lamé-Mode Resonator," in *International Conference on Micro Electro Mechanical Systems*, 2009.
- [84] V. Thakar and M. Rais-Zadeh, "Temperature-compensated piezoelectrically actuated Lamé-mode resonators," in *International Conference on Micro Electro Mechanical Systems (MEMS)*, San Francisco, CA, 2014.
- [85] C. Cassella, Y. Hui, Z. Qian, G. Hummel and M. Rinaldi, "Aluminum Nitride Cross-Sectional Lamé Mode Resonators," *Microelectromechanical Systems*, vol. 25, no. 2, pp. 275-285, 2016.
- [86] M. A. Caro, S. Zhang, T. Riekkinen, M. Ylilammi, M. A. Moram, O. Lopez-Acevedo, J. Molarius and T. Laurila, "Piezoelectric coefficients and spontaneous polarization of ScAlN," *Journal of Physics: Condensed Matter*, vol. 27, no. 24, 2015.

- [87] H. Mansoorzare, S. Moradian, S. Shahraini, J. Gonzales and R. Abdolvand, "Achieving the Intrinsic Limit of Quality Factor in VHF Extensional-Mode Block Resonators," in *International Frequency Control Symposium (IFCS)*, 2018.
- [88] S. Shahraini, H. Fatemi and R. Abdolvand, "Cross-Sectional Quasi-Lame modes in Thin-Film Piezoelectric on Silicon Resonators," in *A Solid-State Sensors, Actuators and Microsystems Workshop*, Hilton Head Island, 2018.
- [89] S. Shahraini, H. Fatemi and R. Abdolvand, "Temperature Coefficient of Frequency in Silicon-Based Cross-Sectional Quasi Lame Mode Resonator," in *IEEE International Frequency Control Symposium (IFCS)*, Olympic Valley, CA, 2018.
- [90] C. M. Lin, T. T. Yen, V. V. Felmetger, M. A. Hopcroft, J. H. Kuypers and A. P. Pisano, "Thermally compensated aluminum nitride Lamb wave resonators for high temperature applications," *Applied Physics Letters*, 2010.
- [91] R. Farraro and R. B. Mclellan, "Temperature dependence of the Young's modulus and shear modulus of pure nickel, platinum, and molybdenum," *Metallurgical Transactions*, vol. 8, no. 10, pp. 1563-1565, 1977.
- [92] H. J. McSkimin, "Measurement of elastic constants at low temperatures by means of ultrasonic waves—data for silicon and germanium single crystals, and for fused silica," *Journal of Applied Physics*, vol. 24, no. 8, pp. 988-997, 1953.

- [93] R. Abdolvand, G. K. Ho, J. Butler and F. Ayazi, "ZnO-on nanocrystalline diamond lateral bulk acoustic resonators," in *In Micro Electro Mechanical Systems*.
- [94] S. Matsuda, M. Hara, M. Miura, T. Matsuda, M. Ueda, Y. Satoh and K. Y. Hashimoto, "Use of fluorine-doped silicon oxide for temperature compensation of radio frequency surface acoustic wave devices," *IEEE Transactions on Ultrasonics, Ferroelectrics, and Frequency Control*, vol. 59, no. 1, pp. 135-138, 2012.
- [95] M. Yoshimaru, S. Koizumi and K. Shimokawa, "Structure of fluorinedoped silicon oxide films deposited by plasma-enhanced chemical vapor," *Journal of Vacuum Science & Technology*, vol. 15, no. 6, pp. 2908-2914, 1997.
- [96] W. Pang, R. C. Ruby, R. Parker, P. W. Fisher, M. A. Unkrich and J. D. Larson, "A temperature-stable film bulk acoustic wave oscillator," *Electron Device Letters*, vol. 29, no. 4, pp. 315-318, 2008.
- [97] S. W. Lim, Y. Shimogaki, Y. Nakano, K. Tada and H. Komiyama, "Changes in Orientational Polarization and Structure of Silicon Dioxide Film by Fluorine Addition," *Journal of Electrochemical Society*, vol. 146, no. 11, pp. 4196-4202, 1999.
- [98] V. Pankov, C. Alonso and A. Ortiz, "Analysis of structural changes in plasma-deposited fluorinated silicon dioxide films caused by fluorine incorporation using

- ring-statistics based mechanism," *JOURNAL OF APPLIED PHYSICS*, vol. 86, no. 1, 1999.
- [99] H. Fatemi, H. Zeng, J. Carlisle and R. Abdolvand, "High-Frequency ThinFilm AlN-on-Diamond Lateral–Extensional Resonators," *Journal of Microelectromechanical Systems*, vol. 22, no. 3, pp. 678-686, 2013.
- [100] G. Chen, C. Cassella, Z. Qian, G. Hummel and M. Rinaldi, "Aluminum Nitride cross-sectional Lamé mode resonators with 260 MHz lithographic tuning capability and high $kt^2 > 4\%$," in *IEEE International Frequency Control Symposium (IFCS)*, New Orleans, LA, 2016.
- [101] G. K. Ho, R. Abdolvand, A. Sivapurapu, S. Humad and F. Ayazi, "Piezoelectric-on-Silicon Lateral Bulk Acoustic Wave Micromechanical Resonators," *Journal of Microelectromechanical Systems*, vol. 17, no. 2, pp. 512-520, 2008.
- [102] R. Melamud, S. A. Chandorkar, B. Kim, H. K. Lee, J. C. Salvia, M. A. Hopcroft and T. W. Kenny, "Temperature-insensitive composite micromechanical resonators," *Journal of Microelectromechanical systems*, vol. 18, no. 6, pp. 1409-1419, 2009.
- [103] D. Serrano, "Electrostatically tunable piezoelectric-on-silicon micromechanical resonator for real-time clock," *IEEE Transaction on Ultrasonic Ferroelectric and frequency control*, 2012.

